INTERNAL REPORT
HIP-2016-04

DEVELOPMENT OF QUALITY ASSURANCE METHODS FOR PARTICLE DETECTORS

ANELIYA KARADZHINOVA - FERRER

Division of Particle Physics and Astrophysics
Department of Physics
Faculty of Science
University of Helsinki
and
Helsinki Institute of Physics
P.O.Box 64, FI-00014, Helsinki, Finland

ACADEMIC DISSERTATION

To be presented for public criticism, with the permission of the Faculty of Science of the University of Helsinki, in the auditorium CK112 of the Exactum building, A. I. Virtasen aukio 1, on 21.10.2016, at 12:00 o'clock.

Helsinki 2016

ISBN 978-951-51-1267-5 (Paperback)
ISSN 1455-0563
Helsinki University Print (Unigrafia Oy)

ISBN 978-951-51-1268-2 (PDF)
http://ethesis.helsinki.fi
Electronic Publications at the University of Helsinki

Helsinki 2016

Custos:

Prof. Paula Eerola
Director, Helsinki Institute of Physics, Finland

Supervisors:

Doc. Eija Tuominen
Doc. Ivan Kassamakov
Dr. Jaakko Härkönen
Dr. Panja Luukka

Department of Physics, University of Helsinki
and Helsinki Institute of Physics, Finland

Reviewers:

Prof. Jan Rak

Department of Physics
University of Jyväskylä
Finland

Dr. Archana Sharma

Physics Department
CERN
Switzerland

Opponent:

Prof. Anders Oskarsson

Department of Physics
Lund University
Sweden

ABSTRACT

The purpose of this thesis is to develop, establish and apply novel quality assurance (QA) methods for nuclear and high-energy physics particle detectors. The detectors should be maintenance-free since devices can only be replaced during long technical shut-downs. Furthermore, the detector modules must endure handling during installation and withstand heat generation and cooling during operations. Longevity in a severe radiation environment must also be assured. Visual inspection and electrical characterisation of particle detectors are presented in this work.

The detector studies included in this thesis, while based on different technologies, were united by the demand for reliable and enduring particle detectors. Four major achievements were accomplished during the the Gas Electron Multiplier (GEM) foil studies: a software analysis capable of precise foil inspection was developed, a rigorous calibration procedure for the Optical Scanning System was established, a detailed 3D GEM foil hole geometry study was performed for the first time and an impact of the hole geometry on the detector gain was confirmed. Promising results were also achieved during the solid-state detectors studies. A new technique for assuring the height uniformity of the chip interconnections in the pixel detector modules was proposed and implemented. Two semiconductor detectors (Si and GaAs) were designed, microfabricated and tested. The consistency of the QA results demonstrated the detectors' reliability and preparedness to serve the needs of future particle and nuclear physics experiments.

During the performed studies, strict calibration techniques and measurement uncertainties were applied to guarantee the trustworthy accuracy of the used measurement tools. Thus, all quality assurance techniques presented in this thesis were held in clean conditions at monitored temperature and humidity.

The combined results of this thesis demonstrate the importance of adequate quality assurance for guaranteed accurate data collection and long operating life of the detector.

ACKNOWLEDGMENTS

I wish to thank the heads of the Helsinki Institute of Physics (HIP), the Department of Physics at the University of Helsinki and the Detector Laboratory for providing the facilities and equipment for the research presented in this thesis. The doctoral studies and conference travels were funded by scholarship from the Doctoral program of Particle Physics and Universe Sciences (PAPU) and the HIP CMS Upgrade Project.

I am indebted to two incredible ladies, Prof. Paula Eerola and Doc. Eija Tuominen, for giving me the opportunity to be part of the PhD program of HIP. My deep gratitudes go also to Doc. Ivan Kassamakov, Dr. Jaakko Härkönen and Dr. Panja Luukka for their support, guidance and confidence in me during my studies.

I would like to express my gratitude to the pre-examiners Prof. Jan Rak and Dr. Archana Sharma for their accurate and sensible comments, which greatly improved the quality of my thesis. I am grateful to Prof. Anders Oscarsson for having accepted to be my opponent. I would like to thank Doc. Eija Tuominen, Dr. Camille Bélanger-Champagne and Dr. Panja Luukka for proofreading my thesis and providing important comments and suggestions that improved the manuscript.

I had the opportunity to start my particle physics adventure during some of the most exciting and inspiring times in this field: performing the successful first run of the LHC, proving the existence of the Higgs boson and completing the Standard Model, detecting gravitational waves and many others that lit my path.

I had the privilege to work in a group with extensive experience with the construction, testing and installation of various particle detectors, housed by the biggest experiments in contemporary high-energy physics. I am grateful for the help of all my colleagues in the Detector Laboratory, especially Rauno Lauhakangas, a great physicist, lecturer and detector builder.

Several researchers have made possible the existence of this doctoral thesis, their names are acknowledged in the papers that are part of this thesis. I wish to express my gratitude to all of them. Especially, I would like to thank Dr. Matti Kalliokoski and Dr. Timo Hildén for their invaluable help in the beginning of my PhD research.

I am grateful for the incredible support from my family and friends. I would like to thank Tiina Naaranoja for her assistance, thoughtful discussions and countless coffee breaks. Most importantly, I would like to thank my wonderful husband Alejandro for his love and patient encouragement throughout this journey.

Aneliya Karadhzinova - Ferrer, HIP, 2016

"The only instrument we are using in high-energy physics is a ruler."

Rauno Lauhakangas
Electrical engineer, HIP

CONTENTS

ABSTRACT v

ACKNOWLEDGMENTS vii

PURPOSE AND STRUCTURE OF THIS THESIS 1

1 INTRODUCTION 5
- 1.1 Basic understanding of matter . . . 5
- 1.2 Physics experiments relevant for this thesis . . . 6
  - 1.2.1 CERN . . . 6
  - 1.2.2 FAIR . . . 9

2 DETECTION OF RADIATION IN PARTICLE PHYSICS 13
- 2.1 Radiation interaction . . . 13
  - 2.1.1 The Bethe-Bloch formula . . . 13
  - 2.1.2 Primary and secondary ionization . . . 15
- 2.2 Detectors of ionizing radiation . . . 15
  - 2.2.1 Gas electron multiplier detectors . . . 16
  - 2.2.2 Solid-state detectors . . . 23
    - 2.2.2.1 Silicon detectors . . . 25
    - 2.2.2.2 Flip-chip interconnections . . . 27

3 QUALITY ASSURANCE OF PARTICLE DETECTORS 29
- 3.1 Motivation for QA . . . 29
- 3.2 Approach towards trustworthy QA . . . 31
- 3.3 GEM foil detectors . . . 31
  - 3.3.1 Software analysis for GEM foil inspection . . . 33
  - 3.3.2 SEM traceable calibration of the Optical Scanning System . . . 34
  - 3.3.3 SWLI traceable calibration of the OSS . . . 38
  - 3.3.4 GEM foil hole geometry . . . 40
  - 3.3.5 Detector gain simulation based on hole geometry . . . 44
- 3.4 Solid-state detectors . . . 48
  - 3.4.1 Visual inspection of flip-chip interconnections . . . 49
  - 3.4.2 Electrical characterisation of solid-state detectors . . . 51

4 Discussion and Research Conclusion **55**

A Traceability and Calibration Procedures for QA Instruments **59**
A.1 SEM calibration 59
A.2 SWLI calibration 61
A.3 Probe-station calibration 64

B Measurement Uncertainties **65**

Bibliography **71**

ABBREVIATIONS

ALICE	A Large Ion Collider Experiment
ANSYS	Engineering analysis software
APPA	Atomic, Plasma Physics and Applications experiment
ATLAS	A Toroidal LHC AparatuS
CBM	Compressed Baryonic Matter experiment
CERN	European Organization for Nuclear Research
CMS	Compact Muon Solenoid experiment
CV	Capacitance-Voltage (measurement)
DLTS	Deep Level Transient Spectroscopy
FAIR	Facility for Antiproton and Ion Research
FCB	Flip-Chip Bonding
Garfield ++	Simulation software for gaseous tracking detectors
GEM	Gas Electron Multiplier
HIP	Helsinki Institute of Physics
ISO	International Organization for Standardization
IV	Current-Voltage (measurement)
LHC	Large Hadron Collider
LHCb	Large Hadron Collider beauty experiment
LS1 and LS2	Long Shut-down 1 and 2 at LHC
NIST	National Institute of Standards and Technology
NUSTAR	NUclear STructure, Astrophysics and Reactions experiment
OSS	Optical Scanning System
PANDA	PANDA experiment
ROC	Read-Out Chamber/Chip
SEM	Scanning Electron Microscope/Microscopy

SM	Standard Model
Super-FRS	Super FRagment Separator project at FAIR
SWLI	Scanning White Light Interferometer/Interferometry
TOTEM	Total Cross Section, Elastic Scattering and Diffraction Dissociation Measurement at the LHC
TCT	Transient Current Technique
TPC	Time Projection Chamber
TS	Transfer Standard
UBM	Under Bump Metallization
UKAS	United Kingdom Accreditation Service
QA	Quality Assurance

LIST OF SYMBOLS

d	Inner diameter of the GEM foil hole
D	Outer diameter of the GEM foil hole
I_{leak}	Leakage current of the solid-state detector
H	Maximum height of the soldering bumps
P	Pitch between the centres of the GEM foil holes
S	Shift between the centres of the two diameters of the GEM foil hole
T	Total thickness of the GEM foil
T_m	Metal thickness of the GEM foil
T_p	Polyimide thickness of the GEM foil
V_{fd}	Depletion voltage of the solid-state detector

PURPOSE AND STRUCTURE OF THIS THESIS

The purpose of this thesis is to improve, develop, establish and apply novel quality assurance (QA) methods for the detectors in the international nuclear and high-energy physics communities. Several steps were taken before achieving these goals: ensuring the calibration of the instruments used for visual inspection of Gas Electron Multiplier (GEM) foils and flip-chip interconnections; fulfilling the requirements of the ISO/IEC 17025, UKAS M3003 and GUM JCGM 100:2008 standards for calculating measurement uncertainty; and studying the impact of GEM hole geometry on the GEM detector gain by using simulation software. Similar calibration checks were performed on the set-up used for the electrical characterisation of the solid-state particle detectors.

The structure of the thesis is as follows: in the current chapter, the summary of the original publications and the author's contributions are presented. Chapter 1 introduces the Standard Model as the framework for our understanding of matter and presents the most relevant experiments for this thesis that study matter and its interactions. In Chapter 2, an introduction to the radiation detection in particle physics is given, followed by a description of the two main particle detector types in the modern physics experiments that are relevant to this work. The motivation and approach for QA of particle detectors, as well as the applied inspection techniques and the obtained results are presented in Chapter 3. In Chapter 4, the discussion and research conclusions are presented.

List of original publications

This thesis is based on the following publications:

Publication I: Optical quality assurance of GEM foils, T. Hildén, E. Brücken, J. Heino, M. Kalliokoski, A. Karadzhinova, R. Lauhakangas, E. Tuominen and R. Turpeinen, *Nuclear Instruments and Methods in Physics Research A* **770**, 113-120 (2015).

Publication II: Calibrating an optical scanner for quality assurance of large area radiation detectors, A. Karadzhinova, T. Hildén, M. Berdova, R. Lauhakangas, J. Heino, E. Tuominen, S. Franssila, E. Hæggström, and I. Kassamakov, *Measurement Science and Technology* **25**, 115403 (2014).

Publication III: Scanning White Light Interferometry for Optical Scanner Calibration using GEM-foil based Traceable Standard, A. Karadzhinova, A. Nolvi, T. Hildén, R. Lauhakangas, E. Hæggström, E. Tuominen and I. Kassamakov, *Frontiers in Optics 2014, OSA Technical Digest (online)* **FW5A.2** (2014).

Publication IV: Impact of GEM foil hole geometry on GEM detector gain, A. Karadzhinova, A. Nolvi, R. Veenhof, E. Tuominen, E. Hæggström and I. Kassamakov, *Journal of Instrumentation* **10** (2015).

Publication V: Characterization of Ni/SnPb-TiW/Pt Flip Chip Interconnections in Silicon Pixel Detector Modules, A. Karadzhinova, A. Nolvi, J. Härkönen, P. Luukka, T. Mäenpää, E. Tuominen, E. Hæggström, J. Kalliopuska, S. Vähänen and I. Kassamakov, *Proceedings of Science, TIPP2014* **092** (2014).

Publication VI: Strip Detectors Processed on High-Resistivity 6-inch Diameter Magnetic Czochralski Silicon (MCz-Si) Substrates, X. Wu, J. Harkonen, J. Kalliopuska, E. Tuominen, T. Mäenpää, P. Luukka, E. Tuovinen, A. Karadzhinova, L. Spiegel, S. Eranen, A. Oja, and A. Haapalinna, *IEEE Transactions on Nuclear Science* **61**, 611-618 (2014).

Publication VII: Processing and characterization of epitaxial GaAs radiation detectors, X. Wu, T. Peltola, T. Arsenovich, A. Gädda, J. Härkönen, A. Junkes, A. Karadzhinova, P. Kostamo, H. Lipsanen, P. Luukka, M. Mattila, S. Nenonen, T. Riekkinen, E. Tuominen, and A. Winkler, *Nuclear Instruments and Methods in Physics Research A* **796**, 51-55 (2015).

The publications are referred to in the text by their Roman numerals.

Author's contribution

The research has been carried out at Helsinki Institute of Physics during the years 2013 - 2016. The author is the main writer of Publications II, III, IV and V and has also contributed to the writing of Publication I. The author participated actively in the GEM foil scanning and tuning the software analysis developed in Publication I. The experimental work, simulations and data analysis in Publications II, III, IV and V were carried out by the author. The author was also responsible for the electrical characterisation (CV and IV measurements) of the solid-state detectors processed for Publications VI and VII.

Summaries of the original publications

Publication I: Optical quality assurance of GEM foils

An Optical Scanning System (OSS), constructed at Helsinki Institute of Physics (HIP), was employed for visual quality assurance of GEM foils. A software application was developed to analyse the images taken by the system to determine the GEM foil quality and reliability. The relationship between the GEM hole size and foil performance, as well as the software capability, were discussed.

Publication II: Calibrating an optical scanner for quality assurance of large area radiation detectors

A rigorous calibration procedure was developed for the OSS. The calibrated high-aspect ratio system ensures the quality of large area GEM foils. The performed calibration fulfilled the requirements of the ISO/IEC 17025 and UKAS M3003 standards for calculating measurement uncertainty with 95 % confidence level. The proposed large-scale scanning technique can potentially be applied to other optical instruments that work in the micro scale.

Publication III: Scanning White Light Interferometry for Optical Scanner Calibration using GEM-foil based Traceable Standard

Based on previous experience, a new approach for OSS calibration was performed, GEM foils were specifically prepared to serve as transfer links between the OSS and a Scanning White Light Interferometry (SWLI) device. In this manner, traceability of the OSS calibration via the SWLI was established (calibrated dynamically and statically at the Finnish Centre for Metrology and Accreditation (MIKES)). This methodology complies with the ISO/IEC 17025, UKAS M3003 and and GUM JCGM 100:2008 standards. Relying on this technique and using more suitable TS, smaller uncertainty in the OSS was achieved.

Publication VI: Impact of GEM foil hole geometry on GEM detector gain

Real GEM foil hole geometry was examined in detail for the first time. Four new GEM hole geometry parameters were defined using high-resolution SWLI. To study the effect of hole geometry on detector gain, the ANSYS and Garfield ++ software tools were employed to simulate GEM detector gain based on collected data for the GEM foil hole geometry. In addition, 70 different shape variations of the GEM foil hole ge-

ometry were created to study the effective gain as a function of hole parameters in a GEM foil with uniformly shaped holes. Later they were compared to a foil carrying holes with the originally designed shape.

Publication V: Characterization of Ni/SnPb-TiW/Pt Flip Chip Interconnections in Silicon Pixel Detector Modules

Silicon pixel detectors are typically connected to readout chips by flip-chip bonding using solder bumps. High-quality electro-mechanical flip-chip interconnects minimize the number of dead read-out channels in the detector system. The uniformity of the solder bumps was studied using SWLI. This technique proposes a way to decrease the number of dead channels of the silicon pixel detector modules by precisely measuring the soldered bump height to ensure that they fulfil the required specifications.

Publication VI: Strip Detectors Processed on High-Resistivity 6-inch Diameter Magnetic Czochralski Silicon (MCz-Si) Substrates

The tracking detectors for future high-luminosity particle physics experiments have to be simultaneously radiation hard and cost efficient. Silicon strip detectors made of high resistivity Magnetic Czochralski silicon (MCz-Si) substrates were successfully processed and characterised. Thorough electrical characterisation of the MCz-Si detectors was performed and the obtained results demonstrate that these detectors can be manufactured by an industrial scale semiconductor process.

Publication VII: Processing and characterization of epitaxial GaAs radiation detectors

Radiation detectors made on epitaxial GaAs substrates are a promising alternative to the silicon devices used for spectroscopy and radiography applications. It was proven that such a device with thickness of $100\,\mu\mathrm{m}$ has 60 % better absorption efficiency compared to a $300\,\mu\mathrm{m}$ thick silicon device. The X-ray detector was successfully manufactured and its reliability was confirmed by electrical characterisation measurements of Capacitance-Voltage (CV), Current-Voltage (IV). Transient Current Technique (TCT) and Deep Level Transient Spectroscopy (DLTS) were also used during the detector inspection.

CHAPTER 1

INTRODUCTION

1.1 Basic understanding of matter

The Standard Model (SM) [1], shown in Figure 1.1, is a quantum field theory that describes all the basic constituents of matter and their interactions via fundamental forces.

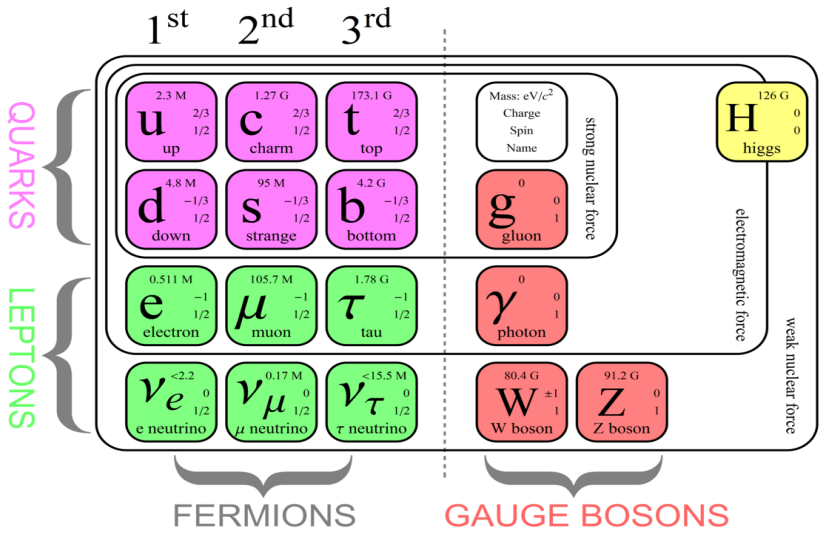

Figure 1.1: The elementary particles and the gauge bosons of the Standard Model quantum field theory [2].

For decades various experiments around the world have been built to test and confirm its predictions. In 2012 the Standard Model was finally completed with the discovery of the last predicted fundamental particle - the Higgs boson [3, 4]. Its detection answered some questions but also led to many new ones. Particle physics does not only study the SM but also spreads beyond its postulates. Many theories beyond the SM are waiting for an experimental evidence of their existence. Therefore, a demand for new, more sensitive and powerful high-energy and nuclear physics experiments is rising. Two of these experiments are presented in the sections below.

The goals of the high-energy and nuclear physics experiments are to study:

- Particle collisions for possible manifestations of physics beyond the Standard Model such as dark matter candidates and existence of extra dimensions, in ad-

dition to increasing the understanding of strong interactions.

- Particle properties including particle mass m, charge q, spin s, mean life τ.
- Global event characteristics for example multiplicity, mean transverse momentum and missing energy.

1.2 Physics experiments relevant for this thesis

1.2.1 CERN

The European Organization for Nuclear Research (CERN) [5] is the largest laboratory with the most powerful accelerator at this moment (2016). It houses the biggest high-energy physics experiments. Since September 2008, the physics program of this facility has been performed at the Large Hadron Collider (LHC) [6] that accelerates two proton beams up to 7 TeV per beam, which are collided at four main collision points, see Figure 1.2. Each point is surrounded by a large detector to record the elementary particles induced by the collision. The four main experiments at the LHC are:

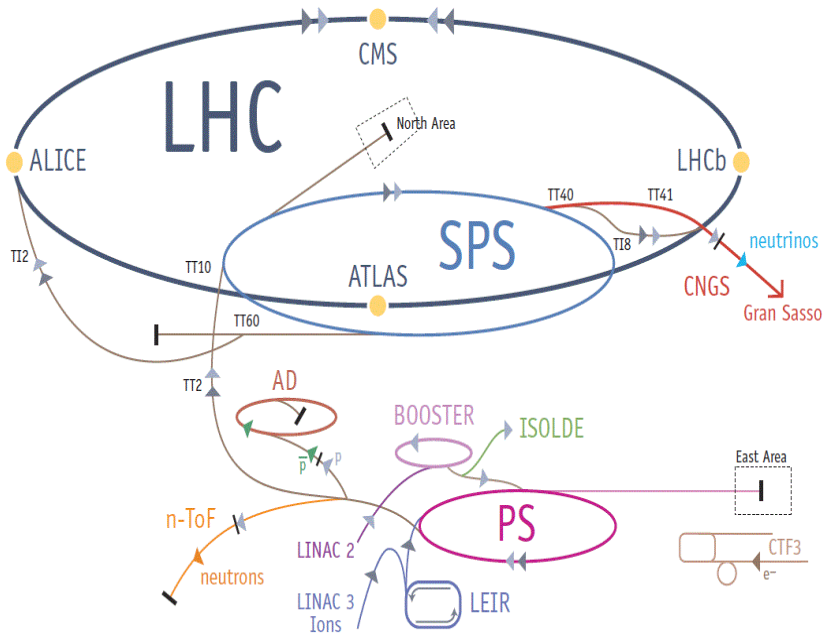

Figure 1.2: A schematic view of the CERN accelerator complex [5].

- A Large Ion Collider Experiment (ALICE) [7] designed to study heavy ion collisions studies.
- A Toroidal LHC AparatuS (ATLAS) [8] and the Compact Muon Solenoid (CMS) [9] are general purpose experiments, their main focus is pursuing a broad physics programme with general purpose detector design.

- The Large Hadron Collider beauty (LHCb) [10] experiment devoted to b quark physics.

Complementary to the CMS detector there is a smaller experiment, the Total Cross Section, Elastic Scattering and Diffraction Dissociation at the LHC (TOTEM) [11]. The physics program of TOTEM is focused on the measurement of the total proton-proton cross section, elastic scattering and soft diffractive processes that occur during the beam collision inside the CMS detector.

Each of these experiments consists of several sub-detectors in concentric layers around the interaction region. They allow the identification of the individual particles, their energy and momentum. An example of such a detector structure is shown in Figure 1.3. In general, the particle detectors can be divided into three groups according to the identification technique they use:

- Particle interaction with the detector material - a particle that passes through matter deposits a part (or all) of its energy within the detector by radiation of electromagnetic waves (including light) or ionization. The energy released in the detector depends on the energy and momentum of the particle that has entered, as well as the properties of the particle.
- With magnetic field - the momentum of a charged particle can be studied by measuring the curvature of its trajectory.
- Time of flight - measures the time that it takes for a particle to enter and leave the detector.

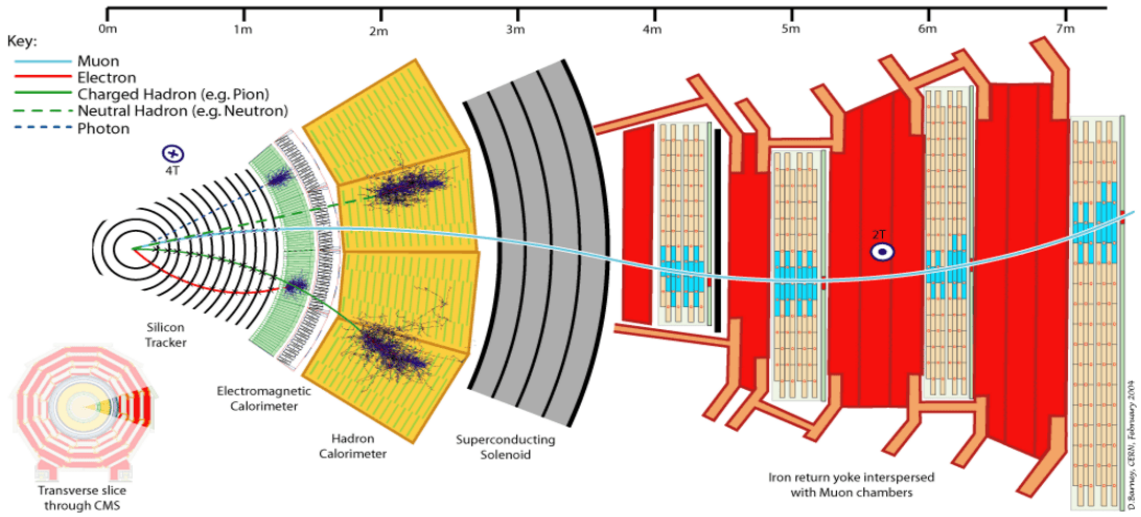

Figure 1.3: Cross-section of the CMS experiment, showing particles passing through its various parts [12].

The LHC experiments are made up of about 150 million sensing elements in total and they are able to operate at the LHC collision rate of up to 40 MHz. After filtering, about 100 collisions of interest are recorded per second for analysis. To extend its

discovery potential, the LHC will undergo a major upgrade to increase its luminosity (rate of collisions) by a factor of 10 beyond the original design value (from 300 to 3000 fb^{-1}) [13]. Thus, upgrades of the detectors will also be required due to the radiation dose increase in the detector material during collision and the higher amount of data that will be collected.

The Helsinki Institute of Physics became a CERN member in 1991. Since then the Detector Laboratory took an essential role in the TOTEM T2 Telescope constructions, quality assurance and installation of the GEM detectors. The CMS Tracker Outer Barrel rods, which provide support for the silicon strip detectors, readout electronics and all the necessary cables, were also constructed in Finland. The Detector laboratory had a large contribution to the ALICE strip detectors. Figure 1.4 gives an overview of the HIP contribution to the CERN experiments. The current responsibilities of the Helsinki Institute of Physics and the Detector Laboratory for CERN are related with the upgrade phases of ALICE and CMS (described below) and the construction of new detector in TOTEM [14].

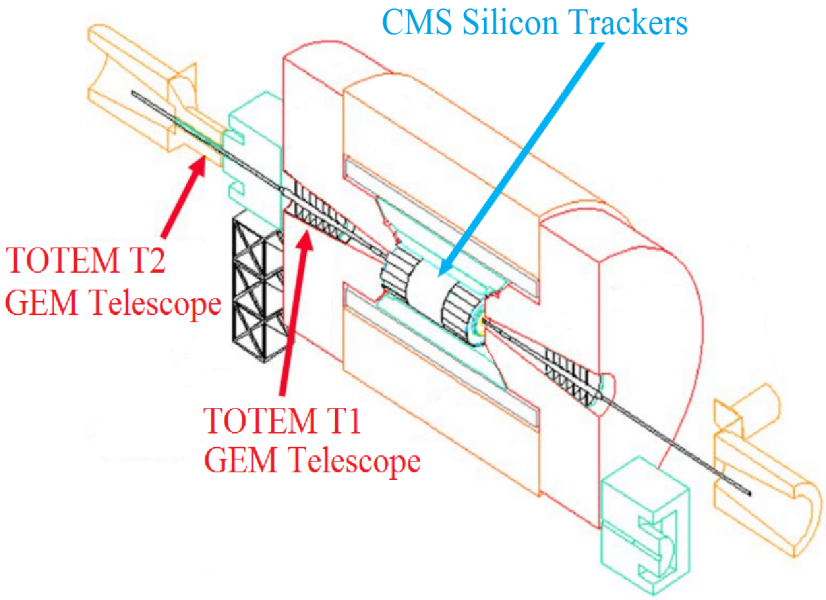

Figure 1.4: The contributions of the Helsinki Institute of Physics to the CERNs experiments. Side view of the inner most detector of CMS, the Silicon Tracker and of the two TOTEM GEM Telescopes [15].

HIP contribution to the ALICE upgrade

One of the ALICE Tracking Detector systems consist of Time Projection Chambers (TPC) [16]. A major upgrade of the TPC readout chambers (ROC) is planned after the second long LHC maintenance break (LS2) [17]. The current system is based on

Multi-Wire Proportional Chambers [18] and will be replaced by Gas Electron Multiplier detectors [19], see Figure 1.5.

Strict design criteria for the new ROCs should be applied to guarantee accurate data collection and long operating life of the detector. Thus, thorough quality assurance of the detectors must be employed to fulfil this goal (see Section 3.3).

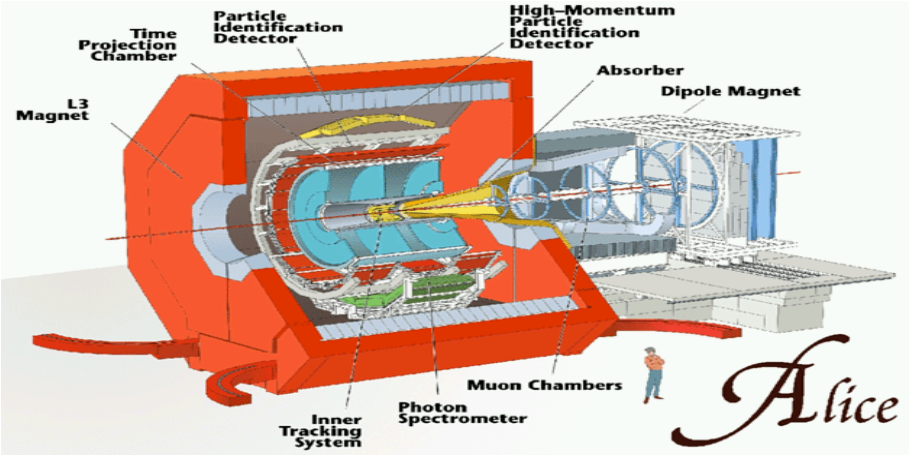

Figure 1.5: Cross-section of the ALICE experiment, showing the Time Projection Chambers in the centre of the detector [20].

HIP contribution to the CMS upgrade

The innermost detector of CMS consists of silicon pixel detector modules, see Figure 1.4. During its upgrade, it will be completely rebuilt and accompanied by new readout electronics capable of handling the higher amount of data expected after the first LHC maintenance break (LS1) [21]. The number of channels, i.e pixels and related interconnections, will simultaneously be increased from the current 64 million up to 125 million channels allowing significantly better tracking performance. Successful, reliable, timely, and economical manufacturing of these modules, to be installed during the end of 2016, requires reliable and accessible quality assurance methods (see Section 3.4).

The HIP contribution to the CMS upgrades also includes a long-term research program focused on the development of radiation-hard silicon pixel and strip particle detectors described in Publication VI, for the phase II upgrade of the CMS and other experiments requiring extreme radiation hardness and tracking granularity.

1.2.2 FAIR

The Facility for Antiproton and Ion Research (FAIR), will house experiments in various fields of physics [22]. The research program of the international accelerator facility will

be based on antiproton and ion studies that have not been possible to perform earlier and in other facilities.

Similarly to CERN, FAIR will host several physics programs in parallel. The four main experiments at the FAIR, illustrated in Figure 1.6, are:

- The Atomic, Plasma Physics and Applications (APPA) program [23], formed by five different sub-collaboration experiments devoted to studies of material science, biology, atomic physics and their applications.
- The Compressed Baryonic Matter experiment (CBM) [24] designed to study highly compressed nuclear matter.
- The PANDA experiment [25] devoted to study the strong interaction physics by proton–antiproton annihilation.
- The Nuclear Structure, Astrophysics and Reactions (NUSTAR) [26] is another group of sub-collaboration experiments studying the structure and dynamics of unstable nuclei.

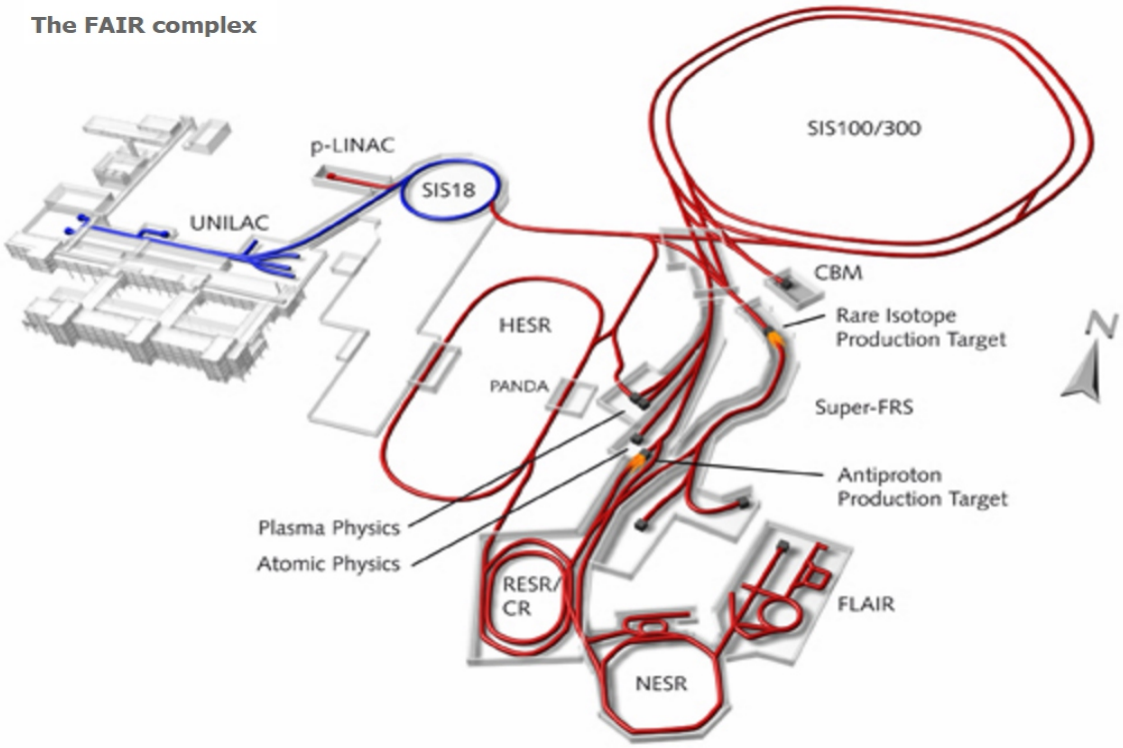

Figure 1.6: A schematic view of the future FAIR facility [27].

HIP contribution at FAIR

Production of dense monoisotopic nuclear beams is required for the purposes of the FAIR physics program. To achieve such beams, a beam monitoring detector system, shown in Figure 1.7, is needed during operation [28]. This detector should be able to

measure and track beams of different particle energies and densities with high resolution. The detectors should be able to sustain a severe radiation environment since these devices can only be replaced during long technical shut-downs. The high intensity of the beams (approximately 10^6 particles per second) also requires that the detector is able to operate with only a short time window to clean the drift volume from the collected charge. Such a speed cannot be achieved with the basic TPC technology, thus a detector with complementary particle amplification with GEM was proposed. In 2011, the first GEM-TPC prototype detector was successfully built and tested for tracking and particle identification [29]. To ensure the design performance is achieved, rigorous quality assurance of the GEM foils will be performed (see Section 3.3).

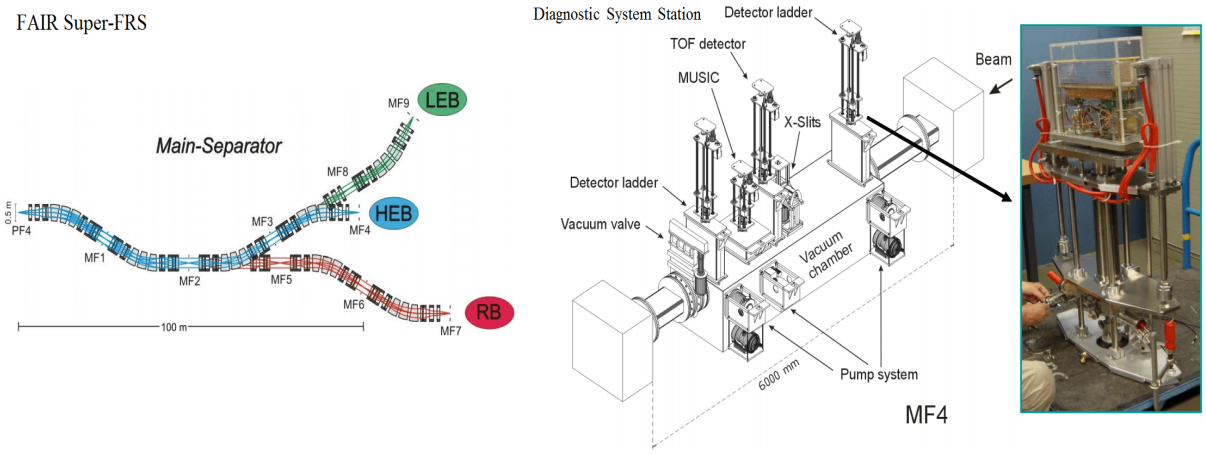

Figure 1.7: The beam monitoring system at FAIR (left) and the GEM-TPC prototype detector (right) [30, 31].

CHAPTER 2

DETECTION OF RADIATION IN PARTICLE PHYSICS

2.1 Radiation interaction

The accurate measurement of particle trajectories is one of the most important tasks for any particle physics experiment. Trajectories provide important information about the event interaction point, the decay path, and the charge and momentum, when a magnetic field can be applied. The principle of particle detection rests mainly on the deposition of energy into the active medium of the detector.

The well-established theory presented in this section is based on [32, 33].

2.1.1 The Bethe-Bloch formula

While moving across matter, particles undergo elastic and inelastic collisions with the electrons and nuclei of atoms, and thereby lose energy. The main process responsible for energy losses is due to Coulomb interaction (elastic or not) of the incident particles with the orbital electrons of the atoms. This energy loss induces some ionization (primary). The rate of energy loss is subject to fluctuations, but it is possible to estimate its average by unit of travelled distance in a material by using the Bethe-Bloch formula:

$$-\frac{dE}{dx} = k\rho\frac{Zz^2}{A\beta^2}\left(\ln\left[\frac{2m_e c^2\beta^2\gamma^2 E_M}{I^2}\right] - 2\beta^2 - \delta - \frac{2C_e}{Z}\right). \tag{2.1}$$

In this expression:

- $k = 2\pi m_e c^2 r_e^2 N_A \approx 0.154\ \mathrm{MeVcm^2/g}$;
- $m_e c^2 \approx 0.51\ \mathrm{MeV}$ is the electron rest energy (electron mass);
- $c \approx 3$ x $10^8\ \mathrm{m/s}$ is the speed of light in a vacuum;
- $r_e = e^2/4\pi\epsilon_0 m_e c^2 \approx 2.82$ x $10^{13}\ \mathrm{cm}$ is the classical electron radius;
- $e \approx 1.602$ x $10^{-19}\ \mathrm{C}$ is the electric charge;
- $\epsilon_0 = 8.8542$ x $10^{-12}\ \mathrm{F/m}$ is the vacuum permittivity;
- $N_A \approx 6.02$ x $10^{23}\ \mathrm{mol^{-1}}$ is the Avogadro number;
- ρ is the density of the absorbing medium in $\mathrm{g.cm^{-3}}$;
- z is the charge of the incident particles in units of the electron charge;

- Z and A are, respectively, the atomic number and the mass number of the material through which the particle travels;
- $\beta = v/c$ is the velocity of the incident particle and γ is the Lorentz's factor ($\gamma = \beta / \sqrt{1-\beta^2}$);
- E_M is the maximal energy transferred in a single collision to a free electron by a particle of mass M and velocity v;
- I is the ionization energy averaged over all electrons;
- δ and C_e/Z are corrections terms. The δ is the density effect of the polarization of the medium by the particle that crosses it. The C_e/Z is the shell correction that is needed due to the absence of contribution to the ionization processes of the deep shells (K, L, etc.) of the atom of the medium;

In summary, energy loss depends essentially on the velocity of the particle (β), its charge (z) and the nature of the medium (Z and A), and on the probability of interaction that increases with the density (ρ). The energy loss $\frac{dE}{dx}$ has a global minimum for particles with $3.0 < \beta\gamma < 3.5$. Particles with an energy loss close to this minimum are called minimum-ionizing particles (MIPs).

Figure 2.1 illustrates the calculated energy loss for protons in liquid, gaseous and solids over a wide momentum range. The qualitative behaviour difference at high energies between a gas (*He* in the figure) and the other materials shown in the figure is due to the density-effect correction, $\delta(\beta\gamma)$ [34]. Table 2.1 shows the properties of materials commonly used in particle detectors compared to *Al* and *Fe* (see Figure 2.1).

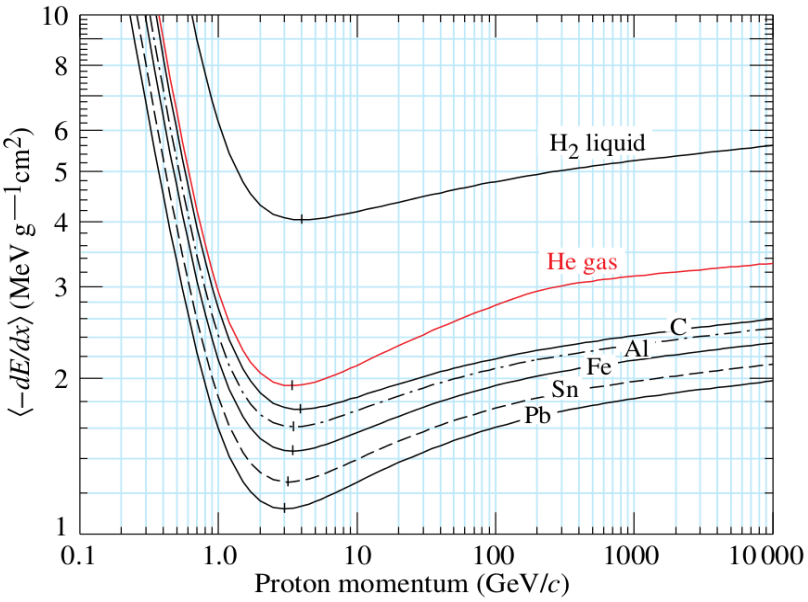

Figure 2.1: Mean energy loss rate according to the Betche-Bloch equation for protons in liquid, gases and solids. The lines for *Si* (Z = 14) and *Ar* (Z = 18) fall between the lines for *Al* (Z = 13) and *Fe* (Z = 26) [34].

2.1.2 Primary and secondary ionization

Electron-ion pairs are form, when a charged particle passes through matter and loses its energy through a discrete number of primary ionizing collisions. The ejected electrons can have enough energy to ionize other atoms in the material and produce secondary electron-ion pairs. The sum of the primary and secondary ionization is the total ionization and its value is proportional to the energy lost by the incident particle in the detector:

$$n_T = \frac{\Delta E}{W_i}, \tag{2.2}$$

where ΔE is the total energy given by the incident particle to the medium and W_i is the average minimal energy needed to create an ion-electron pair. The number of primary pairs n_p is dependent on Z of the detector medium.

Table 2.1: Properties of materials commonly used in particle detectors for comparison with *Al* and *Fe* (see Figure 2.1) [34].

Material	Z	A	$\langle Z/A \rangle$	I (eV)	dE/dx ($\mathrm{MeVcm^2/g}$)	ρ ($\mathrm{g.cm^{-3}}$)
Al	13	26.9815	0.48181	166.0	1.615	2.699
Si	14	28.0855	0.49848	173.0	1.664	2.329
Ar	18	39.9480	0.45059	188.0	1.519	1.662
Fe	26	55.8450	0.46557	286.0	1.451	7.874
$Polyimide film$			0.51264	79.60	1.820	1.420
CO_2			0.48889	85.00	1.819	1.842

2.2 Detectors of ionizing radiation

The detectors of ionizing radiation are the main tools in experimental particle and nuclear physics. The purpose of the detector is to register not only the presence of radiation, but also to give information about the energy of the particles, their trajectory, momentum and charge. The deposited radiation energy inside the working volume of the detector is converted into a human readable signal such as an electrical impulse, a light pulse, a photographic image or even a sound.

Charged particles transmit their energy to the medium through ionization, leading to excitation and ionization of atoms. In contrast, neutral radiation undergoes some typical interactions before these newly charged particles excite and ionize the material.

Particle and nuclear physics experiments primarily use detectors with electrical (analogue) signal with modern electronics that digitize the signal and transmit it to computers, making the data processing stage much easier.

The ionizing radiation detectors are characterised by the following properties [35]:

- Sensitivity - the minimum energy that must be deposited in the detector so as to produce a signal;
- Energy resolution - the ionization per unit length, or in the case of large enough detector, the proportionality of the signal to the initial energy of the particle.
- Time resolution - the time lag and time jitter from the arrival of the particle until the appearance of the signal, and the duration of the output pulse;
- Efficiency - the fraction of the particle flux incident on the detector that is detected;

This thesis focuses on the quality assurance of the two particle detector types used in the leading physics experiments: gaseous and solid-state (silicon) detectors. They are both ionization chamber detectors working with similar operation principles, described in detail in the following sections. However, due to the nature of their sensing characteristics they are also very different in many aspects.

2.2.1 Gas electron multiplier detectors

The invention of the Multi-Wire Proportional Chamber (MWPC) by Charpak in 1968 [18] radically changed the particle detector field. With its good position accuracy and rate capability, and the possibility to electronically record signals generated by the passage of the particle in the detection medium, the MWPC became the "ancestor" of many other modern gaseous particle detectors, such as Drift and Time Projection Chambers. Furthermore, their use has extended into several fields, such as astroparticle and medical physics.

A significant improvement was made in 1996 when Fabio Sauli introduced the Gas Electron Multiplier (GEM) [19]. Today, these gas detectors are used for position detection of ionizing radiation such as charged particles, photons, X-rays [36] and neutrons at CERN, FAIR and the Joint European Torus (JET) project [37].

Unlike other gaseous detectors, the multiplication and the signal induction regions in GEM detectors are physically distinct, resulting in greater freedom in the readout geometry. Moreover, the possibility to divide the multiplication in multiple steps allows a drastic reduction in the problem of discharge and detector ageing processes [38].

The foil manufacturing

A GEM detector features a densely pierced 50 ± 1 µm thick polyimide foil, coated with a 5 ± 1 µm thin copper/chromium layer on both sides, see Figure 2.2. The holes in the GEM foil have an inner diameter of 50 ± 5 µm, an outer diameter of 70 ± 5 µm and pitch of 140 µm [19].

The samples, used in this study, were a CERN standard 10 x 10 cm^2 double mask

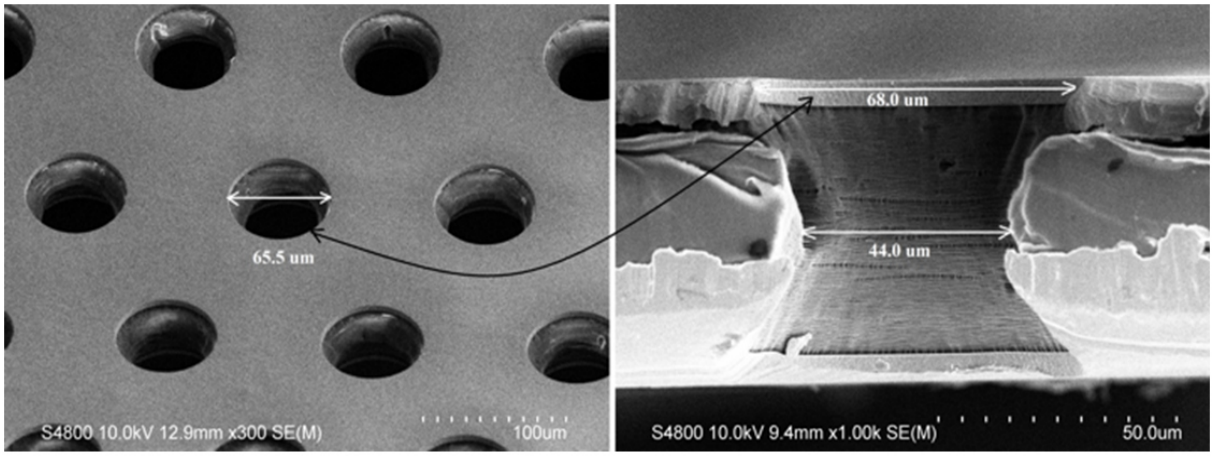

Figure 2.2: SEM image of a GEM foil - top view (left) and cross-section (right).

GEM foils [39]. They were manufactured at the CERN workshop by photolitographic technology, illustrated on Figure 2.3, that was developed by R. de Oliveira and his colleagues [40]. Conventional lithography is used to imprint the standard hexagonal pattern of the holes on both sides of the pre-manufactured sandwich (Cu/Cr-polyimide-Cr/Cu) structure (also known as double mask GEM foil). The hourglass-shape hole is then developed in the middle part of the sandwich by using the remaining metal as a mask for the polyimide etch. Since the last step is applied simultaneously on both sides of the foil, the developed holes have a bi-conical shape.

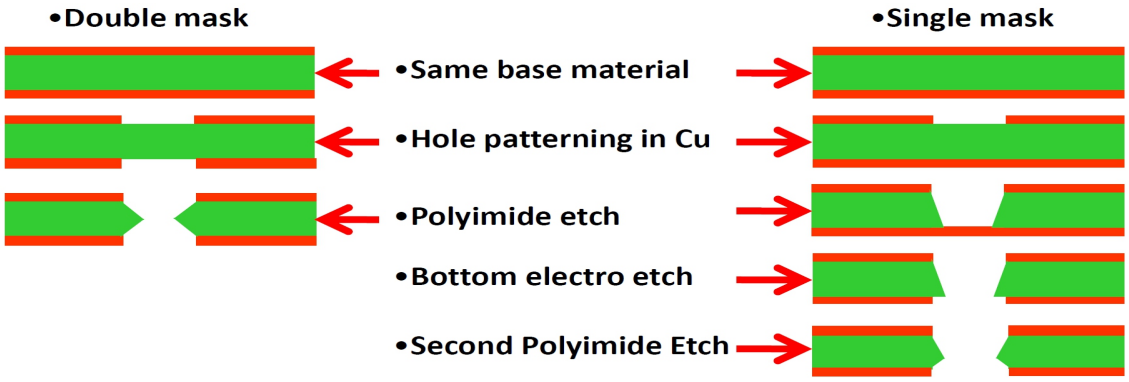

Figure 2.3: Double (left) and single (right) mask GEM foil manufacturing techniques [40].

Detector operation

One of the main processes that occur in the GEM detectors is an electron avalanche. It takes place, when free electrons exhibit acceleration by an applied electric field and thereafter collide with other atoms of the surrounding medium, thereby ionizing them.

This releases additional electrons which accelerate and collide with further atoms, releasing more electrons. For the case of GEM foil, see Figure 2.4, most electrons drifting towards the multiplier will be captured by the field, created inside the hole, undergo avalanche multiplication and exit on the other side.

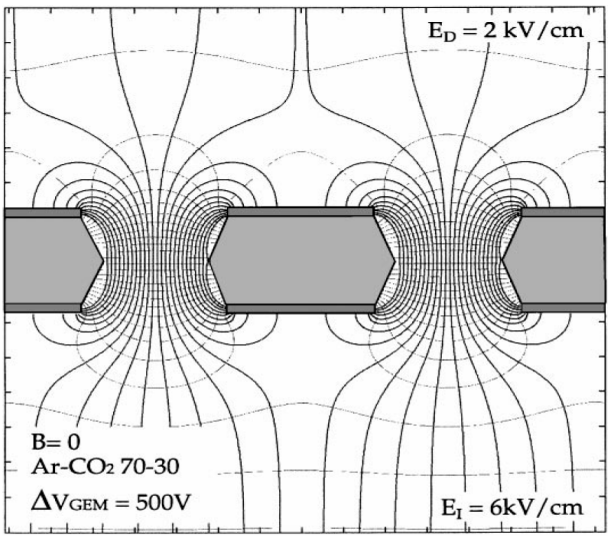

Figure 2.4: Electric field map in typical operational conditions in GEM holes [41].

For the detector to be operational a potential difference needs to be applied between the two metallized electrodes of the foil, thereby a high electric field is generated inside the holes. Drift and induction fields of 2 and 6 kV/cm, respectively, can be reached using a potential difference of $\Delta\ V_{GEM}$ = 500 V. This potential difference is enough for an avalanche multiplication to occur if electrons drift into the hole region [41]. The electric field shape inside the detector makes each hole act as an electron multiplier [19]. As shown in Figure 2.4, most of the field lines from the region above the multiplier enter the holes and exit on the lower side. A multiplication factor of 10^3 can be reached by a single GEM foil.

Some field lines enter the polyimide which becomes polarized in the field because it is a dielectric. This leads to the deposition of electrons on the polyimide surface in the region of the hole where the diameter is the smallest. This additional charge causes an increased field in the centre of the hole and thus an increase in the gain. Due to this phenomenon called charging up, the gain of the GEM increases by 30 % when irradiated. However, the charging up is a fast process (on the order of seconds, depending on the radiation intensity), while the discharging is very slow (on the order of hours) and an equilibrium is quickly reached.

The GEMs have high rate capability, restricted by the slow space charge built up in the multiplication region of the detector. A time period, known as a dead time, is needed to restore the electric field for creation of new avalanches. The rate capability

value has been theoretically calculated taking into account the operational parameters of the detector ($500\ \mathrm{MHz/cm^2}$). However the detector becomes completely inefficient at very high values. A rate of $10\ \mathrm{MHz/cm^2}$ has been experimentally obtained, showing detection stability with high rate capability [42].

This charge amplification technique permits detecting the presence and position of the charged particles, photons, X-rays, and neutrons. An absolute change of $1\ \mu\mathrm{m}$ in the hole diameter alters the amplification by a few % [41]. Hence, a critical phase of the GEM foil production is the mask alignment on both metal sides of the foil. The size and shape of the holes influence the gas multiplication factor [41]. For this reason, a single mask technology is used in the production of large area GEM foils. The studies presented in Publication I (also see Section 3.3.1) and Publication IV (also see Section 3.3.5) show that any misalignment in the two masks significantly affects the GEM foil performance.

Detector gas

Avalanche multiplication, in theory, can occur in any gas or gas mixture. However, to achieve low operating voltage, high stability, and high gain, the gas mixture should be carefully chosen.

In addition to the desired ionization, excited atoms are produced in the primary avalanche process inside the gas volume. The excited noble gas atoms can only return to their ground state through the emission of a photon. The minimum energy of this photon is 11.6 eV for argon, which is well above the ionizing potential of the copper electrodes in the detector, and therefore can release secondary electrons that cause new avalanches. The creation of these secondary avalanches can lead to a permanent discharge.

A gas mixture containing polyatomic molecules and argon is used to avoid the secondary avalanches. The nature of the polyatomic molecules allows them to absorb the de-excitation photons. The energy is subsequently dissipated by collisions or by dissociation of the molecule. Such gases are called quenchers and make up the smaller part of a detector gas mixture.

GEM detector construction

Since GEM is a charge amplification device, it is used as a preamplifier before the detector readout. It is possible to use one GEM as preamplifier for another GEM foil. The possibility to cascade several GEM stages to reach high gains is exploited in multiple-GEM foil detectors and allows the construction of GEM-based detectors capable of efficient detection of MIPs. They consist of three individual parts: the drift region, the multiplier layers, and the readout plane. Figure 2.5 provides a schematic view of a

single and a double GEM detector.

An ionizing particle traversing the detector produces charge along its entire trajectory through the gas volume. However, only the charge produced in the gap between the drift foil and the first multiplier stage contributes significantly to the signal, since for all other primary charges at least one amplification step is missing.

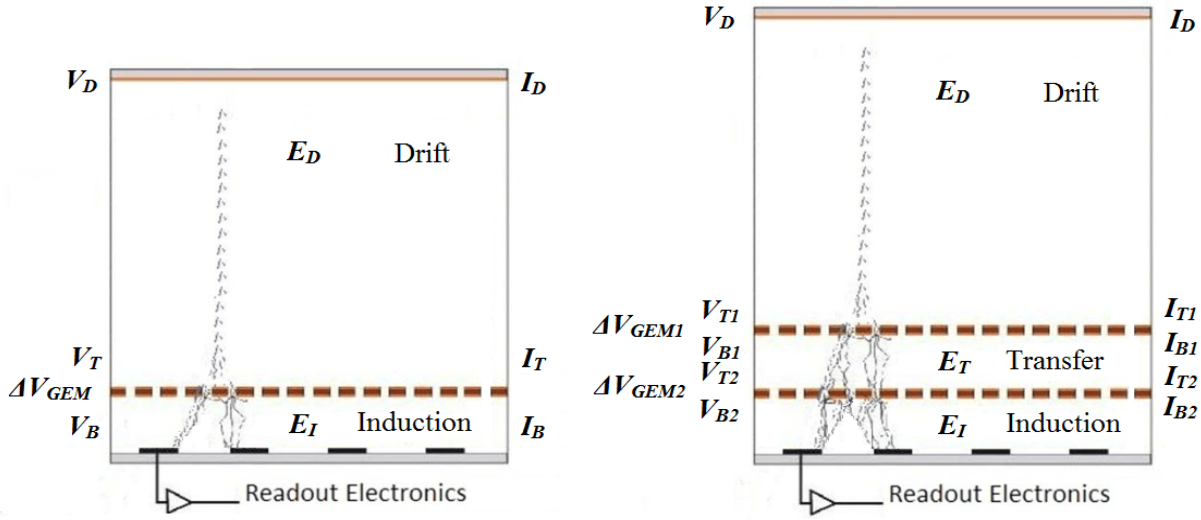

Figure 2.5: Schematic view of a single (left) and a double (right) GEM detector. The readout plane is shaded in grey [43].

Due to the drift field E_D, the electrons that are produced in the drift gap move towards the topmost multiplier. They undergo avalanche multiplication in the strong electric field caused by the voltage difference ΔV_{GEM1} between the two sides of the foil. In the case of a double-GEM detector, the larger electron cloud drifts in the transfer field E_T towards the second GEM, where the multiplication process is repeated. After the GEM foil(s) the electron cloud is ejected into the induction gap and drifts towards the readout plane under the influence of the induction field E_I. Here the charge is collected and read out with electronics. The separation of the readout circuit from the amplification region is one of the greatest advantages of pure GEM detectors. This limits the risk of damaging the fragile readout strips or the front-end electronics in the case of discharges. Triple-GEM detector configurations are also commonly used nowadays.

Diffusion, drift and gas multiplication

Diffusion and drift influence the behaviour of the cloud of charge carriers in the detector volume outside the amplification region.

In the absence of an electric field, charged particles assume the average thermal energy distribution of the gas via multiple collisions. The diffusion in the gas is char-

acterised by the diffusion coefficient D. The standard deviation of the distribution of charge originating from a localized charge at $t = 0$ after a time t is given by

$$\sigma_x = \sqrt{2Dt}, \tag{2.3}$$

with the diffusion coefficient D depending on the mass of the charged particle. For free electrons, the diffusion coefficient is much higher than for ions. The diffusion coefficient for electrons in *Ar* is in the order of 200 - 300 cm^2/s, much higher than the value for electrons in *Si*: 36 cm^2/s.

The application of a uniform electric field across the detector volume causes a movement of the charge carriers along the field direction (positive particles move in the direction of the field, negative particles in the opposite direction). This behaviour is called drift. The drift velocity depends on the strength of the electric field and on the mean free path of the charge carriers in the material.

In the plane perpendicular to the electric field, the diffusion behaviour is unchanged from the field-free case, but in the direction of the electric field, the diffusion coefficient changes, depending on the magnitude of the field.

The process of ionization by electron collisions is the basis for the avalanche multiplication. Upon application of a suitable difference of potential between electrodes, an electric field in the GEM hole develops. Electrons released by ionization in the upper gas volume, drift into the holes, avalanche in the high field region and leave towards the electrode [19]. Since the total charge n_T generated by the passage of a MIP is much too small to be detected by readout electronics, this charge has to be amplified before it can be read out.

While electrons drift in moderate electric fields, they receive enough energy between two collisions to participate in inelastic processes, namely excitation and ionization. If the energy of an electron exceeds the first ionization potential of the gas (15.7 eV for *Ar*), the result of a collision can be an ion pair, leaving the incident electron free to continue in the electric field.

The number of electron-ion pairs produced per unit length of drift by one primary electron is called the first Townsend coefficient, $\alpha = 1/\lambda$. It is the inverse of the mean free path for electrons. For small α the coefficient increases linearly with the energy of the electrons.

Inelastic processes are the basis of avalanche multiplication, as can be seen from the increase of the number of electrons after a path dx, i.e., $dn = n\alpha\, dx$. By integration, the total number of electrons n and the gain G after a distance x are:

$$n = n_0 e^{\alpha x} \quad \text{and} \quad G = \frac{n}{n_0} = e^{\alpha x}. \tag{2.4}$$

Signal formation

Typically, the signal from the detector is completely induced by the electron motion in the induction gap of the detecting device [38].

Current I_k induced on the electrode *k*, due to a moving charge *q* and velocity υ_d, can be calculated using Ramo's theorem [44]:

$$I_k = -\frac{q\overrightarrow{\upsilon_d}(x) \times \overrightarrow{F_k}(x)}{V_k} \tag{2.5}$$

where $\overrightarrow{F_k}(x)$ is the electric field created by raising the electrode *k* to the potential V_k [38].

As such, if V_k = 1 V and all the other pads are connected to ground, Ramo's theorem becomes:

$$I_k = -q\overrightarrow{\upsilon}(x) \times \overrightarrow{F_k^w}(x) \tag{2.6}$$

where $\overrightarrow{F_k^w}(x)$ is called the weighting field. The overall electric field in the detector, $\overrightarrow{F_k}(x)$ and the weighting field, $\overrightarrow{F_k^w}(x)$, are distinctly different (for any configuration with more than two electrodes). The electric field determines the charge trajectory and velocity, whereas the weighting field characterises how charge motion couples to a specific electrode depending only on the geometry of the detector [38].

It is expected that each propagating electron induces a rectangular pulse in the nearest readout pad with a width dependent on the time spent by the electron to cross the induction gap:

$$i = -\frac{q}{t} = -\frac{q\overrightarrow{\upsilon_d}}{x} \tag{2.7}$$

where *x* is the thickness of the of the induction gap and υ_d is the electron velocity in that gap [38].

Discharges

A limiting factor in the operation of all micro-pattern gas detectors is the occurrence of discharges at high gain, especially under the influence of heavily ionizing particles [45]. The transition from normal avalanche to a streamer leading to a discharge occurs if the total charge in the avalanche exceeds a value between 10^7 and 10^8 electron-ion pairs (Raether limit), leading to an enhancement of the electric field in the region of the avalanche. This causes a fast growth of secondary avalanches, leading to a breakdown of the gas rigidity.

Studies of discharges in single and multiple GEM structures are reviewed in detail in [46]. For multiple-GEM detectors, the discharges take place in the last multiplication step, where the avalanche is the largest. Thus, the use of triple-GEM detectors

is advantageous to detect MIPs. Optimal performance for a triple-GEM detector has been reached by a $\sim$ 10 % increase of the voltage V_{GEM} across the topmost foil and a $\sim$ 10 % decrease of the voltage across the bottom GEM with respect to the middle [45].

The water content of the detector gas has a significant influence on the discharge probability. An increase in the water content from $\sim$ 60 ppm to $\sim$ 80 ppm leads to an increase of the discharge probability by one order of magnitude. It is therefore necessary to keep the water content in the detector as low as possible.

2.2.2 Solid-state detectors

Solid-state detectors, also called semiconductor detectors, can be regarded as a kind of ionization chambers in which there is a solid dielectric instead of a gas between the electrodes.

Similar to gaseous detectors, solid-state detectors have had a long development period starting in 1943 with P. J. von Heerden and his successful fabrication of radiation conductivity counters. His work gave rise to an entirely new class of radiation detectors [47]. The first monolithic pixel detectors appeared in 1961 [48], providing position information in addition to the energy deposition signal. The first strip sensor was developed in 1970 for nuclear physics and nuclear medicine. A silicon sensor was used for the first time in 1973 at CERN as a segmented target [49].

Detector operation

An electrical pulse is obtained when an ionized particle passes through and deposits energy into the detector volume. The magnitude of this pulse is proportional to the deposited energy. Solid-state detectors have high-energy resolution, which allows separation of the energy spectrum and identification of the particles with close energies. Such a resolution could be very difficult and sometimes even impossible to achieve with gaseous detectors. Therefore, solid-state tracking detectors are used for accurate particle trajectory characterisation.

These solid-state tracking detectors are able to show the paths of electrically charged particles through the traces left by the ionized substance, when used in multiple layers configuration. In a magnetic field, they can be used to measure the radius of curvature of the path of the particles, and hence their momentum. A high-resolution vertex tracking detector is an example of such a device, positioned close to the point of collision.

Nevertheless, the gaseous and solid-state detectors are both ionization chambers that operate under similar operation principles. However, they are also very different mainly because of the nature of the sensing characteristics they employ. For example,

the energy required for the creation of an electron-ion pair is 3 eV in a typical silicon detector, compared to 30 eV in a typical gaseous detector. Also the stopping power in the solid-state detector is approximately 10^3 times larger than in the gas-filled detector. The solid-state devices have very good energy resolution, due to the difference in the density of the detector medium [35]. The size of the sensing area also affects the resolution, therefore, the smaller active area of the solid-state detector gives better position resolution compared to the gaseous detector. The diffusion effect is smaller than in the gas detectors, resulting in achievable position resolution of less than $10\,\mu\mathrm{m}$.

However, gas-filled detectors have some advantages over solid-state detectors. Their internal amplification, for example, provides a stronger signal and reduces the need for an external pre-amplifier. The gas-filled detectors also do not need external cooling systems to reduce noise and are also lower maintenance with lower operating and manufacturing costs.

P-n junction and depletion region

When n- and p-type semiconducting regions are in contact, the charge carriers recombine in the junction region [50]. The recombined electron-hole pairs leave net charge behind, which leads to the formation of an electric field and electric potential $\varphi(x)$ over the junction. This will eventually get large enough to stop the charge carriers from drifting towards the junction. As a result, there is now a region around the junction that has no free charge carriers and is called the depletion region. When a external reverse bias potential V is connected, the depletion region grows. The contact potential V_C is usually so small compared to the applied reverse bias that it can be ignored. The width of the depletion region W on the junction depends on the applied reverse bias voltage V:

$$W \approx \left(\frac{2\epsilon V}{qN_D}\right)^{1/2}, \tag{2.8}$$

where N_D is the dopant concentration on the lightly doped side, ϵ is the dielectric constant of the semiconducting material and q unit electric charge. When the detector is fully depleted, i.e. the depletion region has reached the physical boundaries of the semiconducting material, the depletion region cannot grow any more and stays constant. The voltage for the full depletion is denoted with V_{fd}.

Capacitance

The depletion region of the junction effectively becomes a parallel plate capacitor. The capacitance is then determined by the geometry of the capacitor:

$$C = \frac{\epsilon A}{d}, \tag{2.9}$$

where A is the overlapping area of the conductive material on either side of the dielectric and d is the thickness of the dielectric layer.

The capacitance per unit area over the junction is:

$$C = \frac{\epsilon}{W} \approx \left(\frac{q\epsilon N_D}{2V}\right)^{1/2}, \tag{2.10}$$

where the dielectric constant $\epsilon = \epsilon_0\epsilon_r$, is the product of the vacuum and the relative dielectric constants. This equation holds until the full depletion is almost reached. When the full depletion voltage V_{fd} is applied, the whole bulk is depleted of the charge carriers and the depletion region has reached its limits. After this point, the capacitance remains constant.

Current

Ideally, the only current present in the detector would be caused by the incident radiation. In reality, there is some leakage current, which in silicon is mainly caused by thermal pair production in the depletion region:

$$I_{leak} \approx qGW = \frac{qn_iW}{\tau_g}^{1/2}, \tag{2.11}$$

where G is the generation rate of the charge carriers, W is the depletion width, n_i is the intrinsic charge carrier concentration and τ_g is the lifetime of the generated electron-hole pairs. The thermal leakage current saturates after the full depletion is reached.

When the reverse bias gets high enough, a sudden increase in the leakage current is observed. This phenomenon is called (avalanche) breakdown. When the primary electrons created by the charged particle acquire high enough kinetic energy, they begin to create new electron-hole pairs. The resulting chain reaction will manifest itself as a strong multiplication of charge carriers [51]. A high enough breakdown current may damage the detector permanently (see Section 3.4.2).

2.2.2.1 Silicon detectors

A reverse biased p-n junction diode is the most often used silicon detector structure. It could be segmented into an array of narrow strips or pixels to achieve position sensitivity. When a charged particle passes through the detector, results in incident radiation that leads electron-hole pairs creation, see Figure 2.6. The holes drift in the electric field towards the negatively biased p-strips (or in the case of p-type detector - positively biased n-strip), collected as an electric pulse. Since the holes drift to the strip closest to them, it is possible to distinguish where the particle has crossed the detector, i.e. spatial resolution is obtained.

A variety of techniques for connecting detectors and their electronics has been developed over the years. Strip detectors are read out with discrete or hybrid electronics, where each channel is connected to its own separate amplifier by wire bonding, as illustrated in Figure 2.7. The idea is that by dividing a large-area diode into a many narrow strips, that can be read out separately.

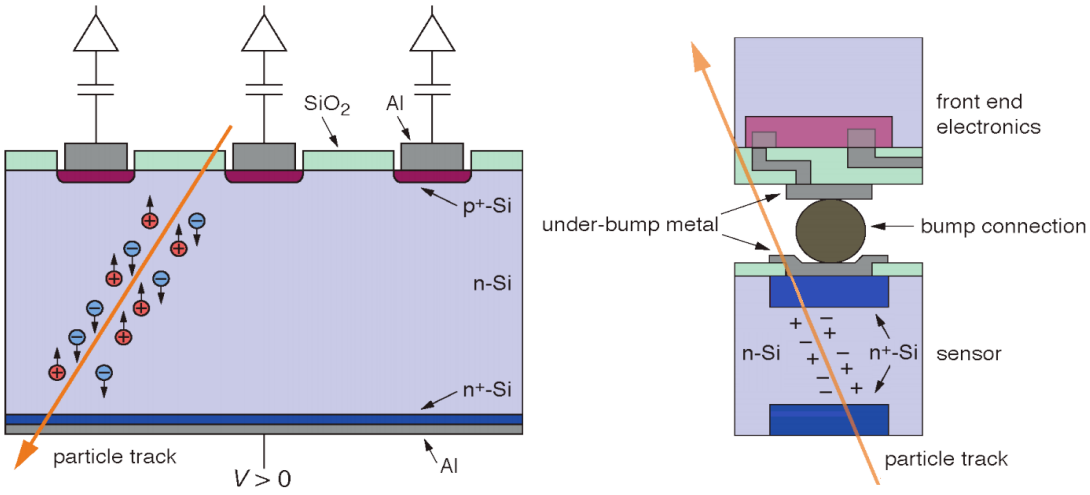

Figure 2.6: Operation principle of silicon strip and pixel detectors. Incident radiation (orange arrow) creates electron-hole pairs in strip (left) and pixel (right) detectors [52]. The currently used pixel detectors are n-on-n device.

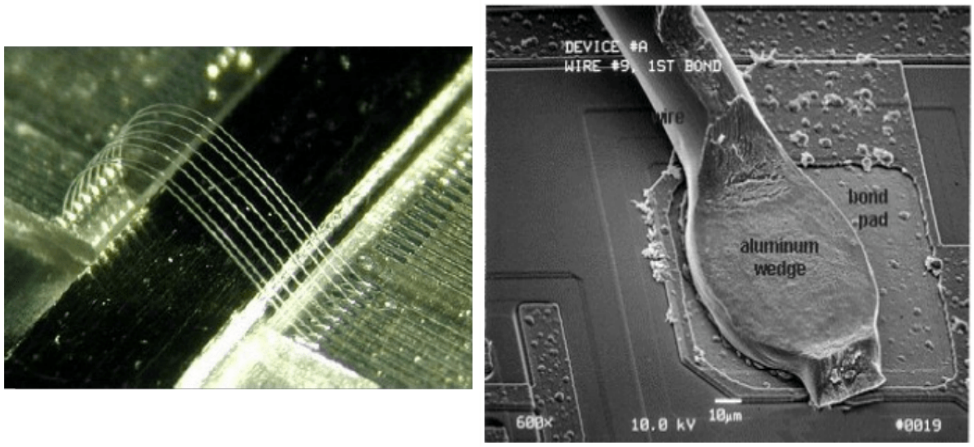

Figure 2.7: A typical wire bonding on a silicon strip module [53].

A standard pixel detector consist of two-dimensional diode arrays and electronics, which are usually built on separate substrates. For each pixel, an electronics channel provides amplification. The geometry of the electronics channel matches the diode pixel, shown in Figure 2.8, so that electronics and detector can be assembled face to face after having one of the devices "flipped" to the other surface. Thus, the technique where the electronics and sensors are connected in this fashion is called flip-chip bond-

ing (FCB). Each diode is connected to the electronic pad by a conductive "bump" [33]. The flip-chip technology is described below.

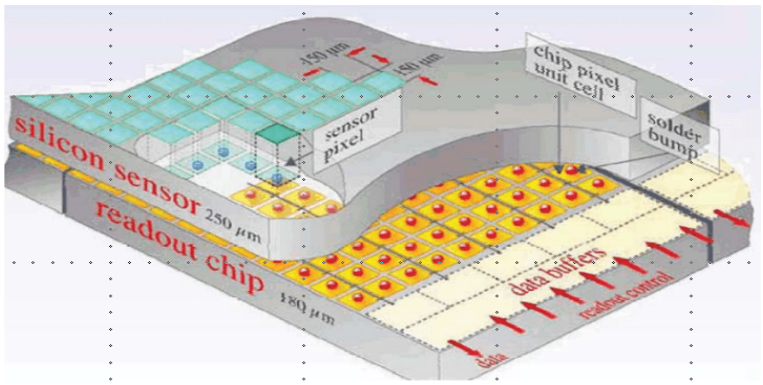

Figure 2.8: A typical outlook of a hybrid pixel module [12].

A detailed description of the silicon detector manufacturing technologies can be found in [54–56]. The specific manufacturing techniques used for the production of the solid-state detectors, both the magnetic Czochralski silicon strip detectors and the GaAs radiation detectors, are inspected in this thesis and are described in Publications Publications VI and VII, respectively.

2.2.2.2 Flip-chip interconnections

As mentioned above silicon pixel detectors are typically connected to the readout chips (ROCs) by flip-chip bonding using solder bumps. High-quality electro-mechanical flip-chip interconnectors minimize the number of dead read-out channels in the pixel detector system.

Flip-chip bonding technology, known since the 1960s, has advanced due to the commercial interest in high-density packaging, see Figure 2.9. This technology has demonstrated better electrical performance and reliability than conventional wire bonding [57]. The advanced fabrication technique of pixel systems allows a narrow pitch of ($55\,\mu\mathrm{m}$) between bumps. It is the preferred technique for hybridized radiation pixel detectors, where the radiation sensing structure and the readout chips are processed on different substrates.

To achieve reliable interconnection, Under Bump Metallization (UBM) is needed on both parts to be bonded. The solder is deposited only on the readout side; the corresponding pad on the sensor side is coated with a very thin layer of TiW/Pt (UBM).

For the research presented in Publication V and in Section 3.4.1, both the readout and sensor wafers were pre-processed. The particle detector elements were first cleaned to remove any particles that contaminated the wafers during handling, probing and transportation. Eutectic SnPb solder bumps were deposited on the readout

wafers and a thin film of TiW/Pt was deposited onto the sensor wafers as UBM, see Figure 2.10. Also the ROC wafers have UBM, not only the sensors (this is also visible on Figure 2.10).

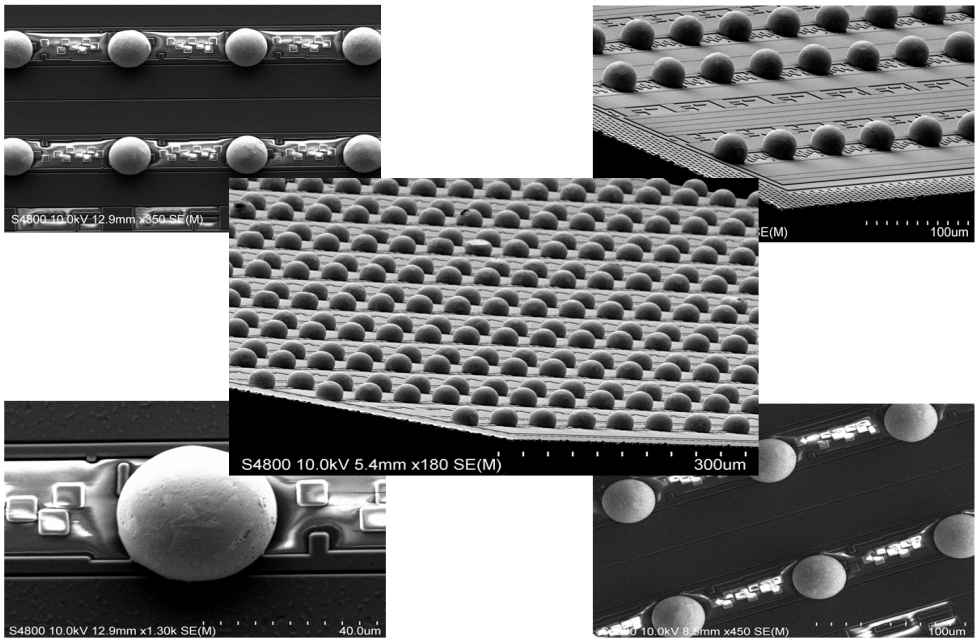

Figure 2.9: Solder bumps imaged with SEM.

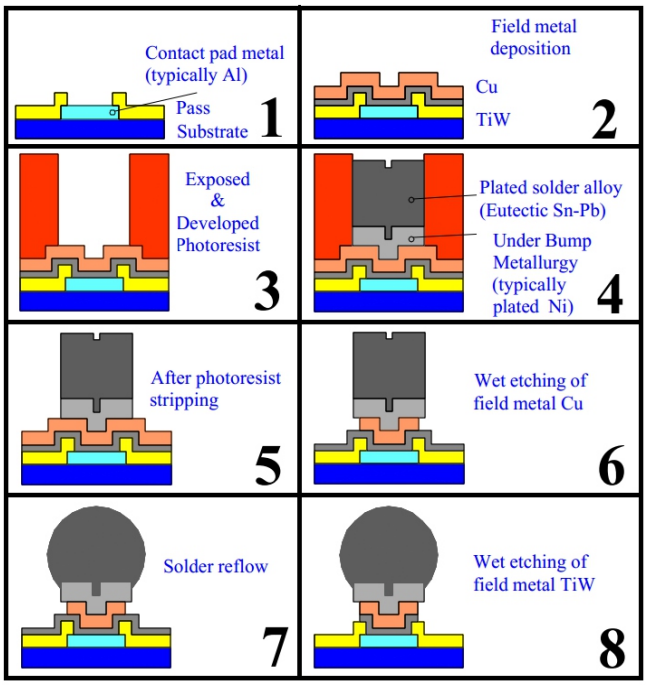

Figure 2.10: Bump manufacturing step-by-step process [58].

CHAPTER 3

QUALITY ASSURANCE OF PARTICLE DETECTORS

3.1 Motivation for QA

Particle detectors used in contemporary high-energy and nuclear physics experiments require precisely engineered structures. The detectors should be maintenance-free since devices can only be replaced during long technical shut-downs. Furthermore, the detector modules must endure handling during installation and withstand heat generation and cooling during operations. Longevity in a severe radiation environment should also be assured. Adequate quality assurance can guarantee a long operating life for detectors [59]. Two main inspection techniques are presented in this work: visual and electrical characterisations.

Visual inspection for defect is an important technique for verifying detector usability. For example, the electric field shape inside the GEM detectors makes each hole act as an electron multiplier through an avalanche process [19]. The area hole density is approximately 6400 holes per cm^2 and local variations in the size, shape [41], and rim roughness of the holes can alter the operational characteristics of the GEM foil. Consequently, these parameters should be uniform to achieve even performance across the active surface of the detector. Thus, the absence of defects is highly desired. Figure 3.1 illustrates defects observed on GEM foil surfaces such as missing holes, etching defects or dust.

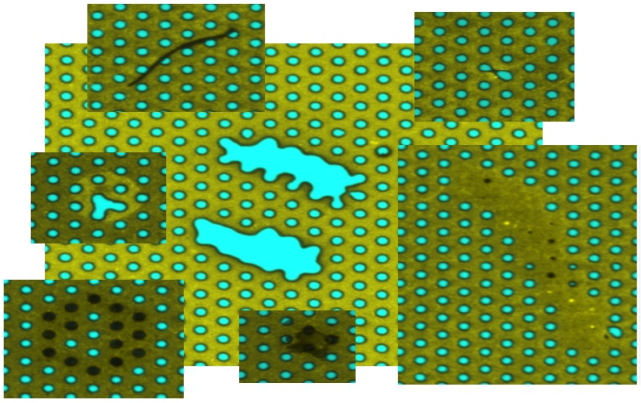

Figure 3.1: Examples of defects observed on GEM foil surfaces.

Another suitable candidate for visual inspection are the modern silicon pixel modules. They can feature up to 67 000 sensing elements which need to be individually connected to their read-out chains. The high quality of the soldered interconnections and their reliable connectivity is therefore key for the success of pixel detectors. The bumps have to be uniform in height to avoid open joints and solder bridges between adjacent pixels. Inhomogeneous bumps can cause significant stress on chips. An example of defective solder bumps is shown in Figure 3.2.

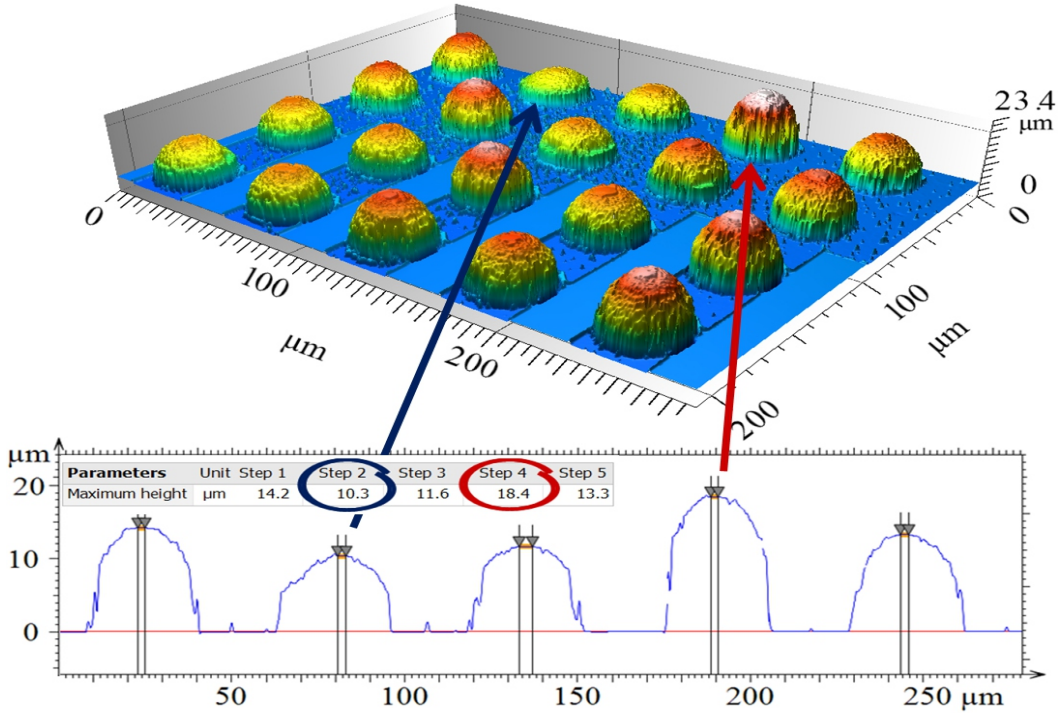

Figure 3.2: 3D reconstruction of defective solder bumps.

Electrical characterisation is another technique for QA of solid-state detectors. While rudimentary, this method provides a crucial evaluation of the basic parameters of a device and its behaviour. The total current through the detector is measured to obtain the leakage current of the detector during a current-voltage measurement. A capacitance-voltage measurement can also be used to determine the depletion voltage of the detector. Theoretically an optimal device should have low leakage current at high operational voltages. For example the 1 cm^2 silicon detector presented in this thesis had optimal operational depletion voltage of 150 V and leakage current of 55 nA.

The main focus of this work is on the development and assessment of improved and strict methods for quality assurance of particle detectors, which could guarantee not only the long operational life of the detectors but also accurate and precise radiation detection. These goals could be achieved by correctly calibrated and maintained instruments for the quality assurance.

3.2 Approach towards trustworthy QA

Several optical tools have been used for visual inspection in this thesis and Publications I-V: two high-resolution instruments (namely a Scanning Electron Microscope (SEM) and a Scanning White Light Interferometer (SWLI)) and an Optical Scanning System (OSS) with lower resolution. They were used individually or in comparison with each other, depending on the research purpose. In all cases, the calibration of each high-resolution instrument was checked according to the instrument specifications (see Appendices A1 and A2). Only after that check, the traceability between the individual instruments was established and calibration factors were determined, if necessary. Each calibration procedure followed the strict requirements for testing and calibration of vision systems, established by [60–63].

A semi-automated probe-station was used for the electrical characterisations of the studied solid-state detectors in Publications VI and VII. The system calibration was confirmed before each measurement session (see Appendix A3). All quality assurance techniques presented in this thesis were held in clean conditions at monitored temperature and humidity.

3.3 GEM foil detectors

Several techniques are used for GEM foil quality assurance. Most often, a high-voltage test is applied for a leakage current measurement of the GEM foil [64]. Visual inspection of GEM foils is less common. X-ray-based GEM foil inspection has also been proposed as a possible future inspection technique.

Visual QA is necessary not only to examine the size and the shape of the holes, but also to catch foil defects, residuals, and dust. Visual inspection is the only way to confirm the hole parameters. Slow speed is the main disadvantage of the visual QA compared to the HV QA. Visual inspection usually takes hours, while the HV test is completed in approximately 30 minutes. This drawback is especially important in the case of large-area GEM foil detectors, which are needed in many applications.

An Optical Scanning System for quality assurance of GEM foils was developed in the Laboratory for Nuclear Science at the Massachusetts Institute of Technology (U.S.A.) in 2006 [65, 66]. The University of Helsinki, together with the Helsinki Institute of Physics (Finland) [67] and Temple University (Philadelphia, U.S.A.) [68], developed their own systems on the basis of this first system (see Figure 3.3).

Helsinki Institute of Physics has several commitments with some of the largest particle physics experiments in Europe. According to the technical design review documents being prepared, upcoming FAIR and CERN experiments will require an estimated 340 m^2 of GEM foils. Since the area hole density is 6400 holes per cm^2, the

quality assurance must be able to process 22 billion holes in a limited time. This translates into a targeted inspection rate of approximately (5 - 10) x 10^6 holes per day with $5\,\mu\mathrm{m}$ imaging resolution.

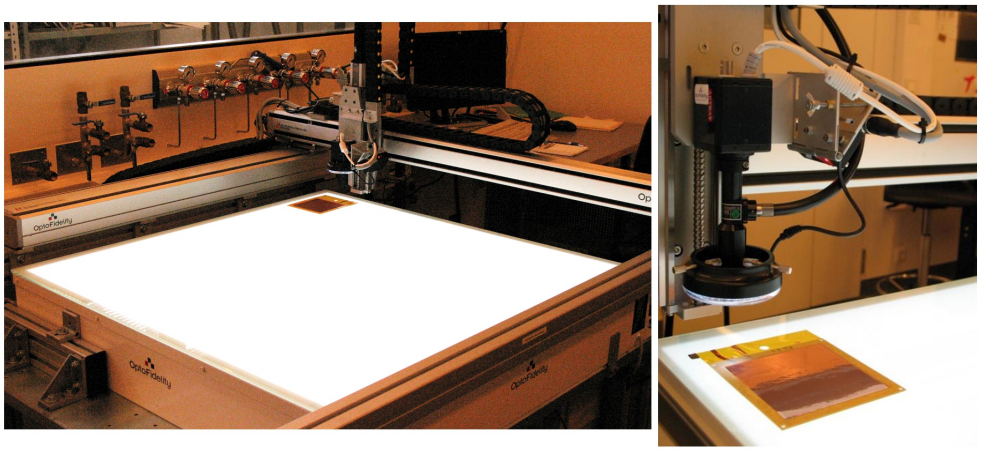

Figure 3.3: The Optical Scanning System in the clean room of the Detector laboratory at the Helsinki Institute of Physics and the University of Helsinki.

Visual inspection

Visual inspection is a commonly used method for quality assurance of various objects during manufacturing and assembly. As a rapid, non-contact QA technique, visual inspection complies with the strict requirements of maintaining the original surface quality at high hole-inspection rate.

An Optical Scanning System with 950 x 950 mm^2 scanning area was developed in the Detector Laboratory at Helsinki Institute of Physics and University of Helsinki [67]. Its main application of the OSS is visual control of the GEM foil hole parameters. The OSS also allows inspection of defects, some of which are: missing holes, enlarged holes, dirt inside the holes or etching defects (see Figure 3.1). These kinds of defects considerably reduce the lifetime of manufactured detectors.

An elaborate, state of the art instrument for high-resolution image taking, OSS set-up features $1.75\,\mu\mathrm{m}$ pixel size, 950 x 950 mm^2 scan area, and a projected inspection rate of (5 - 10) x 10^6 holes per day. The core of the system is a precision positioning xyz table with a carefully chosen set of optical components and light sources. A LabView based [69] software application controls the camera motion and monitors the image acquisition. Versatile and trustworthy software analysis and reliable calibration of the system optics are essential for usability of the set-up. Improving OSS operations and precision is one of the main focuses of this research.

The analysis software was first developed for accurate characterisation of GEM foil hole parameters, presented in Publication I. It was later supplemented with laborious

calibration procedure for the OSS. The improved and calibrated high-aspect ratio system guarantees accurate and traceable results, ensuring the quality and reliability of large area GEM foils in Publication III.

3.3.1 Software analysis for GEM foil inspection

The optical analysis of GEM foil images has been complicated because the reflectance of the foil surface varies between individual foils, see Figure 3.4. Several factors affect the precision accuracy of measurements from optical images: homogeneity of illumination, foil tilt, waviness and position in the light field (focus), surface reflectivity and roughness, rim roughness (the space between the inner d and outer D diameter of the GEM foil hole), and conical wall tilt. In particular, waviness along the z coordinate of the foil surface (due to wrinkles, see Figure 3.5) causes lighter/darker spots in the protruding/indented areas. This affects either part of the image or all of it and can make the image hard to analyse or altogether unsuitable for analysis.

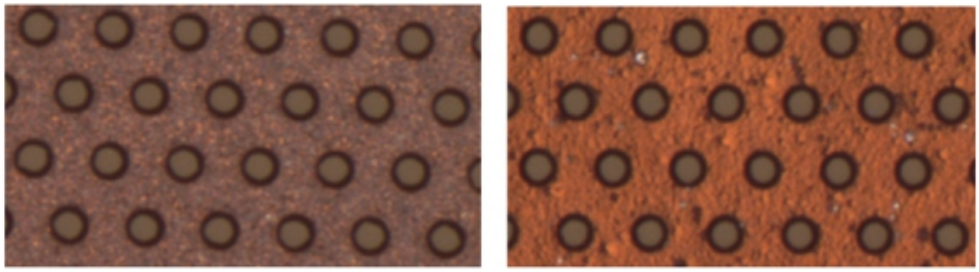

Figure 3.4: Images of two different GEM foils taken with OSS using in-line illumination.

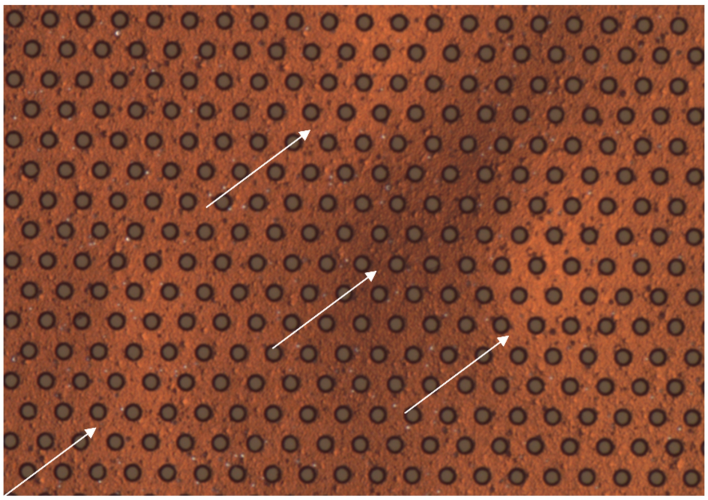

Figure 3.5: Darker and lighter areas observed during GEM foil scanning.

In order to extract foil characteristics from the highly variable input images, the software was designed to be as generic as possible in terms of image pre-processing,

segmentation and data analysis. This led to the creation of a software tool that is independent of the image quality in Publication I.

The software was tuned by comparing measurements made from both sides of a set of 5 GEM foils. The inner d and outer D diameters of the holes, the pitch P of the hole pattern and the difference between the length of the axes of an ellipse fitted to the hole boundary were used as the measured parameters. Measurement uncertainties for the parameters were found with a 2σ confidence level.

3.3.2 SEM traceable calibration of the Optical Scanning System

The absence of layer defects and the conformity of the GEM holes to specifications is important. Both hole size and shape influence the detector gas multiplication factor and hence affect the collected data. The required lateral measurement tolerance for the OSS is $\pm\,5\,\mu\mathrm{m}$.

Two actions need to be taken in order to calibrate the system, see Publication II:

- Determine the precision and accuracy with which one can calibrate the OSS for measuring one hole;
- Use this value together with an ensemble measurement to derive the calibration constant for an ensemble of holes occupying a large area.

In this study, we used a calibration sample with a surface comparable to that of the GEM foil [70] to confirm the tool calibration (see also Appendix A1). For this purpose, transfer standards (TS) were designed and microfabricated on an Si substrate. To guarantee accurate and traceable results, data was collected from the TS with a calibrated SEM device and later compared to the corresponding OSS images (see Figure 3.6).

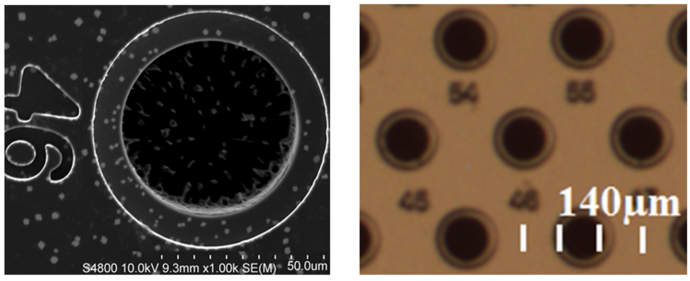

Figure 3.6: SEM (left) and OSS (right) images of the same TS cavity.

Strict requirements were applied to the TS design, illustrated in Figure 3.7:

- The TS layout should replicate the hole pattern in the GEM foil, the hole size, the pitch (P) between the hole centres and the rim roughness of the inner (d) and outer (D) diameter.
- The TS should permit calibration of a single cavity image (calibrated microscopy) as well as calibration of the cavity matrix image.

- Non-destructive methods must be used for TS calibration.
- The calibration procedure must be traceable to standards.

TS manufacturing technology can produce patterns simulating the holes and pierced matrix in the GEM foil [19]. It also provides standards with similar optical reflectance to that of GEM foils. This is important because the calibration depends on the surface properties of the sample [60]. For example, oxidation, chemical residue from the manufacturing process, dust particles or surface artefacts that often can be caused by scratches on the foil surface.

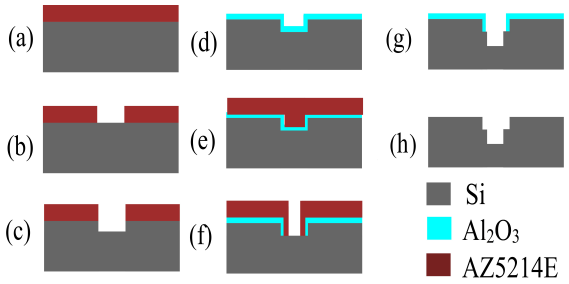

Figure 3.7: Process flow of the Si TS manufacturing: (a) spin coating of AZ5214E photoresist, (b) laser writing, (c) cryogenic Deep Reactive Ion Etching, (d) deposition of Al_2O_3, (e) spin coating of AZ5214E photoresist, (f) laser writing and BHF (etching agent) removal of Al_2O_3, (g) etching of $5\,\mu m$ deep cavities by Bosch process, (h) etching of $50\,\mu m$.

Forty-five cavities were chosen from the TS to be examined (see Appendix A1). A calibration check of the SEM was first performed and the TS cavities were then scanned. The same cavities were examined by OSS in nine positions on the scan area, as illustrated in Figure 3.8. The obtained results were analysed and the d and D of the TS cavities were determined (see Table 3.1). Uncertainties were calculated at the 2σ level to show that the OSS method provides results consistent with those provided by SEM (see Appendix B). Cavities with apparent etching defects were not analysed.

Figure 3.9 presents the absolute difference in d measured by SEM and OSS before (BC) and after (AC) applying the calibration factor of $1.01 \pm 0.01\ (2\sigma)$. Figure 3.10 presents the absolute difference in D measured by SEM and OSS before and after calibration with a calibration factor of $0.99 \pm 0.01\ (2\sigma)$. The comparison of the OSS data to the SEM data determines how close OSS is to the correct value (accuracy). The uncertainty of our measurement (precision) was calculated at a 95 % confidence level.

The uncertainty in d and D for each hole measurement was defined as required in [60–63] (see Appendix B). The uncertainty of the measurement of the SEM calibration specimen was combined with the uncertainty of the measurement of the d and D obtained with both devices. The OSS calibration factor was derived, for d and D, by linking the SEM and OSS results using the ratio of the two results.

Table 3.1: Inner (d) and outer (D) diameters of TS cavity #46 .

Parameter	Before OSS calibration (µm)	After OSS calibration (µm)	SEM (µm)
d	53.06 ± 0.74	53.56 ± 0.75	53.64 ± 0.88
D	71.89 ± 1.03	71.35 ± 1.03	71.57 ± 0.68

The most important result is that accurate imaging was achieved across a large TS area and, by implication, can be achieved for a large GEM area if one can guarantee that the GEM foil sandwich structure remains as flat and as homogeneous in reflection as the silicon TS. The diameter measurements (OSS) exhibited an uncertainty of $\pm$ 1.03 µm. These results were consistent with those provided by SEM.

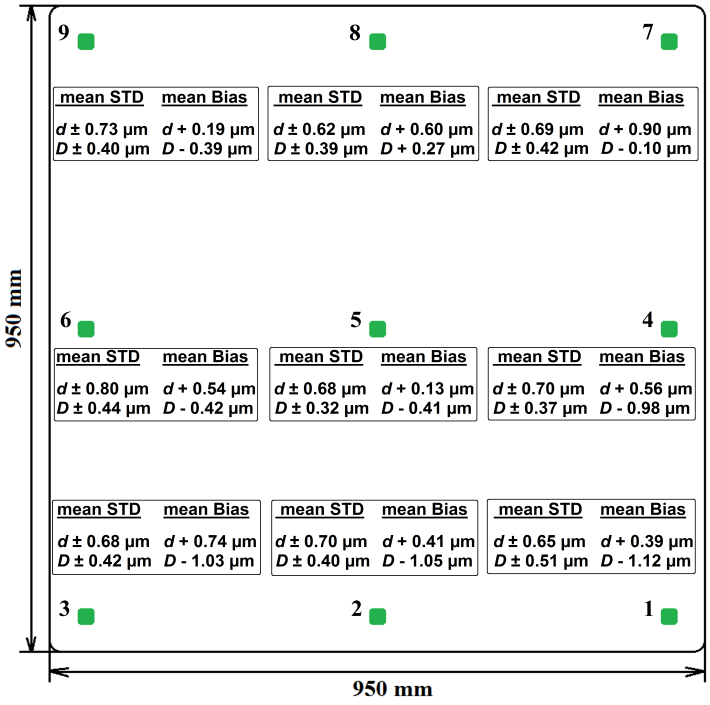

Figure 3.8: The nine positions across the test bed used to calibrate the OSS.

In practice, it was shown that the OSS performs quantitative microscopy (distortion-free imaging after calibration) as well as area surveying (distortion-free translation and imaging after calibration). The calibration was successful across a 950 x 950 mm^2 area for the narrow range of d and D values present in the TS.

The most serious limitation with this general approach comes from the fact that both employed methods, OSS and SEM, are essentially 2D methods used to examine 3D objects with two diameters (d and D), whose recorded values depend on maintaining precise focus distance control along the z-axis. Controlling focal distance across large area scans (tight auto focusing) is non-trivial. Moreover, in the current OSS

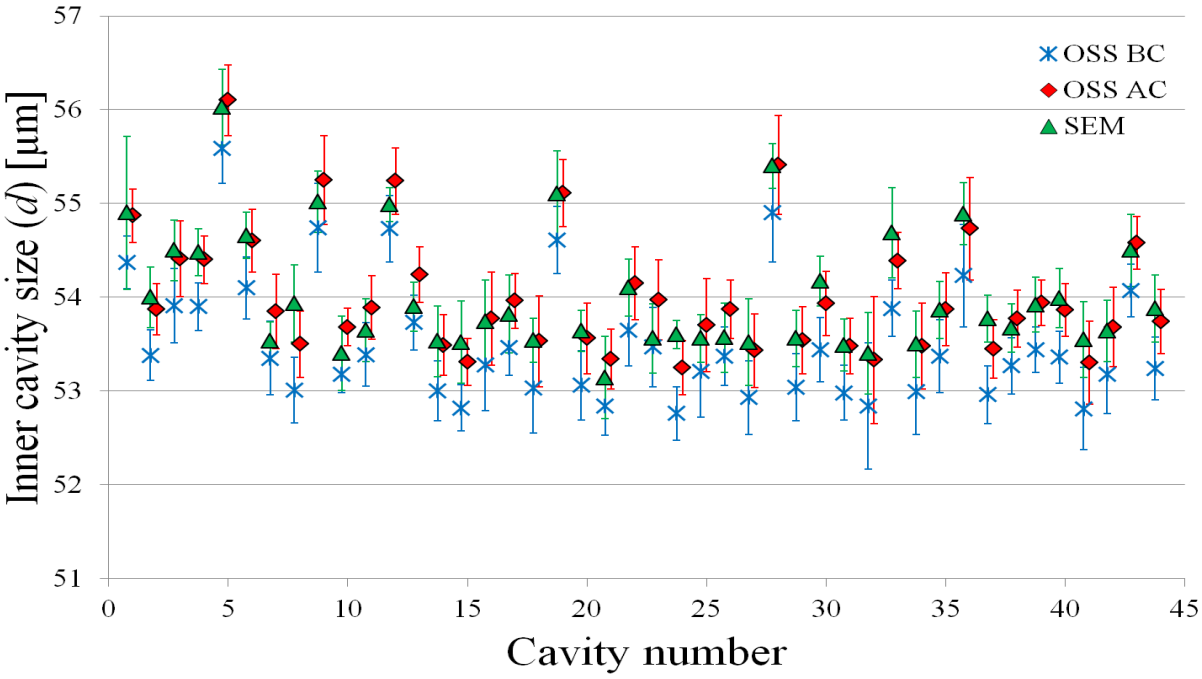

Figure 3.9: The 44 inner cavities d in TS measured with SEM and OSS before (BC) and after (AC) calibration. A small shift along the x axis was applied to the AC data points for better readability.

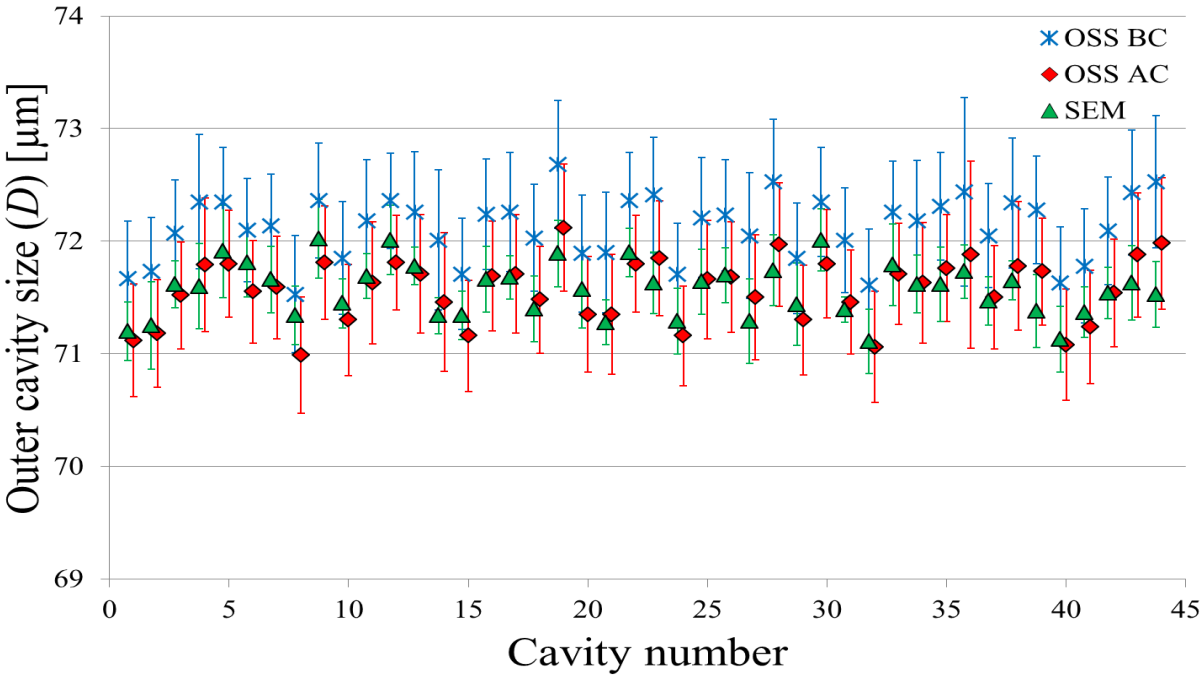

Figure 3.10: The 44 outer cavities D in TS measured with SEM and OSS before (BC) and after (AC) calibration. A small shift along the x axis was applied to the AC data points for better readability.

set-up, an axial limitation (along the z-axis) was observed due to limitations in the camera pixel size ($1.75\,\mu\mathrm{m}$), magnification of the optical system (1X) and illumination wavelength ($\approx 0.5\,\mu\mathrm{m}$). Each of these factors also affects the OSS image quality and consequently the accuracy of the d and D estimates, which are at the core of the QA process. A tight auto-focus needs to be maintained during large, fast motion; the precision and accuracy of the OSS depends on the focus. This could cause results to be inaccurate.

3.3.3 SWLI traceable calibration of the OSS

A more thorough OSS calibration was performed using a piece of GEM foil as TS in Publication III. The new TS was examined with the OSS and the results compared with those obtained with a 3D high-resolution non-contact imaging system. The resulting calibration improved the performance accuracy of the OSS measurements. The 3D imaging system allows a detailed study of the complete GEM-hole geometry, not only the GEM foil surface (see Section 3.3.4).

A GEM foil sample, similar to the one illustrated in Figure 3.11, was created from a larger GEM foil of the type under QA assessment so that the foil characteristics (hole size, foil surface roughness and reflectivity) were accurately reproduced. The TS was used to link the OSS to our Scanning White Light Interferometry (SWLI) device [71]. In this manner, traceability of the OSS calibration via the SWLI was established (calibrated dynamically and statically at the Finnish Centre for Metrology and Accreditation (MIKES)) [72].

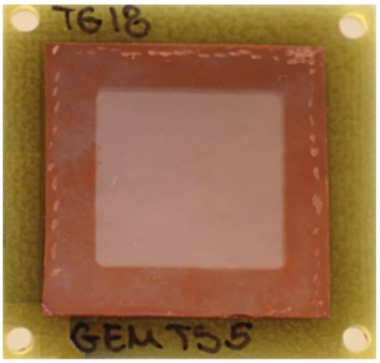

Figure 3.11: GEM foil 2.5 x 2.5 cm^2 sample.

By verifying the data obtained with the OSS results against data from a calibrated SWLI device (see Appendix A2), it was assured that both individual holes and ensembles of holes were correctly imaged to guarantee accurate and traceable results. Measurement and data extraction procedures similar to those of Section 3.3.2 were used.

Figure 3.12 presents the values for d measured by the SWLI and the OSS after applying the calibration factor of 1.05 ± 0.01 (2σ). Figure 3.13 presents the values for D measured by SWLI and OSS after calibration with a calibration factor of 0.96 ± 0.01 (2σ). The expanded uncertainty at 95 % confidence level was $\pm 0.67\,\mu\text{m}$

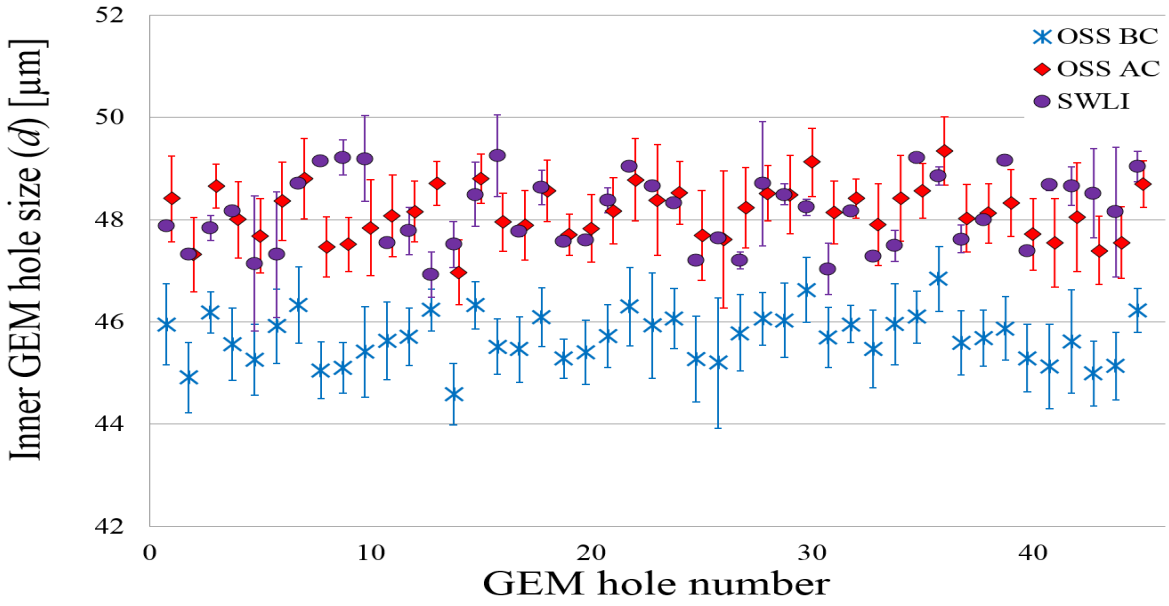

Figure 3.12: The 45 inner GEM foil holes d measured with SWLI and OSS before (BC) and after (AC) calibration. A small shift along the x axis was applied to the AC data points for better readability.

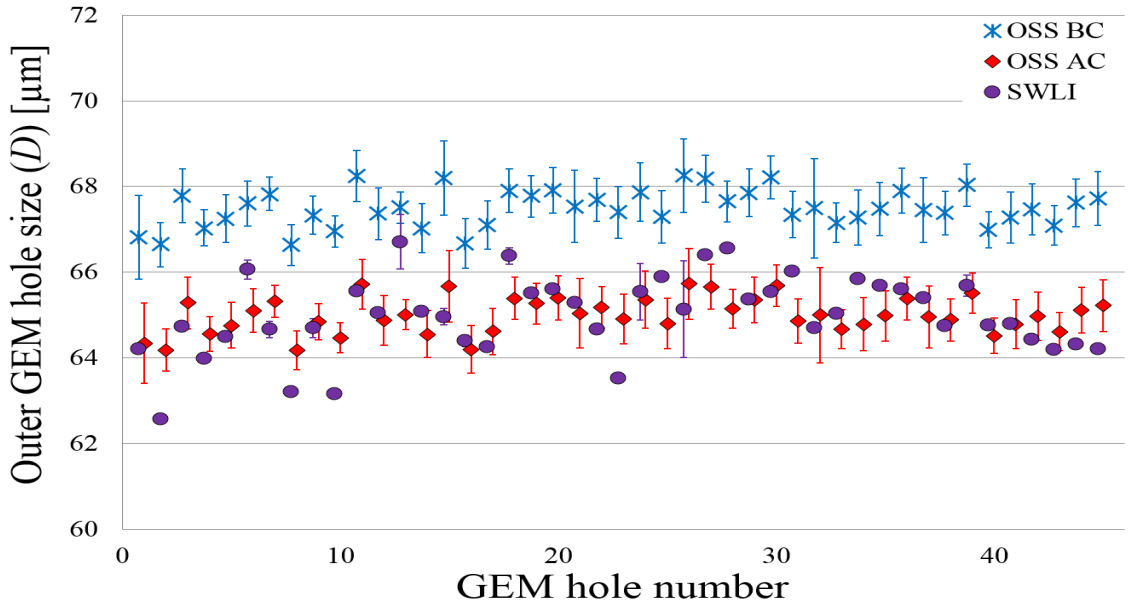

Figure 3.13: The 45 outer GEM foil holes D measured with SWLI and OSS before (BC) and after (AC) calibration. A small shift to the AC was applied for better differentiation.

(reduced by 65 % relative to the study presented in Section 3.3.2 and in Publication II). This reduction is due to the fact that the two studies used different TS. Both *d* and *D* measured by OSS agree with the SWLI results.

The uncertainty in *d* and *D* for each hole measurement was defined as required in [60–63] (see Appendix B). The uncertainty of the measurement of the SWLI calibration specimen was combined with the uncertainty of the measurement of the *d* and *D* obtained with both devices. The OSS calibration factor was derived for *d* and *D* by linking the SWLI and OSS results using the ratio of the two results.

3.3.4 GEM foil hole geometry

There are no detailed studies in the literature on the shape and size of GEM foil holes. Up to now, the holes have been assumed to be perfectly hourglass-shaped [41] and only nominal hole shapes have been simulated [73]. There are papers reporting on both simulations and real measurements regarding the optimal hole size for high gain [41, 74, 75]. In these cases, all holes were assumed to be identical. Most of the previous research on detector gain focuses on the gas mixture and pressure, as well as the applied voltage rather than the actual hole shape [76–78].

Detailed 3D imaging of GEM foil hole geometry, the first of its kind, was realized at HIP and described in Publication IV. The GEM foil sample shown in Figure 3.11, and high-resolution SWLI [71], were used for a detailed examination of the geometry of GEM foil holes. Both sides of the sample were examined. In addition to the standard GEM hole parameters (*d* and *D*), four new parameters were introduced and studied in detail — the shift (*S*) between the centres of the inner and outer diameters, illustrated in Figure 3.14, the total foil thickness (*T*) and metal (T_m) and polyimide (T_p) thicknesses, shown in Figure 3.15 and Figure 3.16, respectively. Table 3.2 presents the top and bottom parameters obtained for the GEM foil sample hole #8.

The contour extraction method (see Figure 3.14) was used to study the variation in the diameter of the holes located in one small area of the GEM foil sample. Figure 3.17 presents a comparison for the top and bottom *d* measured with SWLI for all 25 chosen holes from the GEM foil sample, whereas Figure 3.18 presents the same comparison but for the top and bottom *D*.

Although there was fluctuation between the top and bottom *d* values, they all were within the manufacturing tolerance for the GEM foil ($d = 50 \pm 5$ µm). However, the values obtained for *D* were systematically smaller (-6.1 µm on average for both the top and the bottom sides) than the nominal value (70 ± 5 µm).

The contour extraction method confirmed the observed shift *S* between the centres of the top and bottom holes determined by SWLI; see Figure 3.14 (right). Figure 3.19 shows a comparison of *S* between *d* and *D* on the top and bottom sides measured with

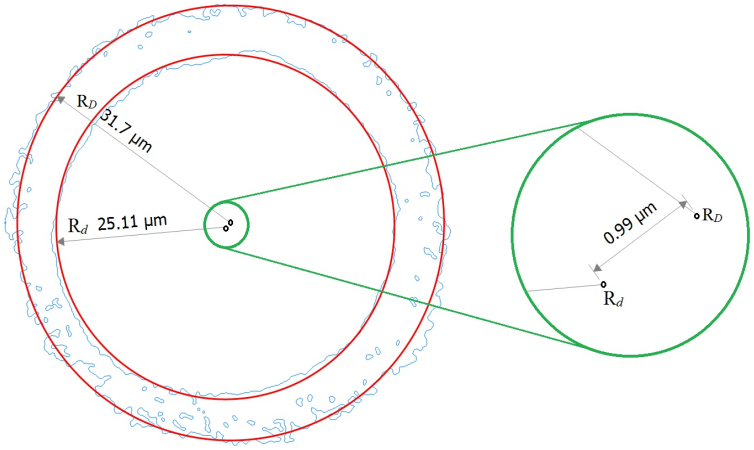

Figure 3.14: Inner (d) and outer (D) diameter obtained by the contour fit and radii extraction method used in the MountainsMap software [79] (left). The measured shift S between the centres of d and D (right) was $0.99\,\mu\mathrm{m}$ for one of the 25 examined holes.

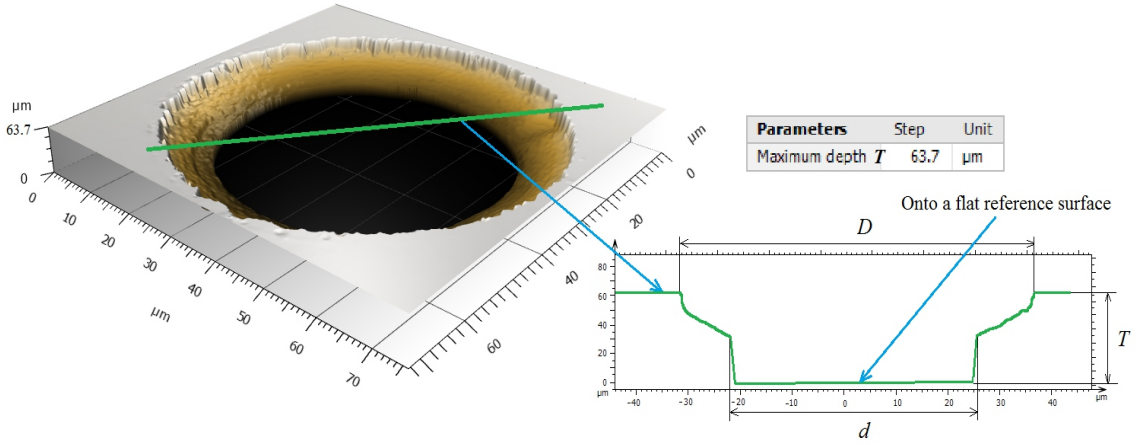

Figure 3.15: MountainsMap software step height feature used in the study of the total thickness T of the GEM foil sample.

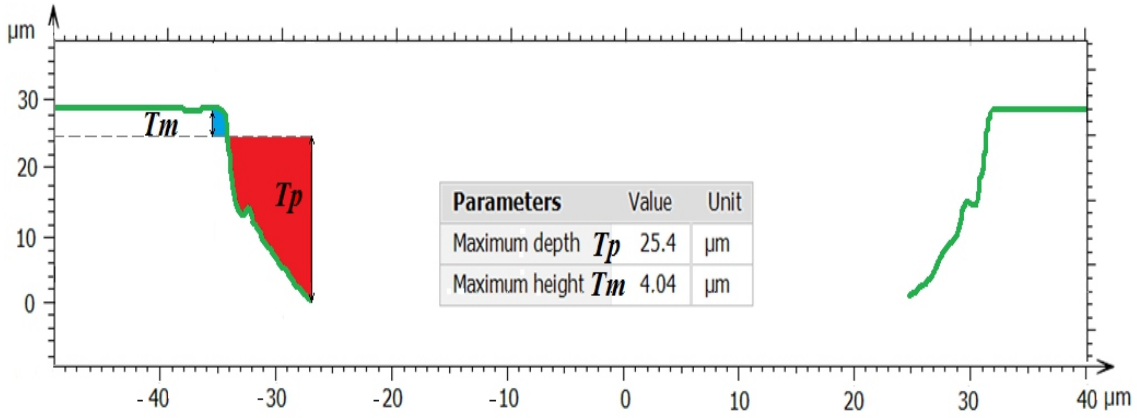

Figure 3.16: MountainsMap software step height feature used in the metal (T_m) and polyimide (T_p) thickness study of the GEM foil sample.

SWLI for the 25 holes of the GEM foil sample. The plot indicates that holes #5 and #22 feature a relative top and bottom side shift of $3\,\mu m$. The impact of such a large shift was studied using simulation and the results are shown in Section 3.3.5.

Table 3.2: SWLI measured top and bottom parameters of GEM foil hole #8 with total thickness T of 63.17 ± 0.07 µm. The presented errors have a coverage factor k = 2.

Parameter	Top (µm)	Bottom (µm)
d	51.18 ± 0.28	51.16 ± 0.04
D	62.81 ± 0.37	63.15 ± 0.11
S	0.22 ± 0.07	1.41 ± 0.14
T_m	3.64 ± 0.55	3.28 ± 0.42
T_p	22.96 ± 1.01	23.35 ± 0.75

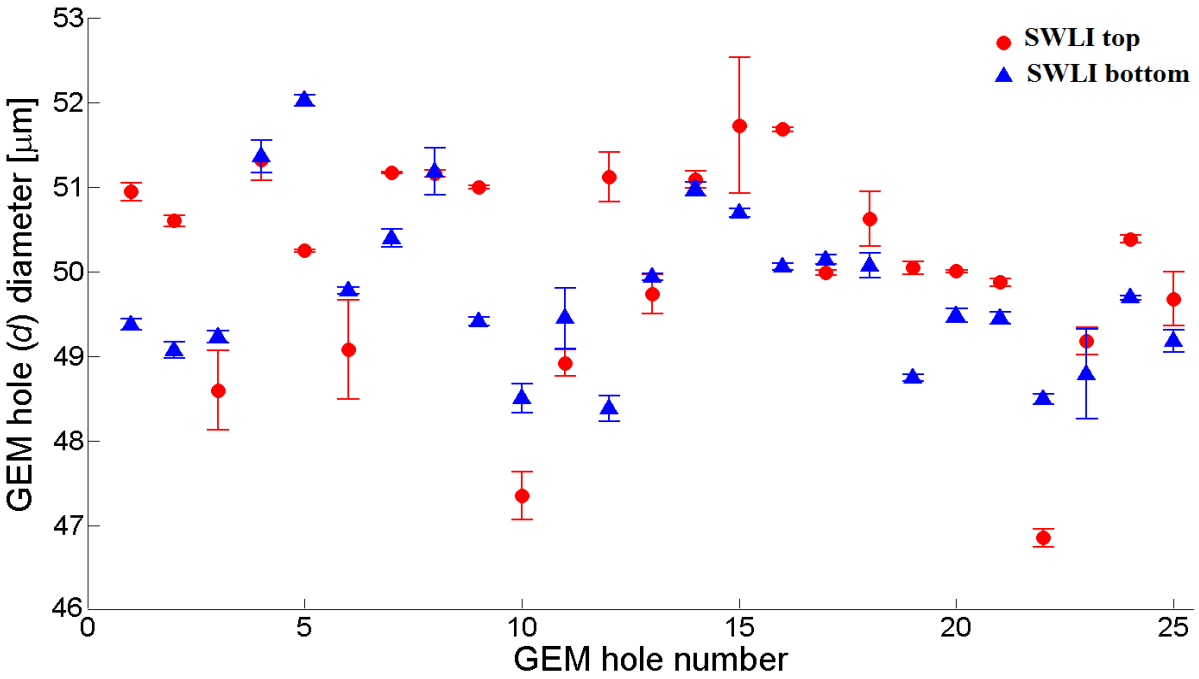

Figure 3.17: The 25 inner holes d values measured with SWLI (see Figure 3.14) in the GEM foil sample.

It was possible to determine the total foil thickness T, as well as the thickness of the metal T_m and polyimide layers T_p, using the high-vertical resolution of the SWLI. Figure 3.20 shows the total thickness T measured with SWLI for the 25 holes of the GEM foil. The T values ranged from 62.30 to 65.60 µm. The thickness of the GEM foil, close to most of the examined holes, was $5.6\,\mu m$ larger than the nominal thickness (60 ± 3 µm).

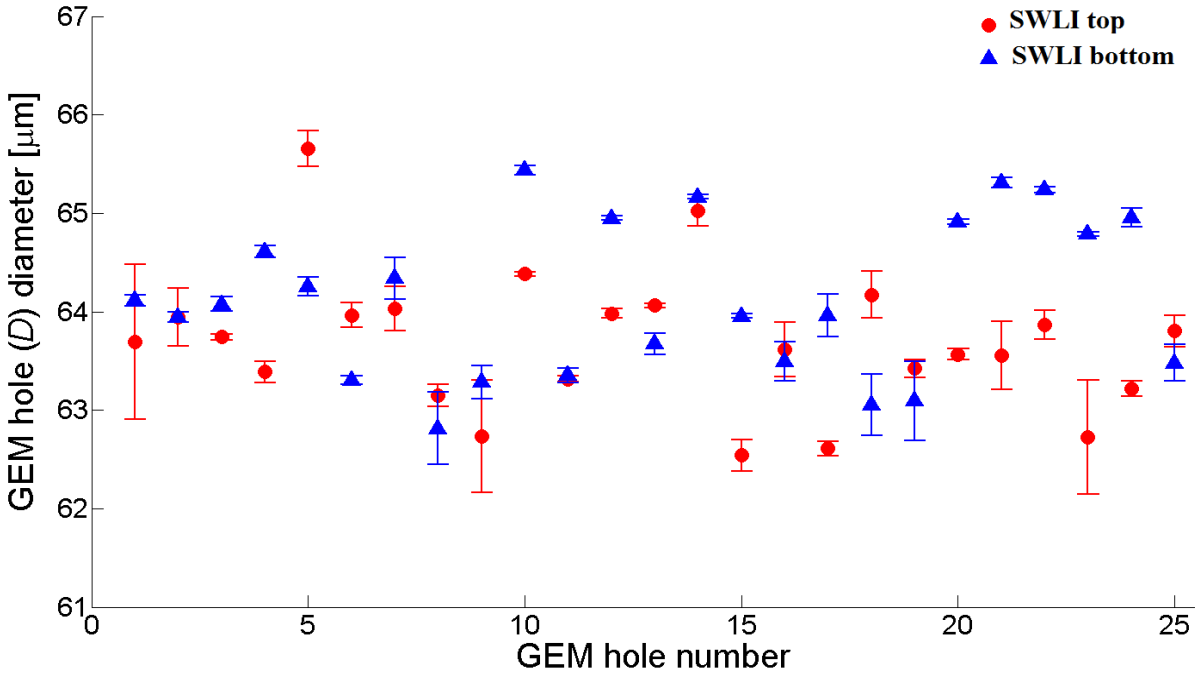

Figure 3.18: The 25 outer hole D values measured with SWLI (see Figure 3.14) in the GEM foil sample.

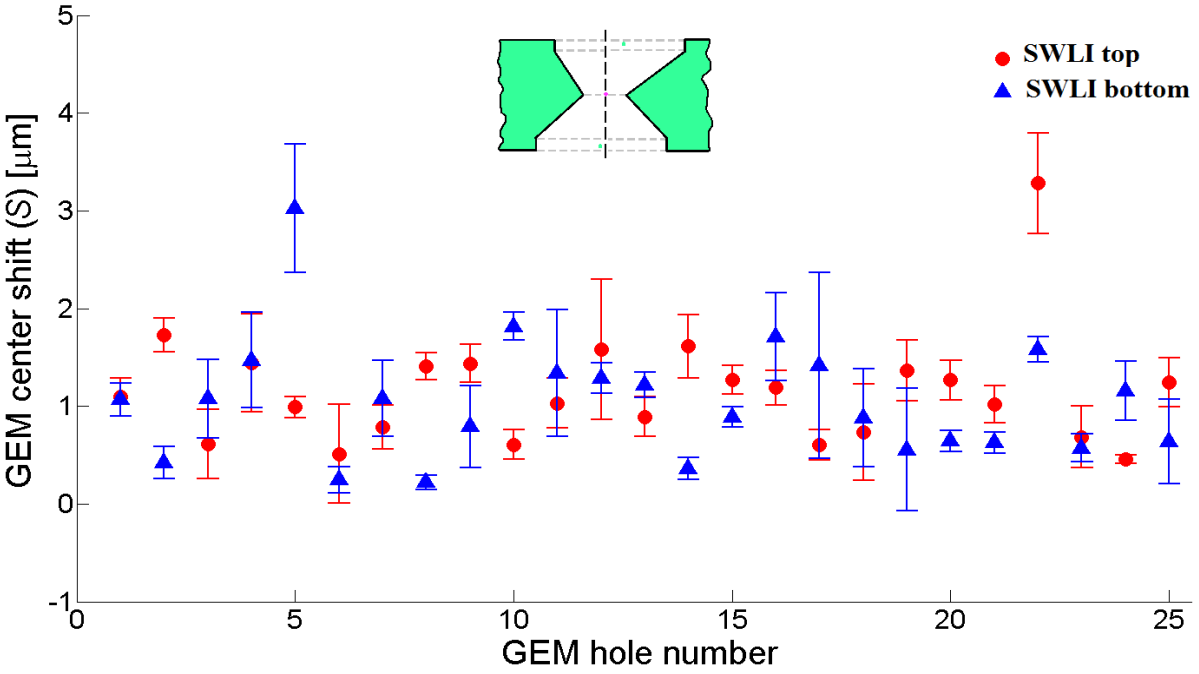

Figure 3.19: SWLI comparison of the shift S between d and D on the top and bottom side for the 25 holes in the GEM foil sample.

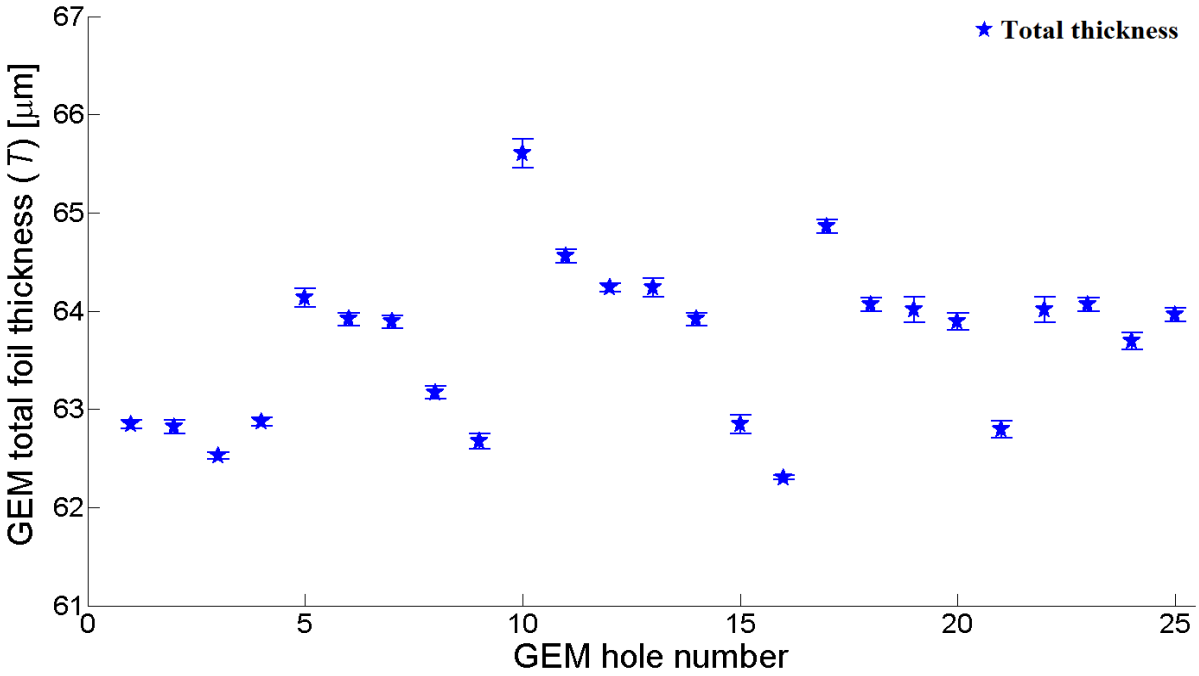

Figure 3.20: SWLI results for the total foil thickness T (see Figure 3.15) around the 25 holes in the GEM foil sample. The nominal foil thickness is 60 ± 3 µm.

This QA method is slow if used to examine a 10 x 10 cm^2 GEM foil. However, knowing the real hole geometry could help to improve the GEM fabrication process, which could lead to better detector performance. Improving GEM foil fabrication is important because, on the basis of [41] and [64–68], it can be assumed that the characteristics of the GEM foils strongly affect the behaviour of the GEM detector. The results from the examined GEM foil sample indicate a probable mask misalignment during the foil fabrication.

3.3.5 Detector gain simulation based on hole geometry

To determine the effect of GEM hole geometry variations, the ANSYS [80] and Garfield ++ [81] software packages were employed to simulate the GEM detector gain performance on the basis of the SWLI measured data, see Publication IV. Two separate simulations studied variations in the geometry of hourglass-shaped holes and variations based on the geometry of real holes.

Hourglass-shaped holes - This study focused on an hourglass-shaped hole simulation with a nominal d and D (50 ± 5 µm and 70 ± 5 µm), T of 60 ± 3 µm, and pitch P of 140 µm. The study included 70 different shape variations of the GEM foil holes. The five basic scenarios are shown in Figure 3.21.

First, the nominal hourglass hole geometry (#1) was simulated and its effective gain was studied. After that the top part of the hole was kept static while the bottom part

was moved from the centre to the left and then from the centre to the right by 1 µm steps in a total range of -5 to 5 µm (scenario #2 in Figure 3.21). The same was done for the scenario #3, but the bottom part of the hole was kept static. Finally, scenarios #4 and #5 were studied, where both parts of the hole were moved in opposite directions by 1 µm steps in a total range of -5 to 5 µm.

Figure 3.22 presents the variation in the effective gain obtained with Garfield ++ for different shapes of a single hole in a GEM foil with uniformly shaped holes. In scenarios #1 to #5 a drop of up to 7 % in the effective gain was observed compared to the effective gain of the nominal hourglass-shaped hole. Figure 3.23 shows the percentage of electrons produced near the exit electrode that do not contribute to the effective gain. A 7 % maximum increase was observed within the studied scenarios.

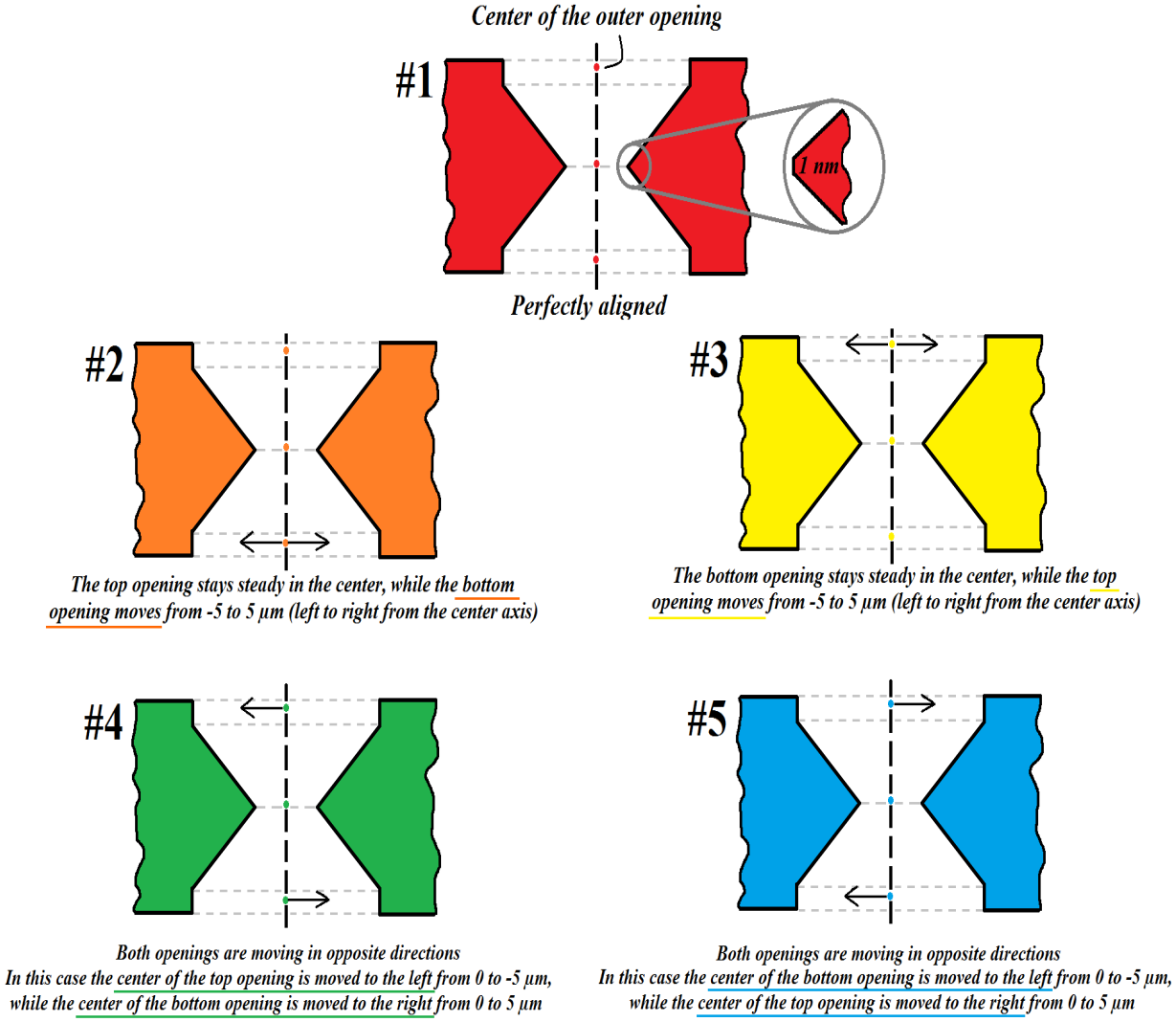

Figure 3.21: Simplified side view of the five basic scenarios: #1 - original hourglass-shaped hole; #2 - top opening stays static, bottom moves; #3 - top opening moves, bottom stays static; #4 and #5- top and bottom move in opposite directions.

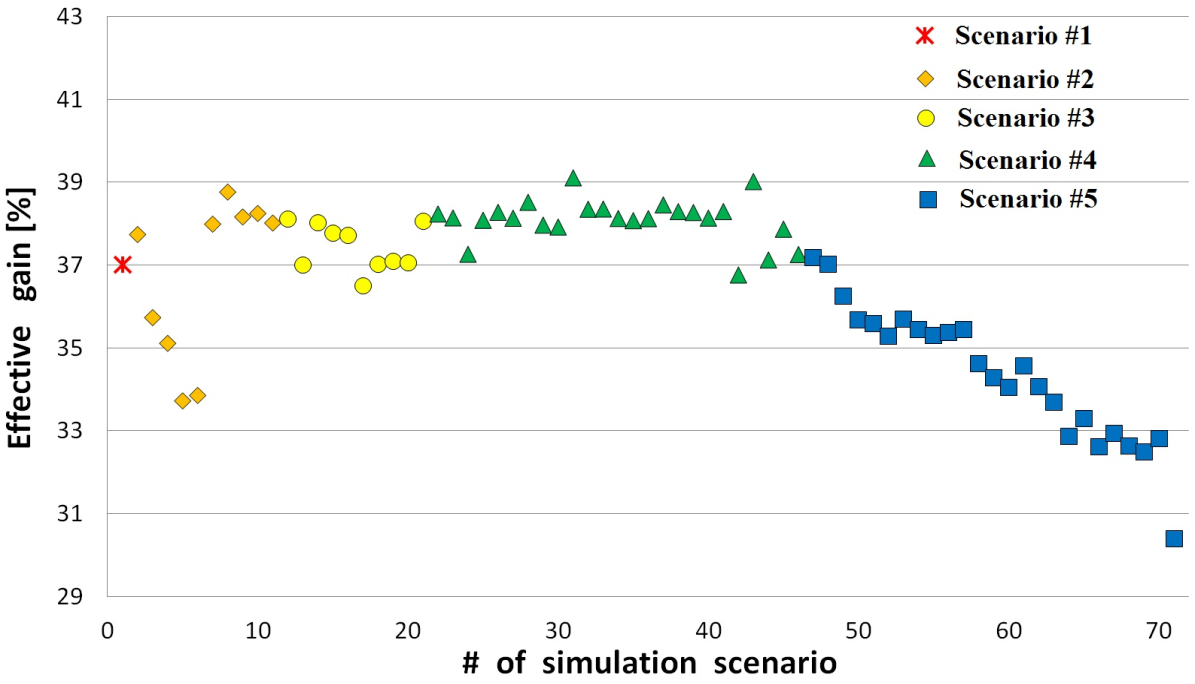

Figure 3.22: The simulated effective gain of the GEM foil holes ($G_{tot} = G_{eff} + G_{Neff}$). The nominal hourglass-shaped hole compared to the 70 scenarios of differently shaped holes. See Figure 3.21 for the colour codes.

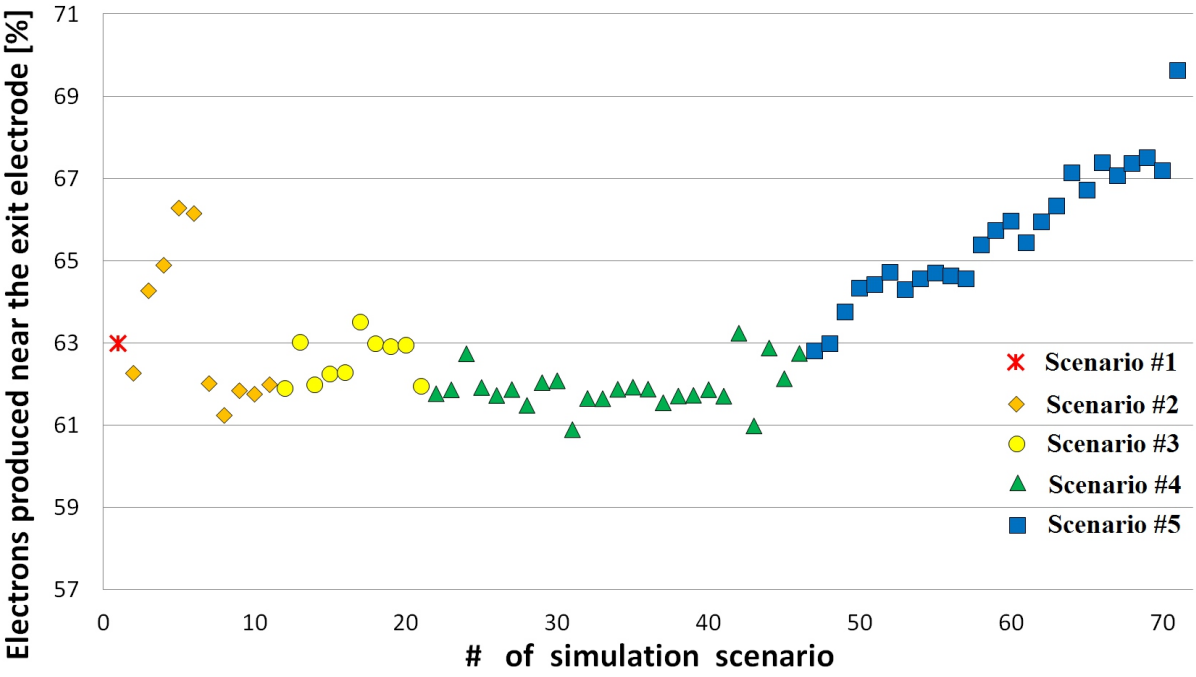

Figure 3.23: The electrons produced near the exit electrode ($G_{tot} = G_{eff} + G_{Neff}$). The nominal hourglass-shaped hole compared to the 70 scenarios of differently shaped holes. See Figure 3.21 for the colour codes.

The total number of electrons produced in the avalanche is refereed to as total gain (G_{tot}). In the case of the first marker on Figure 3.22 the effective gain is G_{eff} = 37 % of the total gain. Although electrons are predominately (G_{Neff} = 63 %) produced near the exit electrode (the first marker on Figure 3.23), only the electrons produced in the centre of the hole contribute to the effective gain of the detector. Therefore the anti-correlation between the two plots.

Real shape holes - During the SWLI GEM hole parameter extraction (see Section 3.3.4), values different from the nominal GEM hole were observed for the top and bottom sides of the foil. A study of the effective gain as a function of the measured GEM foil hole shape was then performed. ANSYS was used to recreate the GEM foil on the basis of the SWLI data from 10 holes of our GEM foil sample (see Figure 3.11).

These 10 holes were randomly chosen from the 25 holes examined with the SWLI. They were divided into three categories: A - deviation in all hole parameters with more than $1\,\mu\mathrm{m}$ of the nominal values - see Figure 3.14 and Table 3.2; B - top and bottom hole elements with a shift S of more than $1\,\mu\mathrm{m}$ from the centre of the hole (relatively similar top and bottom shift); C - difference of more than $1\,\mu\mathrm{m}$ between the top and bottom opening shift (imbalanced top and bottom shift). The hole shapes shown in Figure 3.24 present (from left to right) the hourglass-shaped hole with nominal values and the replicated GEM foil holes from categories B and C with their parameter values as measured with SWLI.

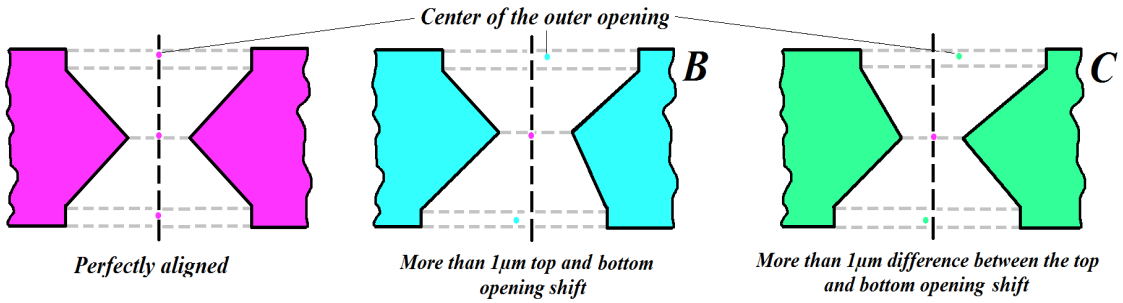

Figure 3.24: Simplified side view of the B and C GEM foil hole categories. See Figure 3.14 for an A category GEM foil hole.

Figure 3.25 illustrates the simulated effective gain (left) compared to that of the nominal hourglass - shaped hole foil and the electrons produced near the exit electrode (right) for 10 real GEM foil hole geometries. The same anti-correlation between the two plots was observed.

Each simulated scenario assumed a fixed size and shape for all of the holes in the GEM foil. For example, each marker in Figure 3.22, Figure 3.23 and Figure 3.25 represents a foil with identical holes. A GEM detector gain evaluation on the device level could be performed for a set of differently shaped and sized holes over several GEM

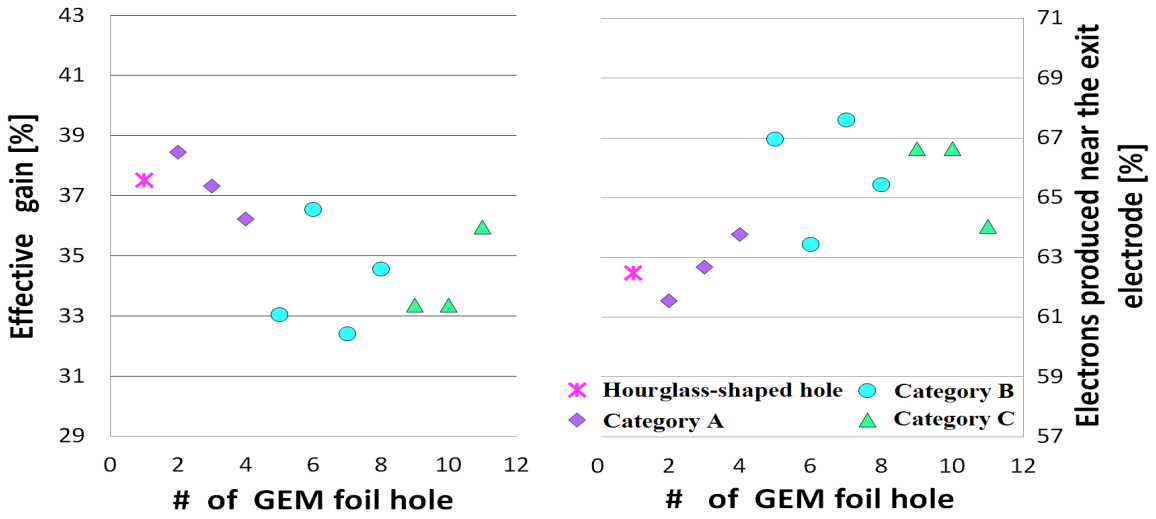

Figure 3.25: Simulated results based on 10 SWLI measured GEM foil hole geometries. The magenta marker is for the hourglass-shaped hole and diamond purple, circle cyan, and triangle green are for the A (see Figure 3.14), B, and C categories (see Figure 3.24), respectively.

foil detectors. It is likely that the effective gain could significantly vary if a foil with holes of different shapes and size were simulated. The effect of the rim roughness should also be examined since the sharp points concentrate the electric field.

The simulated results indicate that the real GEM foil performance could differ from the design performance by as much as a 6 % increase in the electron production near the exit electrode of the GEM foil with a 4 % lower effective gain. Thus, the four new parameters introduced to characterise GEM foil holes in these studies should be included in the quality assurance process during GEM foil manufacturing. The results prove that the hole geometry affects the gain performance of the GEM detectors. The recorded effect, though small, may be important since the simulated cases use uniformly shaped holes along the GEM foil. As demonstrated in this study, a real GEM foil will always contain holes of different shapes and sizes.

3.4 Solid-state detectors

The same two QA techniques were also employed to ensure the reliability of various solid-state particle detectors in Publications VI and VII and their connecting elements in Publication V. The quality of silicon pixel ans strip detector modules depends on the quality of the readout chip, the sensor chip, and the connections between them. The connection can be done by wire bonding (strip) or flip-chip (pixel) technology [57].

Visual inspection was used to confirm the height of the soldering bumps that form the connections between the sensing element and the readout chips in the pixel de-

tector module. In addition, electrical characterisation was used to evaluate the basic electrical parameters of the sensing element itself. The accuracy and the sensitivity of both QA techniques are important to ensure the quality and integrity of the particle detectors. Therefore, a calibration measurement check was performed before each measurement session on the inspection systems used.

3.4.1 Visual inspection of flip-chip interconnections

The Helsinki Institute of Physics has several commitments at CERN [5]. In collaboration with Advacam Oy [82], 250 silicon pixel detector modules have been bump-bonded (see Figure 2.9) and characterised for the Phase I upgrade of the Barrel Pixel detector of the CMS experiment [12]. Successful, reliable, timely, and economical manufacturing of these modules to be installed during the end of 2016 requires reliable and accessible quality assurance methods.

The uniformity of the height of the solder bumps was studied using SWLI, see Publication V, according to the flip-chip bonding pixel detector module requirements in [83]. The SWLI was chosen once again as a visual inspection tool. Its full-field-of-view, non-contact measuring methods and high-vertical resolution make it a suitable instrument for the visual inspection of the pixel detector module. Calibration SiO_2 spheres, shown in Figure 3.26, were used to determine the uncertainty of the SWLI set-up when characterising spherical surfaces. Produced by Corpuscular Inc. [84], the spheres feature a National Institute of Standards and Technology (NIST) [85] certified diameter of 20 ± 1.2 µm.

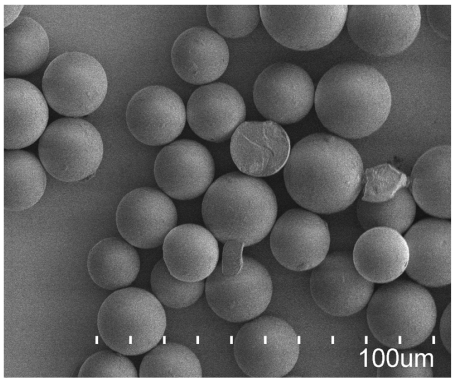

Figure 3.26: An example of NIST calibrated SiO_2 spheres imaged with SEM.

Imaging spherical objects is a challenging task because their curvature causes the reflected light to be lost. Therefore, one can only see part of the spherical object due to its steep slope. Thus, only the very top of the spherical objects was used to extract the maximum height of the calibration spheres and the soldering bumps.

The studied solder bumps were deposited at Advacam Oy using the bump manufacturing technique presented in Section 2.2.2.2. The high-vertical resolution of the SWLI allows us to perform precise height measurements of the soldering bumps. The MountainsMap software step height feature, illustrated in Figure 3.27, was used to determine the maximum height of the soldering bumps by extracting their profile.

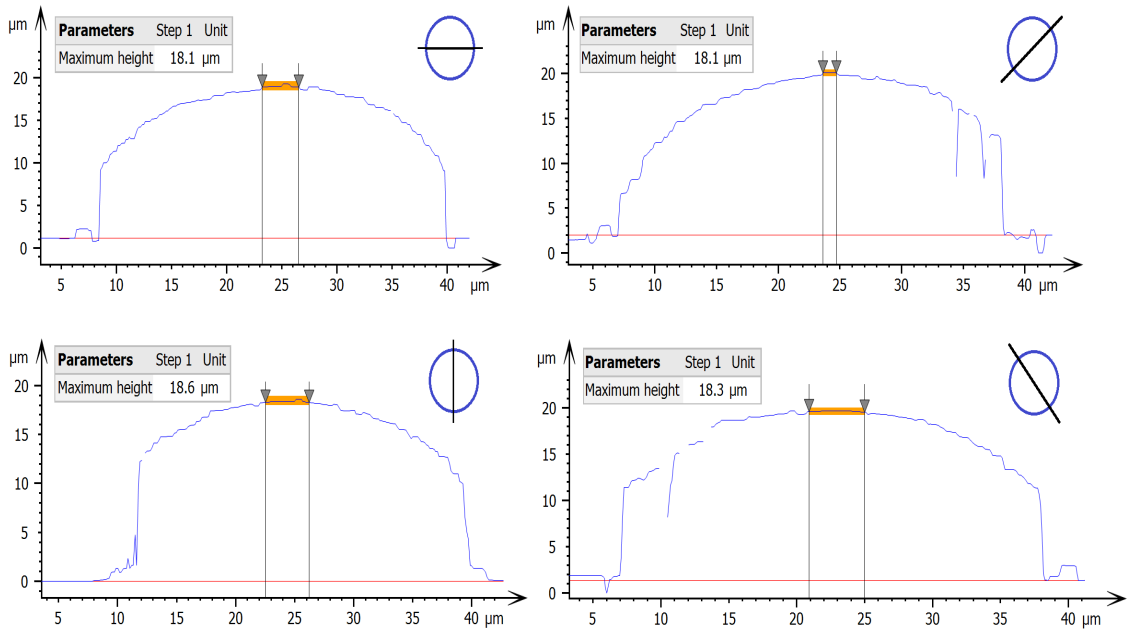

Figure 3.27: The MountainsMap software step height feature used in the maximum height H study of the solder bumps.

Nine neighbouring bump-bonds were randomly chosen for examination. The SWLI was used to scan the bump surface three times. The MountainsMap software step height feature was used for the extraction of four profiles across the summit of each bump, separated by 45° (see Figure 3.28).

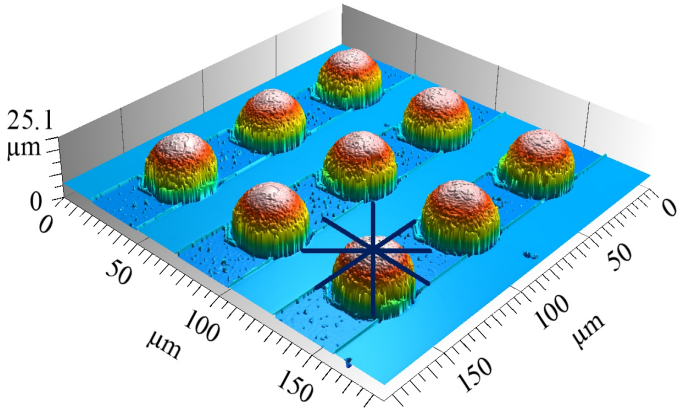

Figure 3.28: 3D reconstruction of the nine neighbouring bumps imaged with SWLI. The polar grid showing the profile extraction is indicated in dark blue.

The maximum height H of each bump was calculated as an average of 12 profiles (9 soldering bumps x 1 height x 4 profiles x 3 times = 108 measurements). Table 3.3 contains an example of the maximum height data for the bump #5.

Table 3.3: SWLI maximum height H measurement of bump #5.

Profile	Before SWLI calibration (µm)	After SWLI calibration (µm)
0°	18.03 ± 0.31	17.63 ± 0.31
45°	18.60 ± 0.30	18.19 ± 0.31
90°	18.03 ± 0.31	17.63 ± 0.31
135°	17.90 ± 0.27	17.50 ± 0.27

Figure 3.29 shows the average maximum height for the nine bumps, after applying the SWLI measurement correction of $+\ 0.98\,\mu\text{m}$ corresponding to the SLWI pixel size obtained during the NIST sphere measurements, as required by UKAS M3003 [62] and GUM JCGM 100:2008 [63]. The maximum height of the bumps was determined to be in range of 17.63 - 18.76 µm, which falls within the $\pm\ 1\,\mu\text{m}$ typically achieved tolerance.

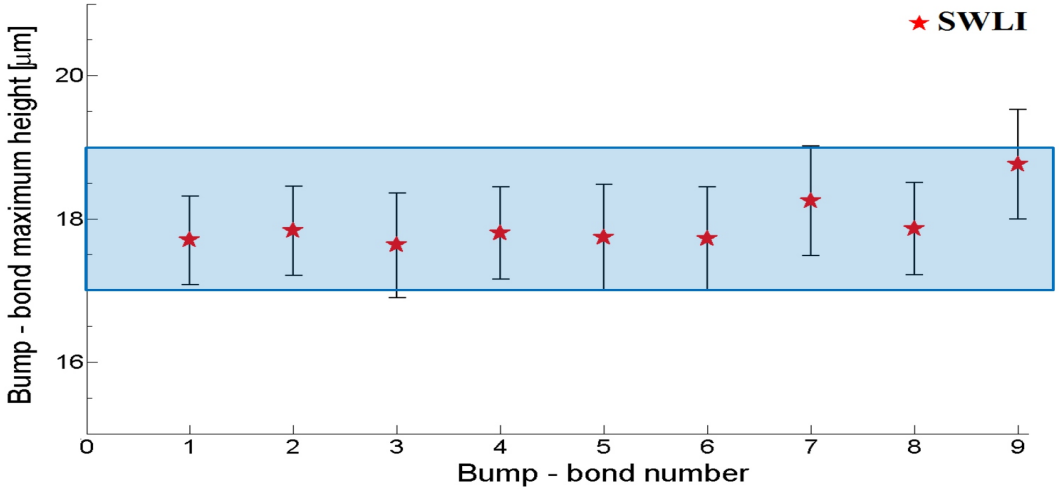

Figure 3.29: Measured maximum height H of the 9 bumps. The typical specification boundaries ($\pm\ 1\,\mu\text{m}$) are indicated in blue.

3.4.2 Electrical characterisation of solid-state detectors

The electrical characterisation of solid-state detectors usually relies on fast and non-destructive measurement techniques and provides insights into the general detector characteristics. A reverse bias voltage is applied over the detector. The device leakage current and depletion voltage are measured by a semi-automatic probe-station, as illustrated in Figure 3.30, placed inside a dark, controlled environment (temperature of 22 ± 1 C° and humidity of 21 ± 2 %, measured by a monitoring system). The obtained

results can be used, for example, for quality control, irradiation and ageing studies, comparison of different manufacturing methods and many other applications. Therefore, their accuracy and sensitivity are important for ensuring the quality and reliability of the detectors. The system calibration was confirmed before each measurement session (see Appendix A3).

Silicon strip detectors in Publication VI and GaAs radiation detectors in Publication VII were successfully manufactured during two separate research projects. Electrical characterisation was performed on the test structures of both detector types.

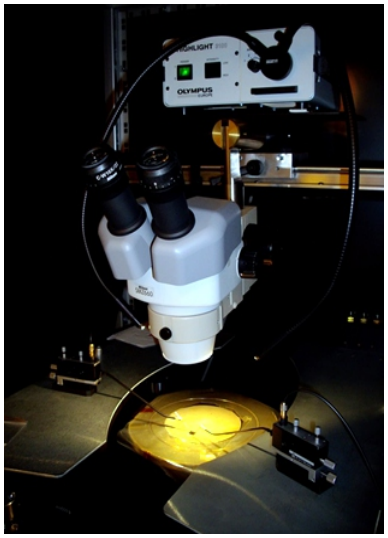

Figure 3.30: Semi-automatic probe-station for electrical characterisation.

The tracking detectors for future high-luminosity particle physics experiments have to be simultaneously radiation hard and cost efficient. Silicon strip detectors, shown in Figure 3.31, made of high-resistivity Magnetic Czochralski silicon (MCz-Si) substrates were successfully manufactured. For their electrical characterisation, CV and IV measurement were performed on 20 mini-sensors from three wafers.

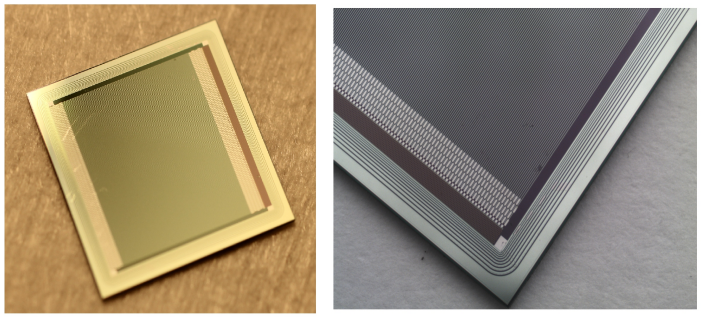

Figure 3.31: MCz-Si mini strip sensor with 1 x 1 cm^2 active area (left); zoomed view of the detector's strips (right).

The depletion voltages (V_{fd}) were extracted using intersection of two fitted lines of the $1/C^2$ vs. voltage curves, illustrated in Figure 3.32 (left). The depletion voltage remains uniformly between 120-150 V for the different wafers. The leakage current (I_{leak}) of the mini-sensors measured from the three wafers, shown in Figure 3.32 (right), stayed in the range of 0 - 55 nA/cm^2 for most of the tested sensors (approximately 63 %).

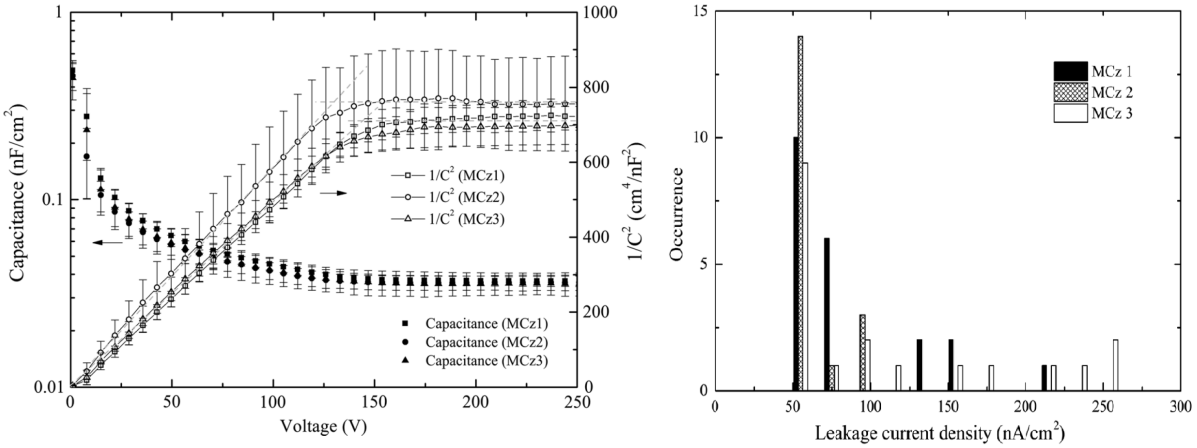

Figure 3.32: CV curves of 1 cm^2 mini-strip MCz-Si detectors (left) and the extracted leakage current densities (right).

Radiation detectors made on epitaxial GaAs substrates, shown in Figure 3.33, are a promising alternative to the silicon devices used for spectroscopy and radiography applications. However, why they are not commonly used is due to their more complex manufacturing and the availability of the material. Therefore only a few detectors were successfully manufactured.

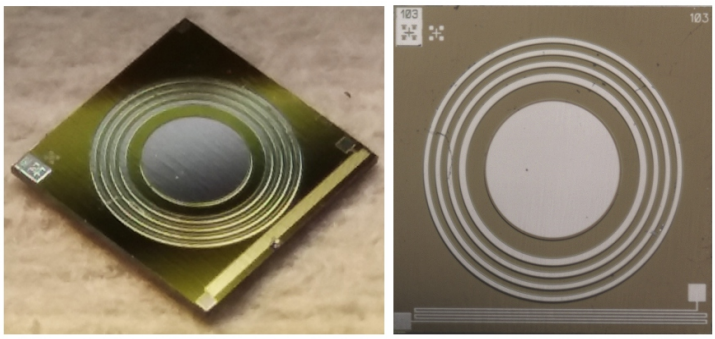

Figure 3.33: The GaAs radiation pad detector with a diameter of 1.75 mm for the inner most circle (left); zoomed view of the pad (right).

The full depletion voltage of these GaAs radiation detectors was in the range of 8–15 V and the leakage current in the range of 100–200 pA, corresponding to the current density of 10 nA/cm^2. The measurements were performed on two pad detectors

and the results are presented in Figure 3.34. The leakage current tended to saturate after the V_{fd} was reached, and a breakdown occurred in the better sample after about 200 V, i.e. at more than 10 times higher voltage than the depletion voltage (for such an example of breakdown see D167 J1 diode in Figure 3.34).

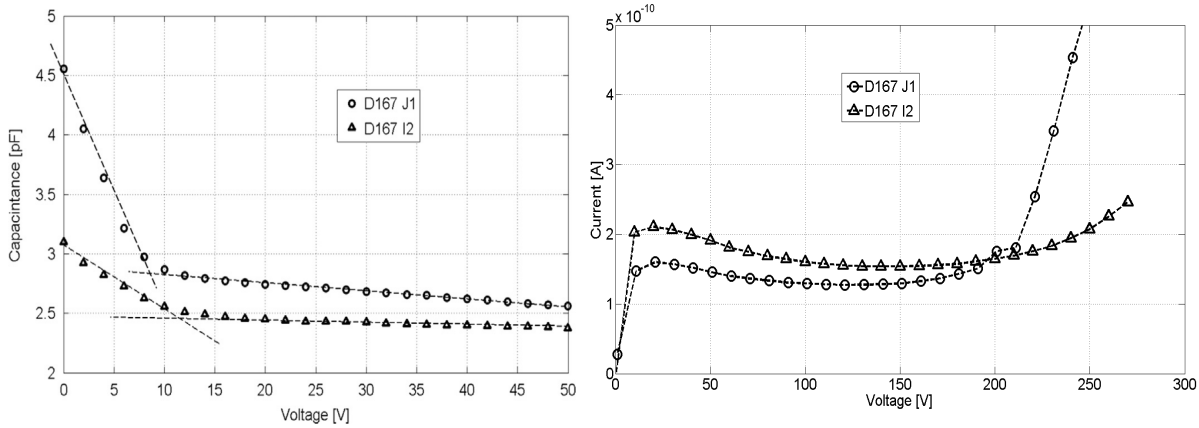

Figure 3.34: Capacitance-Voltage curves (left) and Current-Voltage curves (right) of GaAs radiation pad detectors D167 J1 and D167 I2. D167 I2 experienced a breakdown just above 200 V.

In general, the obtained leakage current and depletion voltage results were consistent and within the expected range. Both detector types were proven to be functional and suitable for the needs of particle and nuclear physics experiments.

CHAPTER 4

DISCUSSION AND RESEARCH CONCLUSION

The purpose of this thesis was to improve, develop, establish and apply novel quality assurance methods to the detector manufacturing process for the international nuclear and high-energy physics communities. The detectors should be maintenance-free since devices can only be replaced during long technical shut-downs. Furthermore, the detector modules must endure handling during installation and withstand heat generation and cooling during operations. Longevity in a severe radiation environment should also be assured. Visual inspection and electrical characterisations of particle detectors are presented in this work.

The detector studies included in this thesis, while based on different technologies, were united by the demand for reliable and endurant particle detectors. The combined results of this thesis demonstrate the importance of adequate quality assurance for guaranteed accurate data collection and long operating life of the detector.

GEM foil studies

Four major achievements were accomplished during the GEM foil studies contained in this thesis: a software analysis capable of precise foil inspection was developed in Publication I, a rigorous calibration procedure for the Optical Scanning System was established in Publications II and III, a detailed 3D GEM foil hole geometry study was performed for first-time and an impact of the hole geometry on the detector gain was confirmed in Publication IV.

The optical analysis of the GEM foil images has been complicated because the reflectance of the foil surface varies between individual foils, see Figure 3.4. Several issues can affect the image: homogeneity of illumination, foil tilt, waviness and position in the light field (focus), surface reflectivity and roughness, rim roughness and conical wall tilt.

In order to extract the foil characteristics from the highly variable input images, the software was designed to be as generic as reasonably achievable in terms of image pre-processing, segmentation and data analysis. This research was presented in Publication I.

However, improving the image analysis software was not enough to improve the

OSS inspection accuracy and precision. A rigorous calibration procedure was developed by determining the precision and accuracy with which the OSS can be calibrated. For this purpose, a calibration sample was microfabricated to confirm the tool calibration with a surface comparable to that of the GEM foil. To guarantee accurate and traceable results, the data was collected with a calibrated SEM device and later compared to the corresponding OSS images, see Publication II.

The most important result is that accurate imaging was achieved across a large TS area and by implication can be achieved over a large GEM area, if one can guarantee that the GEM foil sandwich structure remains as flat and as homogeneous in reflection as the silicon TS. The diameter measurements (OSS) exhibited an uncertainty of $\pm\ 1.03\,\mu\mathrm{m}$.

A serious limitation with this general approach comes from the fact that both employed methods (OSS and SEM) are essentially 2D methods used to examine 3D objects with two diameters (*d* and *D*), whose recorded values depend on maintaining precise focus distance control along the z-axis. Controlling focal distance across large area scans (tight auto focusing) is non-trivial.

To demonstrate this requirement, a second thorough OSS calibration was performed using a piece of GEM foil as TS in Publication III. The new TS that precisely reproduced the foils' holey surface, surface roughness, and reflectivity was designed. The TS was examined with the OSS and the results compared with those obtained with a 3D high-resolution non-contact imaging system - SWLI. This improved the previous calibration of the OSS set-up. The high-resolution SWLI [71] allowed detailed examination of the geometry of GEM foil holes, not only the foil surface. The new OSS diameter measurements expanded uncertainty with 95 % confidence level was $\pm\ 0.67\,\mu\mathrm{m}$ (a reduction of 65 %). This last calibration technique is currently employed for the calibration of the second OSS, constructed in the clean room of the Detector laboratory at the Helsinki Institute of Physics and the University of Helsinki.

Four new parameters were introduced and studied in detail to describe hole geometry, presented in Publication IV. In addition to the standard GEM hole parameters (*d* and *D*) - the shift (*S*) between the centres of the inner and outer diameters, illustrated in Figure 3.14, the total foil thickness (*T*) and metal (T_m) and polyimide (T_p) thickness, shown in Figure 3.15 and Figure 3.16, respectively. Variations in those parameters for neighbouring holes in different foil regions were observed.

Knowing the real hole geometry of existing foils has the potential to improve the GEM fabrication, which leads to better detector performance [41] and [64–68]. The results from the examined GEM foil sample indicate a probable mask misalignment during the foil fabrication, see Figure 3.19. Systematic deviation in *S* of $1.2\,\mu\mathrm{m}$ was observed. However, the GEM sample holes #5 and #22 feature a relative top and bottom side shift of $3\,\mu\mathrm{m}$.

To define the effect of GEM hole geometry variation in Publication IV, the ANSYS [80] and Garfield ++ [81] software packages were employed to simulate the GEM detector gain performance on the basis of the SWLI measured data. Two separate simulations studied the variations in the geometry of hourglass-shaped holes and the variations in the geometry of real holes.

The results prove that the hole geometry affects the gain performance of the GEM detectors. The simulated results indicate that the real GEM foil holes performance could differ from the design performance by as much as a 6 % increase in the electron production near the exit electrode of the GEM foil with a 4 % lower effective gain. Thus, the four new parameters, introduced to characterise GEM foil holes in these studies, should be included in the quality assurance process during GEM foil manufacturing. The recorded effect, though small, may be important since the simulated cases a feature GEM foils with ideal, uniformly shaped holes along the GEM foil. As demonstrated in measurements included in this thesis, a real GEM foil will always contain holes of different shapes and sizes.

Inspection of solid-state detectors

Promising results were achieved during the solid-state detector study. A new technique for assuring the height uniformity of chip interconnections in the pixel detector modules was proposed and implemented. Visual inspections were used to confirm the height of the soldering bumps, which form the connections between the sensing element and the readout chips, see Publication V.

In addition, two semiconductor detectors (Si and GaAs) were designed, microfabricated and tested. Electrical characterisation was used to evaluate the basic electrical parameters of the two semiconductor detectors in Publications VI and VII. The consistent results demonstrated detectors' reliability and preparedness to serve the needs of future particle and nuclear physics experiments.

Research conclusion

During all studies, strict calibration techniques and measurement uncertainties [60–63] were applied to guarantee the trustworthiness and accuracy of the measurement tools. Thus, all quality assurance techniques presented in this thesis were held in clean environments at monitored temperature and humidity.

The accuracy and the sensitivity of both QA techniques are important to ensure the quality and integrity of the particle detectors. Therefore, a calibration measurement check was performed on the inspection systems before each measurement session.

In conclusion, the main focus of this thesis work were the development and assessment of improved and strict methods for quality assurance of particle detectors,

which could guarantee not only the long operational life of detectors but also accurate and precise radiation detection. All of these goals were successfully achieved by using correctly calibrated and maintained instruments for quality assurance of particle detectors.

APPENDIX A

TRACEABILITY AND CALIBRATION PROCEDURES FOR QA INSTRUMENTS

A.1 SEM calibration

A Hitachi S-4800 FESEM with 3 nm lateral resolution [86], served as the 'gold standard' to determine the OSS calibration factor in Publication II.

The SEM was calibrated at 15 kV and $10\,\mu A$ according to Hitachi's specifications. The instrument's expanded uncertainty was determined using a SIRA SEM calibration specimen S170 [87], see Figure A.1. The calibration grid was measured three times, both vertically and horizontally without removing the sample between the measurements. The results were averaged and their experimental standard deviation was found, according to (B.1) and (B.3), from Appendix B.

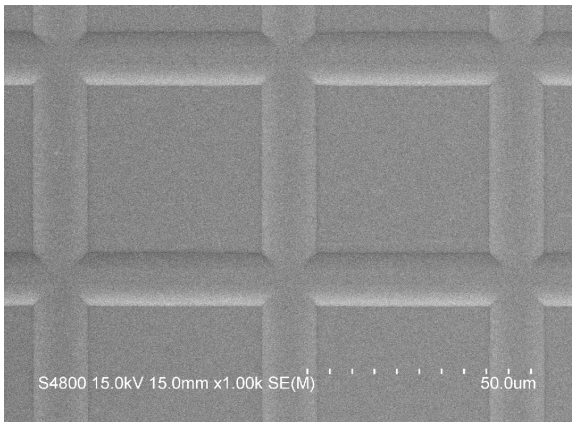

Figure A.1: SIRA SEM calibration specimen S170. The 19.7 lines mm^{-1} with period = $50.8\,\mu m$ had $\pm\ 0.02\,\mu m$ expanded uncertainty.

The combined standard uncertainty for the SEM imaging was calculated using (B.5) and was determined to be $0.01\,\mu m$ at 1000 X magnification. The same magnification was used during all TS measurements. The expanded uncertainty of the SEM was $\pm\ 0.02\,\mu m$, calculated using (B.6).

OSS/SEM traceable calibration

The flow of the OSS/SEM traceable calibration, used in Publication II, is illustrated in Figure A.2.

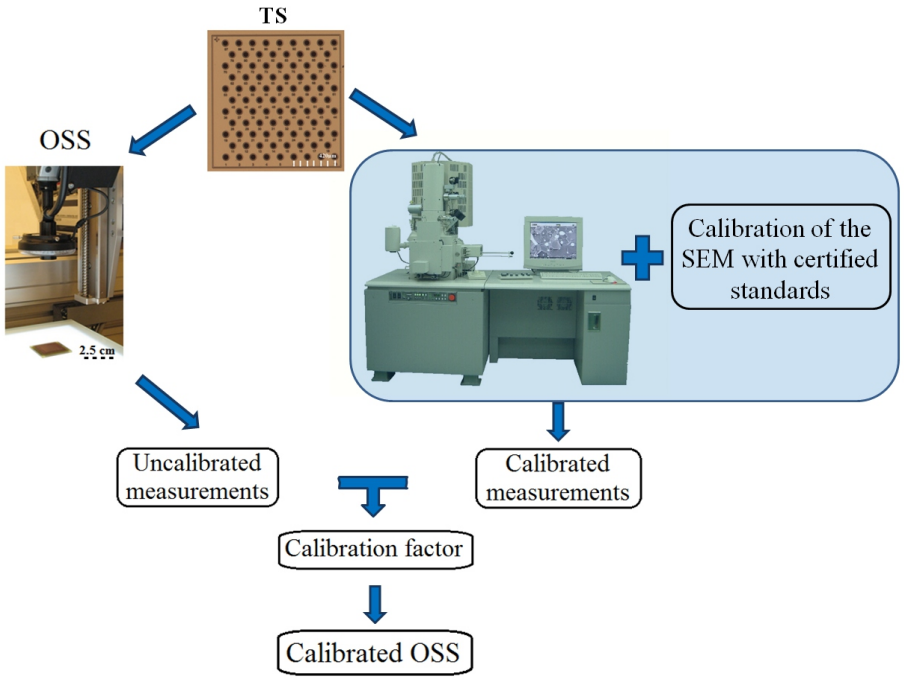

Figure A.2: Flow chart illustrating the logic of the OSS/SEM calibration.

To verify the absence of distortion (alteration of original cavity shape) and magnification errors (of a cavity imaged by OSS), the cavities were selected close to the sample diagonals, Figure A.3. The TS was placed at the centre of the nine different positions of the table, see Figure 3.8, and scanned several times without moving the TS between the repeated measurements. The TS fits into a single OSS image and it was placed at the centre of the field of view.

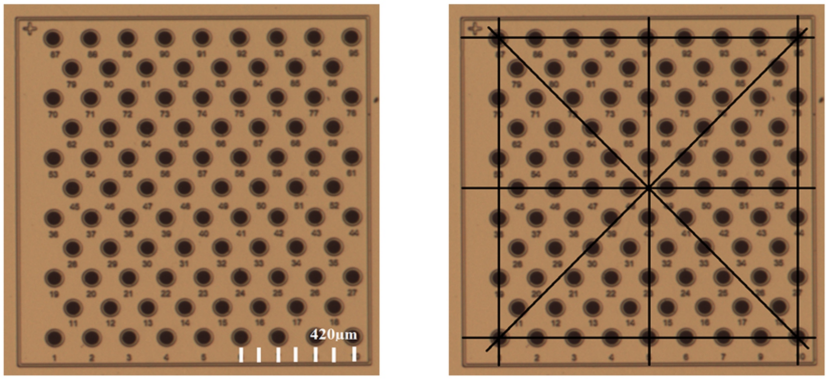

Figure A.3: The TS imaged by OSS (left) with the diagonal method for cavity selection (right).

A.2 SWLI calibration

The SWLI [71], used in Publications III and IV for the detailed study of GEM hole geometry, was calibrated at constant temperature and humidity (22.4 $\pm$ 1 C° and 55 $\pm$ 3 %, respectively, measured with a REED ST-171 Standard Data Logger). The instrument's expanded uncertainty was determined by using a 2D resolution mesh of a SHS-1800 QC [88] and a depth standard # 0313 [89], illustrated in Figure A.4.

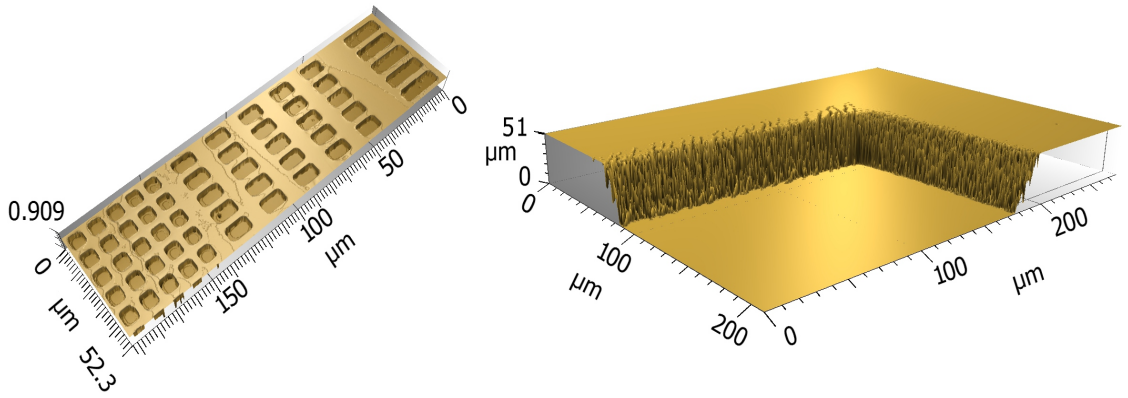

Figure A.4: 2D resolution mesh (left) and depth standard (right) reconstructed with the MountainsMap 3D software.

The 2D resolution mesh feature was used to define the lateral uncertainty of the SWLI. The calibration standard was scanned with the SWLI three times both vertically and horizontally with (case *a*) and without (case *b*) removing the sample between the measurements. Using the MountainsMap [79] software, 10 profiles (5 North-South and 5 West-East directions) were extracted from each image. The results were averaged and their experimental standard deviation was found, according to (B.1) and (B.3), from Appendix B. The lateral combined standard uncertainty of the SWLI was determined using (B.5) to be $\pm$ 0.0047 µm (for case *a*) and $\pm$ 0.0049 µm (for case *b*) at 25X magnification. The same magnification was used in all subsequent TS measurements. The expanded uncertainty of the SWLI, calculated using (B.6), was $\pm$ 0.0091 µm and $\pm$ 0.0097 µm (for cases *a* and *b*, respectively), calculated using (B.6).

The same procedure was used to define the vertical combined standard uncertainty of the SWLI, by using the depth standard feature. The results were $\pm$ 0.001 µm and $\pm$ 0.003 µm (for cases *a* and *b*, respectively), and an expanded uncertainty of $\pm$ 0.002 µm and $\pm$ 0.006 µm (for cases *a* and *b*, respectively).

OSS/SWLI traceable calibration

Figure A.5 illustrates a schema of the OSS/SWLI traceable calibration used in Publications III and IV.

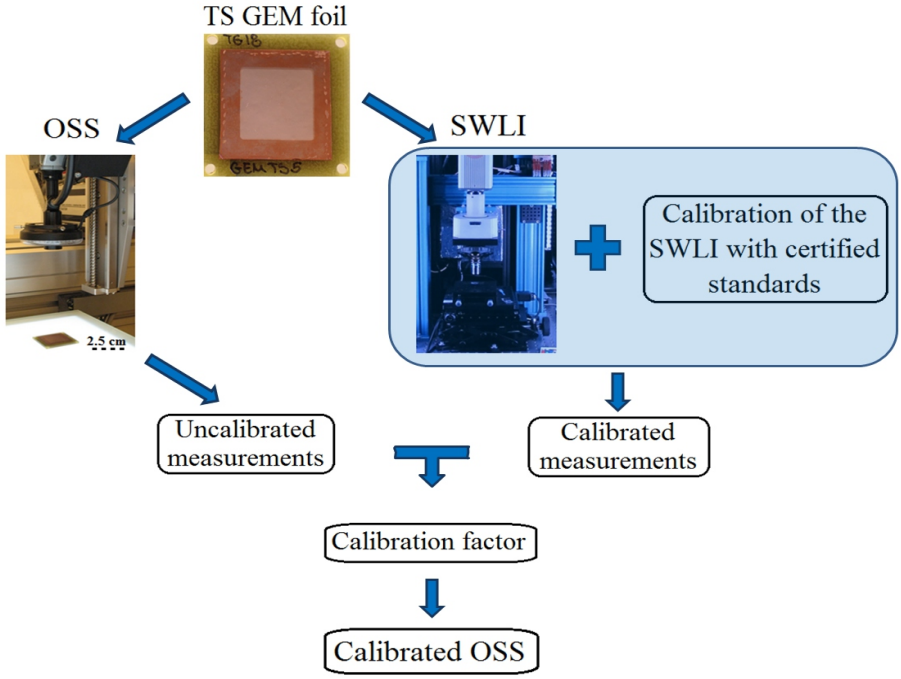

Figure A.5: Flow chart illustrating the logic of the OSS/SWLI calibration.

A similar GEM foil hole selection process was used in Publications III and IV. The holes were selected in the flattest possible area of the sample. Figure A.6 illustrates the selection used during the GEM hole geometry study. Distortion and magnification error checks were also performed.

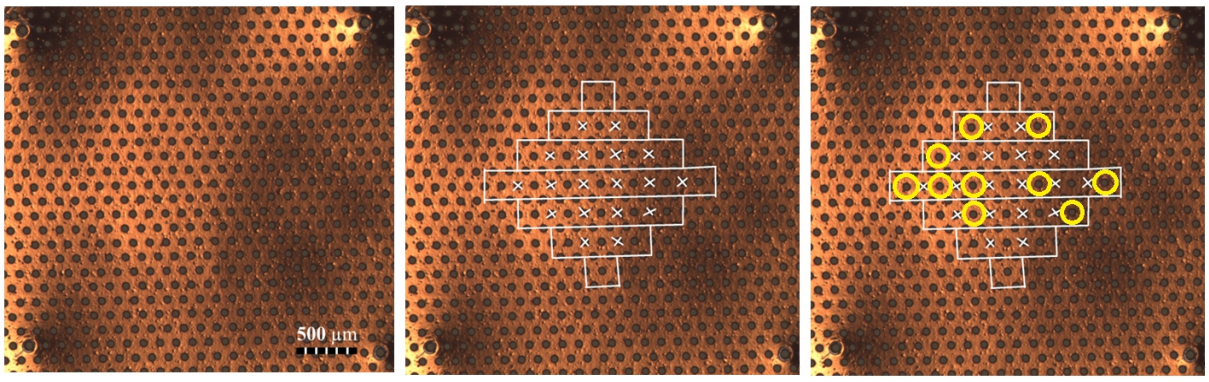

Figure A.6: The map of the 25 SWLI holes that were chosen for the SWLI GEM hole geometry study (middle); the yellow circles show the 10 holes chosen for the simulation studies (right).

SWLI GEM hole geometry

A schema, illustrated in Figure A.7, describes the methodology followed during the detailed study of the GEM hole geometry in Publication IV.

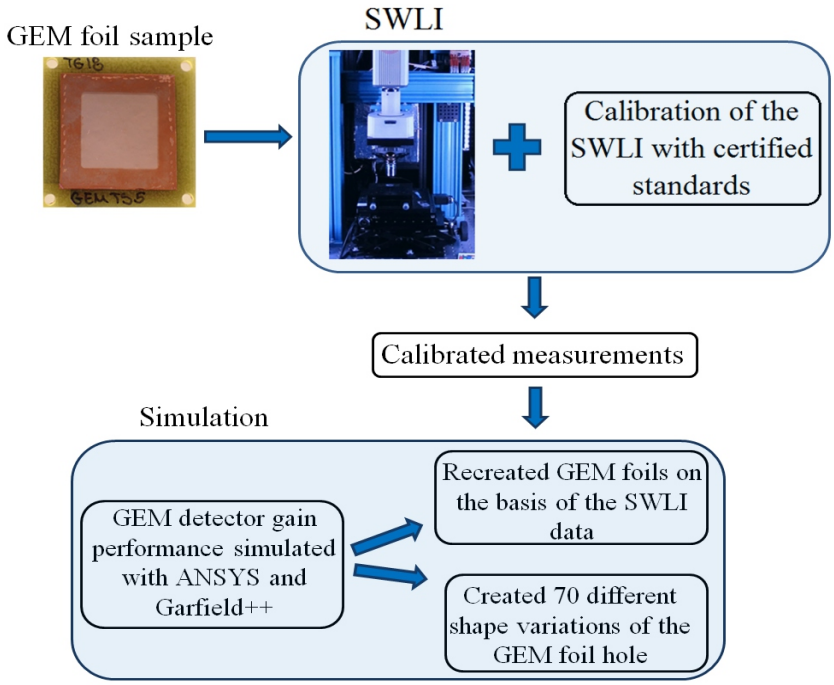

Figure A.7: Flow chart illustrating the logic of the GEM hole geometry and simulation studies.

A.3 Probe-station calibration

A n-type Si diode with a known behaviour, shown in Figure A.8, was used for the calibration check of the semi-automated probe-station before each measurement session. The diode depletion voltage and leakage current measurements, illustrated in Figure A.9, were performed in a clean room environment at monitored temperature and humidity. The same conditions were maintained during the CV/IV measurements of all solid-state detectors examined in this thesis and Publications VI and VII.

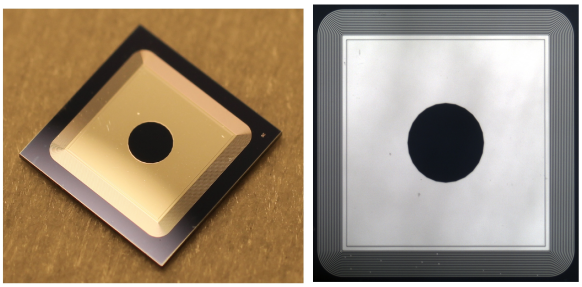

Figure A.8: The Si diode with 0.5 x 0.5 cm^2 active area (left) and its zoomed view (right).

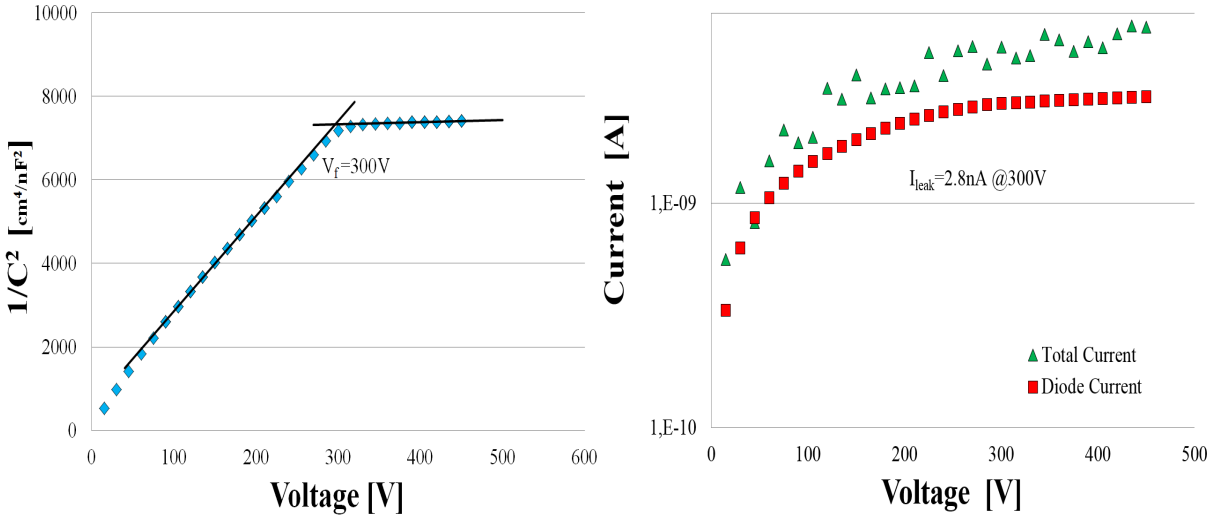

Figure A.9: The Si diode depletion voltage (left) and leakage current (right) measurements.

MEASUREMENT UNCERTAINTIES

All reported results in Publications II-V are established in accordance to the Type A standard uncertainty calculations from the Evaluation of measurement data — Guide to the expression of uncertainty in measurement (JCGM 100:2008) [63].

All optical instruments were calibrated using calibration samples designed and certified for their particular use. Each sample was examined three times and the result was reported as the average $\overline{q}$ of n individual observations q_k:

$$\overline{q} = \frac{1}{n}\sum_{k=1}^{n} q_k. \tag{B.1}$$

The experimental variance of the observations, which estimates the variance σ^2 of the probability distribution of $\mathbf{q}$ is:

$$s^2(q_k) = \frac{1}{n-1}\sum_{j=1}^{n}(q_j - \overline{q})^2. \tag{B.2}$$

The estimate of $\sigma^2(\overline{q}) = \frac{\sigma^2}{n}$, the variance of the mean is:

$$s^2(\overline{q}) = \frac{s^2}{n}. \tag{B.3}$$

The experimental variance of the mean $s^2(\overline{q})$ and the experimental standard deviation of the mean $s(\overline{q}) = +\sqrt{s^2(\overline{q})}$, quantify how well $\overline{q}$ estimates the expectation of $\mathbf{q}$, and either value may be used as a measure of the uncertainty of $u(\overline{q})$.

$$u^2(\overline{q}) = s^2(\overline{q}). \tag{B.4}$$

The combined standard uncertainty of each measurement system was calculated by summing in quadrature the standard certified uncertainty and the measurement uncertainty of the dimensional measurement using the Vision Systems (National Physics Laboratory) [60].

$$U_c = \sqrt{U_{Calibration\ standard}{}^2 + U_{Sample\ measurements}{}^2}. \tag{B.5}$$

The expanded uncertainty was used to provide a coverage probability of 95% (Coverage factor **k = 2**).

$$U_{exp} = U_c \times 1.96. \tag{B.6}$$

List of Figures

1.1 Schematic presentation of the Standard Model quantum field theory . 5
1.2 The CERN facility 6
1.3 Cross-section of the CMS experiment 7
1.4 The contributions of the Helsinki Institute of Physics to the CERNs experiments 8
1.5 Cross-section of the ALICE experiment 9
1.6 The FAIR facility 10
1.7 The beam monitoring system at FAIR 11

2.1 Energy loss according to the Betche-Bloch equation 14
2.2 SEM image of a GEM foil 17
2.3 GEM foil manufacturing techniques 17
2.4 Electric field map inside GEM foil holes 18
2.5 GEM detector construction 20
2.6 Operation principle of a silicon strip and pixel detectors 26
2.7 Wire bonding 26
2.8 Hybrid pixel module 27
2.9 Solder bumps imaged with SEM 28
2.10 Bump manufacturing technique 28

3.1 GEM foil defects 29
3.2 Solder bumps defects 30
3.3 The Optical Scanning System 32
3.4 Different GEM foils 33
3.5 Darker and lighter GEM foil areas 33
3.6 Transfer standard imaged with SEM and OSS 34
3.7 TS manufacturing 35
3.8 The nine positions used for OSS calibration 36
3.9 Calibtarion results for TS inner cavities 37
3.10 Calibtarion results for TS outer cavities 37
3.11 GEM foil transfer standard 38
3.12 Calibtarion results for the inner GEM foil holes diameter 39
3.13 Calibtarion results for the outer GEM foil holes diameter 39

3.14 GEM foil holes inner (d) and outer (D) diameter, and the shift S measured between their centres . . . 41
3.15 GEM foil total thickness (T) . . . 41
3.16 GEM foil metal ($\boldsymbol{T_m}$) and polyimide ($\boldsymbol{T_p}$) thickness . . . 41
3.17 GEM foil inner hole d values measured with SWLI . . . 42
3.18 GEM foil outer hole D values measured with SWLI . . . 43
3.19 GEM foil shift S between d and D measured with SWLI . . . 43
3.20 GEM foil thickness T measured with SWLI . . . 44
3.21 The various GEM foil hole geometries simulated with ANSYS . . . 45
3.22 The simulated effective gain of the GEM foil . . . 46
3.23 The electrons produced near the exit electrode of the GEM foil . . . 46
3.24 Examples of real GEM foil hole geometries . . . 47
3.25 Simulated results based on SWLI measured GEM foil hole geometries . 48
3.26 NIST calibrated $\boldsymbol{SiO_2}$ spheres for SWLI calibration . . . 49
3.27 The maximum height H extraction of the solder bumps . . . 50
3.28 3D reconstruction of the soldering bumps profile . . . 50
3.29 Maximum height H comparison of neighbouring solder bumps . . . 51
3.30 Semi-automatic probe-station . . . 52
3.31 MCz-Si mini strip sensor . . . 52
3.32 Electrical characterisation of MCz-Si strip detectors . . . 53
3.33 GaAs radiation pad detector . . . 53
3.34 Electrical characterisation of GaAs radiation pad detectors . . . 54

A.1 SEM calibration standard . . . 59
A.2 The OSS/SEM calibration flow chart . . . 60
A.3 TS cavity selection . . . 60
A.4 SWLI calibration standards . . . 61
A.5 The OSS/SLWI calibration flow chart . . . 62
A.6 GEM foil hole selection . . . 62
A.7 The SWLI GEM hole geometry and simulation studies . . . 63
A.8 Si diode for probe-station calibration . . . 64
A.9 CV and IV characteristics of the Si calibration diode . . . 64

List of Tables

2.1 Properties of materials commonly used in particle detectors 15

3.1 Comparison of TS cavity parameters measured with OSS and SEM . . 36
3.2 SWLI measured top and bottom parameters of GEM foil hole 42
3.3 SWLI maximum height H measurement of solder bump 51

BIBLIOGRAPHY

[1] A. Pich, "The Standard Model of Electroweak Interactions", in: *Lecture given at the 4th CERN - CLAF School of High Energy Physics,Vina del Mar, Chile* 419 (Mar. 2007), arXiv: 0705.4264 [hep-ph] (cit. on p. 5).

[2] *University of Zurich*, http://www.physik.uzh.ch/groups/serra/StandardModel.html, Accessed: August, 2016 (cit. on p. 5).

[3] The ATLAS Collaboration, "Observation of a new particle in the search for the Standard Model Higgs boson with the ATLAS detector at the LHC", in: *Physics Letters B* 716 (Aug. 2012), DOI: 10.1016/j.physletb.2012.08.020 (cit. on p. 5).

[4] The CMS Collaboration, "Observation of a new boson at a mass of 125 GeV with the CMS experiment at the LHC", in: *Physics Letters B* 716 (Aug. 2012), DOI: http://dx.doi.org/10.1016/j.physletb.2012.08.021 (cit. on p. 5).

[5] *CERN, The European Organization for Nuclear Research*, http://home.cern.ch/, Accessed: August, 2016 (cit. on pp. 6, 49).

[6] *LHC Design Report: The LHC infrastructure and general services*, Geneva, Switzerland: CERN, The European Organization for Nuclear Research, 2004 (cit. on p. 6).

[7] *ALICE physics performance : Technical Design Report*, CERN-LHCC-2005-030, ALICE-TDR-13, Geneva, Switzerland: CERN, The European Organization for Nuclear Research, 2005 (cit. on p. 6).

[8] *ATLAS: Detector and physics performance technical design report*, CERN-LHCC-99-14, ATLAS-TDR-14, Geneva, Switzerland: CERN, The European Organization for Nuclear Research, 1999 (cit. on p. 6).

[9] *CMS Physics : Technical Design Report*, CERN-LHCC-2007-009, CMS-TDR-8.2, Geneva, Switzerland: CERN, The European Organization for Nuclear Research, 2007 (cit. on p. 6).

[10] *Framework TDR for the LHCb Upgrade : Technical Design Report*, CERN-LHCC-2012-007, LHCb-TDR-12, Geneva, Switzerland: CERN, The European Organization for Nuclear Research, 2012 (cit. on p. 7).

[11] *TOTEM: Technical design report. Total cross section, elastic scattering and diffraction dissociation at the Large Hadron Collider at CERN*, CERN-LHCC-2004-002, TOTEM-TDR-001, Geneva, Switzerland: CERN, The European Organization for Nuclear Research, 2002 (cit. on p. 7).

[12] *The Compact Muon Solenoid (CMS)*, http://home.cern/about/experiments/cms, Accessed: August, 2016 (cit. on pp. 7, 27, 49).

[13] *LHC Luminosity and energy upgrade : A Feasibility Study*, LHC-Project-Report-626, Geneva, Switzerland: CERN, The European Organization for Nuclear Research, 2002 (cit. on p. 8).

[14] *Timing Measurements in the Vertical Roman Pots of the TOTEM Experiment, Technical Design Report*, CERN-LHCC-2014-020, TOTEM-TDR-002, Geneva, Switzerland: CERN, The European Organization for Nuclear Research, 2014 (cit. on p. 8).

[15] G. Ricciardi, "Total Cross Section, Elastic Scattering and Diffraction Dissociation", in: *talk given at the LHC CSN1, Bari, Italy* (July 2005) (cit. on p. 8).

[16] V. Hlinka et al., "Time Projection Chambers for tracking and identification of radioactive beams", in: *Nuclear Instruments and Methods in Physics Research A* 419 (Dec. 1998), DOI: 10.1016/S0168-9002(98)00827-4 (cit. on p. 8).

[17] *The ALICE Collaboration Upgrade of the ALICE Time Projection Chamber*, CERN-LHCC-2013-020, ALICE-TDR-016, Geneva, Switzerland: CERN, The European Organization for Nuclear Research, 2013 (cit. on p. 8).

[18] G. Charpak et al., "The use of multiwire proportional counters to select and localize charged particles", in: *Nuclear Instruments and Methods in Physics Research A* 62 (July 1968), DOI: 10.1016/0029-554X(68)90371-6 (cit. on pp. 9, 16).

[19] F. Sauli, "GEM: A new concept for electron amplification in gas detectors", in: *Nuclear Instruments and Methods in Physics Research A* 386 (Nov. 1997), DOI: 10.1016/S0168-9002(96)01172-2 (cit. on pp. 9, 16, 18, 21, 29, 35).

[20] *A Large Ion Collider Experiment (ALICE)*, http://home.cern/about/experiments/alice, Accessed: August, 2016 (cit. on p. 9).

[21] *CMS Technical Design Report for the Pixel Detector Upgrade*, CERN-LHCC-2012-016, CMS-TDR-11, Geneva, Switzerland: CERN, The European Organization for Nuclear Research, 2012 (cit. on p. 9).

[22] W. F. Henning, "The future GSI facility", in: *Nuclear Instruments and Methods in Physics Research B* 214 (Jan. 2004), DOI: 10.1016/S0168-583X(03)01761-0 (cit. on p. 9).

[23] Th. Stöhlker et al., "APPA at FAIR: From fundamental to applied research", in: *Nuclear Instruments and Methods in Physics Research B* 356 (May 2015), DOI: 10.1016/j.nimb.2015.07.077 (cit. on p. 10).

[24] J. M. Heuser, "The Compressed Baryonic Matter Experiment at FAIR", in: *Nuclear Physics A* 904–905 (May 2012), DOI: 10.1016/j.nuclphysa.2013.02.170 (cit. on p. 10).

[25] C. Schwarz, "The PANDA Experiment at FAIR", in: *Journal of Physics: Conference Series* 734 (2012), DOI: 10.1088/1742-6596/374/1/012003 (cit. on p. 10).

[26] A. Herlert, "The NUSTAR program at FAIR", in: *EPJ Web of Conferences* 71 (2014), DOI: 10.1051/epjconf/20147100064 (cit. on p. 10).

[27] *FAIR, The Facility for Antiproton and Ion Research*, http://www.fair-center.eu/index.php?id=1, Accessed: August, 2016 (cit. on p. 10).

[28] M. Kalliokoski et al., "GEM-TPC Trackers for the Super-FRS at FAIR", in: *Proceedings of the International Particle Accelerator Conference, Kyoto, Japan* (May 2010) (cit. on p. 10).

[29] F. García et al., "Prototype Development of a GEM -TPC for the Super-FRS of the FAIR Facility", in: *IEEE transactions on Nuclear Science* Nuclear Science Symposium Conference Record (NSS/MIC) (Oct. 2011), DOI: 10.1109/NSSMIC.2011.6154683 (cit. on p. 11).

[30] *Technical Design Report on the Super-FRS*, Darmstadt, Germany: FAIR, The Facility for Antiproton and Ion Research, 2008 (cit. on p. 11).

[31] T. Grahn, "Beam Diagnostics at the Super-FRS", in: *talk given at the 13th Nordic Meeting on Nuclear Physics, Saariselkä, Finnish Lapland* (Apr. 2015) (cit. on p. 11).

[32] G. Knoll, *Radiation Detection and Measurement*, Fourth edition, New Jersey, USA: John Wiley and Sons, 2010 (cit. on p. 13).

[33] G. Lutz, *Semiconductor Radiation Detectors*, Germany: Springer, 1999 (cit. on pp. 13, 27).

[34] K.A. Olive et al. (Particle Data Group), "Review of Particle Physics", in: *Chinese Physics C* 38(9) (2014), DOI: 10.1088/1674-1137/38/9/090001 (cit. on pp. 14, 15).

[35] Adrian C. Melissinos and Jim Napolitano, *Experiments in Modern Physics*, Second edition, 525 B Street, Suite 1900, San Diego, CA, USA: Academic Press, an imprint of Elsevier Science, 2003 (cit. on pp. 15, 24).

[36] M. Chernyshova et al., "Development of GEM gas detectors for X-ray crystal spectrometry", in: *Journal of Instrumentation* 9 (Mar. 2014), DOI: 10.1088/1748-0221/9/03/C03003 (cit. on p. 16).

[37] J. Rzadkiewicz et al., "Design of T-GEM detectors for X-ray diagnostics on JET", in: *Nuclear Instruments and Methods in Physics Research A* 720 (Aug. 2013), DOI: 10.1016/j.nima.2012.12.041 (cit. on p. 16).

[38] M. Alfonsi, "The GEM detectors for the innermost region of the forward muon station of the LHCb experiment", in: *PhD Thesis, University of Rome Tor Vergata, Italy* (2008) (cit. on pp. 16, 22).

[39] *Technology Transfer, Technical questions on GEM manufacturing and pricing*, http://knowledgetransfer.web.cern.ch/technology-transfer/external-partners/gas-electron-multiplier/, Accessed: August, 2016 (cit. on p. 17).

[40] R. Oliveira, "MPGDs and GEM foils and detector fabrication techniques", in: *talk given at the IWAD and the 14th RD51 Collaboration Meeting, Kolkata, India* (Oct. 2014) (cit. on p. 17).

[41] S. Bachmann et al., "Charge amplification and transfer processes in the gas electron multiplier", in: *Nuclear Instruments and Methods in Physics Research A* 438 (Dec. 1999), DOI: 10.1016/S0168-9002(99)00820-7 (cit. on pp. 18, 19, 29, 40, 44, 56).

[42] D. Pinci, "A triple-GEM detector for the muon system of the LHCb experiment", in: *PhD Thesis, University of Cagliari, Italy* (2002) (cit. on p. 19).

[43] F. García, "GEM-TPC Development for the Super-FRS", in: *talk given at the FAIR mini-workshop, Jyväskylä, Finland* (Dec. 2015) (cit. on p. 20).

[44] S. Ramo, "Currents Induced by Electron Motion", in: *Proceedings of the Institute of Radio Engineers* 27 (Sept. 1939), DOI: 10.1016/S0168-9002(99)00820-7 (cit. on p. 22).

[45] A. Bressan et al., "High rate behavior and discharge limits in micro-pattern detectors", in: *Nuclear Instruments and Methods in Physics Research A* 424 (Mar. 1999), DOI: 10.1016/S0168-9002(98)01317-5 (cit. on pp. 22, 23).

[46] S. Bachmann et al., "Discharge mechanisms and their prevention in the gas electron multiplier (GEM)", in: *Nuclear Instruments and Methods in Physics Research A* 479 (Mar. 2002), DOI: 10.1016/S0168-9002(01)00931-7 (cit. on p. 22).

[47] D. S. McGregor and H. Hermon, "Room-temperature compound semiconductor radiation detectors", in: *Nuclear Instruments and Methods in Physics Research A* 395 (Aug. 1997), DOI: 10.1016/S0168-9002(97)00620-7 (cit. on p. 23).

[48] G. Dearnaley and A.B. Whitehead, "The semiconductor surface barrier for nuclear particle detection", in: *Nuclear Instruments and Methods* 12 (July 1961), DOI: 10.1016/0029-554X(61)90138-0 (cit. on p. 23).

[49] Frank Hartmann, *Evolution of Silicon Sensor Technology in Particle Physics*, Germany: Springer, 2008 (cit. on p. 23).

[50] S. M. Sze, *Physics of Semiconductor Devices*, 2nd Edition, New Jersey, USA: John Wiley and Sons, 1981 (cit. on p. 24).

[51] S. Väyrynen, "Irradiation of silicon particle detectors with MeV-protons", in: *PhD Thesis, University of Helsinki, Finland* (2010) (cit. on p. 25).

[52] M. Krammer, "Detector Structures", in: *talk given at the XI ICFA School on Instrumentation in Elementary Particle Physics, San Carlos de Bariloche, Argentina* (Jan. 2010) (cit. on p. 26).

[53] R. Wallny, "How do Silicon Sensors Work", in: *talk given at the Second CDF Silicon Workshop, Santa Barbara, USA* (May 2006) (cit. on p. 26).

[54] E. Tuominen, "Development of Radiation Hard Radiation Detectors - Differences between Czochralski Silicon and Float Zone Silicon", in: *PhD Thesis, Helsinki Institute of Physics, Finland* (2003) (cit. on p. 27).

[55] P. Luukka, "Characterization of Czochralski Silicon Detectors", in: *PhD Thesis, Helsinki Institute of Physics, Finland* (2003) (cit. on p. 27).

[56] E. Tuovinen, "Processing of Radiation Hard Particle Detectors on Czochralski Silicon", in: *PhD Thesis, Helsinki Institute of Physics, Finland* (2008) (cit. on p. 27).

[57] John H. Lau, *Flip Chip Technologies*, New York, USA: McGraw - Hill, 1996 (cit. on pp. 27, 48).

[58] J. Salmi and J. Salonen, "Solder Bump Flip Chip Bonding for Pixel Detector Hybridization", in: *Workshop on Bonding and Die Attach Technologies, CERN, Geneva, Switzerland* (June 2003) (cit. on p. 28).

[59] M. Kalliokoski et al., "Optical scanning system for quality control of GEM-foils", in: *Nuclear Instruments and Methods in Physics Research A* 664 (Feb. 2012), DOI: 10.1016/j.nima.2011.10.058 (cit. on p. 29).

[60] Tim Coveney, *Dimensional Measurement using Vision Systems*, Measurement Good Practice Guide 39, Teddington, Middlesex, UK: Queen's Printer and Controller of HMSO, 2014 (cit. on pp. 31, 35, 40, 57, 65).

[61] *General requirements for the competence of testing and calibration laboratories*, ISO/IEC 17025, Geneva, Switzerland: International Organization for Standardization, 2005 (cit. on pp. 31, 35, 40, 57).

[62] *The Expression of Uncertainty and Confidence in Measurement*, UKAS, M3003, Feltham, Middlesex, UK: United Kingdom Accreditation Service, 2012 (cit. on pp. 31, 35, 40, 51, 57).

[63] *Evaluation of measurement data — Guide to the expression of uncertainty in measurement (GUM)*, JCGM 100:2008, Sèvres-Cedex FRANCE: Joint Committee for Guides in Metrology, 2008 (cit. on pp. 31, 35, 40, 51, 57, 65).

[64] M. Posik and B. Surrow, "Optical and electrical performance of commercially manufactured large GEM foils", in: *Nuclear Instruments and Methods in Physics Research A* 802 (Dec. 2015), DOI: 10.1016/j.nima.2015.08.048 (cit. on pp. 31, 44, 56).

[65] U. Becker, B. Tamm, and S. Hertel, "Test and evaluation of new GEMs with an automatic scanner", in: *Nuclear Instruments and Methods in Physics Research A* 556 (Jan. 2006), DOI: 10.1016/j.nima.2005.11.056 (cit. on pp. 31, 44, 56).

[66] F. Simon et al., "Development of Tracking Detectors With Industrially Produced GEM Foils", in: *IEEE transactions on Nuclear Science* 54 (Dec. 2007), DOI: 10.1109/TNS.2007.909912 (cit. on pp. 31, 44, 56).

[67] M. Kalliokoski et al., "Study of GEM-foil defects with optical scanning system", in: *IEEE transactions on Nuclear Science* Nuclear Science Symposium Conference Record (NSS/MIC) (Nov. 2010), DOI: 10.1109/NSSMIC.2010.5874011 (cit. on pp. 31, 32, 44, 56).

[68] M. Posik and B. Surrow, "Research and development of commercially manufactured large GEM foils", in: *Nuclear Instruments and Methods in Physics Research A* (2015), DOI: 10.1016/j.nima.2015.08.048 (cit. on pp. 31, 44, 56).

[69] *National Instruments Corporation (U.K.) Ltd.* http://uk.ni.com/, Accessed: August, 2016 (cit. on p. 32).

[70] A. Karadzhinova et al., "Microfabrication of Transfer Standards for Calibration of Optical Quality Assurance System", in: *Proceedings of 24th Micromechanics and Microsystems Europe Conference, Espoo, Finland* (Sept. 2013) (cit. on p. 34).

[71] J. Seppä et al., "Quasidynamic calibration of stroboscopic scanning white light interferometer with a transfer standard", in: *Optical Engineering* 52 (Dec. 2013), DOI: 10.1117/1.OE.52.12.124104 (cit. on pp. 38, 40, 56, 61).

[72] *Finnish Center for Metrology and Accreditation, MIKES*, http://www.mikes.fi/front-page, Accessed: August, 2016 (cit. on p. 38).

[73] G. Bencivenni et al., "A comparison between GEM-based detector simulation and experimental measurements", in: *Nuclear Instruments and Methods in Physics Research A* 492 (Nov. 2002), DOI: 10.1016/S0168-9002(02)01472-9 (cit. on p. 40).

[74] O. Bouianov et al., "Foil geometry effects on GEM characteristics", in: *Nuclear Instruments and Methods in Physics Research A* 458 (Feb. 2001), DOI: 10.1016/S0168-9002(00)00897-4 (cit. on p. 40).

[75] F. Sauli, "The gas electron multiplier (GEM): Operating principles and applications", in: *Nuclear Instruments and Methods in Physics Research A* 805 (Jan. 2016), DOI: 10.1016/j.nima.2015.07.060 (cit. on p. 40).

[76] Ö. Şahin et al., "Penning transfer in argon-based gas mixtures", in: *Journal of Instrumentation* 5 (May 2010), DOI: 10.1088/1748-0221/5/05/P05002 (cit. on p. 40).

[77] A. Bondar, A. Buzulutskov, and L. Shekhtman, "High pressure operation of the triple-GEM detector in pure Ne, Ar and Xe", in: *Nuclear Instruments and Methods in Physics Research A* 481 (Apr. 2002), DOI: 10.1016/S0168-9002(01)01369-9 (cit. on p. 40).

[78] F.D. Amaro et al., "Operation of a single-GEM in noble gases at high pressures", in: *Nuclear Instruments and Methods in Physics Research A* 579 (Aug. 2007), DOI: 10.1016/j.nima.2007.04.013 (cit. on p. 40).

[79] *Digital Surf Inc*, http://www.digitalsurf.fr/en/index.html, Accessed: August, 2016 (cit. on pp. 41, 61).

[80] *ANSYS Inc*, http://www.ansys.com//, Accessed: August, 2016 (cit. on pp. 44, 57).

[81] H. Schindler and R. Veenhof, *Garfield++: Simulation of tracking detectors*, http://garfieldpp.web.cern.ch/garfieldpp/, Accessed: August, 2016 (cit. on pp. 44, 57).

[82] *Advacam Oy*, http://www.advacam.com/en/, Accessed: August, 2016 (cit. on p. 49).

[83] S. Savolainen-Pulli et al., "Experiences in flip chip production of radiation detectors", in: *Nuclear Instruments and Methods in Physics Research A* 565 (Sept. 2006), DOI: 10.1016/j.nima.2006.04.090 (cit. on p. 49).

[84] *Corpuscular Inc.* http://www.microspheres-nanospheres.com/, Accessed: August, 2016 (cit. on p. 49).

[85] *National Institute of Standards and Technology*, http://www.nist.gov/, Accessed: August, 2016 (cit. on p. 49).

[86] Marianna Kemell, *Hitachi S-4800 FESEM – Short instructions for use*, Version 4, 2008 (cit. on p. 59).

[87] *Van Loenen Instruments*, http://www.loeneninstruments.com/, Accessed: August, 2016 (cit. on p. 59).

[88] *SiMETRICS GmbH*, http://www.simetrics.de/pdf/VS.pdf, Accessed: August, 2016 (cit. on p. 61).

[89] *VLSI Standards, Inc.* http://www.vlsistandards.com/products/absolute_model_listing.asp?SID=100, Accessed: August, 2016 (cit. on p. 61).